NORTHWESTERN UNIVERSITY

Schrödinger Cat State Atomic Interferometer with Heisenberg-Limited Sensitivity and Detection of Collective States

A DISSERTATION

SUBMITTED TO THE GRADUATE SCHOOL
IN PARTIAL FULFILLMENT OF THE REQUIREMENTS

for the degree

DOCTOR OF PHILOSOPHY

Field of Physics and Astronomy

By

Resham Sarkar

EVANSTON, ILLINOIS

December 2016

Abstract

Schrödinger Cat State Atomic Interferometer with Heisenberg-Limited Sensitivity and Detection of Collective States

Resham Sarkar

An atom interferometric gyroscope (AIG) made with an uncorrelated ensemble of N two-level atoms, rotating at a rate Ω_G about an axis normal to the area Θ accrues a phase $\phi = 2\omega_C \Theta \Omega_G / c^2$ due to the Sagnac effect. Here ω_C is the Compton frequency of the atoms used, and c is the speed of light in vacuum. The rotation sensitivity of such an AIG is restricted by the standard quantum limit (SQL), $\delta\Omega_G = c^2/2\omega_C\Theta\sqrt{N}$. This is a direct consequence of the Heisenberg uncertainty principle. Introducing entanglement in the system can enhance this precision upto the fundamental Heisenberg limit, $\Delta\phi = c^2/2\omega_C\Theta N$. Essentially, this can be interpreted as an AIG with a single particle of Compton frequency $N\omega_C$. Motivated by this, we explore the use of large number of particles treated as a single entity, first without entanglement in a collective state atomic interferometer (COSAIN), and then under spin squeezing in a Schrödinger cat atomic interferometer (SCAIN).

As a first step towards achieving this goal, we investigate the behavior of an ensemble of N non-interacting, identical atoms, excited by a laser with a wavelength of λ. In his seminal paper, R. H. Dicke showed that such an ensemble evolves into a superposition of $N+1$ symmetric states, $\{|E_0\rangle, |E_1\rangle, \ldots, |E_N\rangle\}$ under conditions that each atom experiences identical motion induced Doppler shift, and Rabi frequency. We show that when these ideal conditions are breached, i.e., the i-th atom experiences Rabi frequency Ω_i, and Doppler shift δ_i, the ensemble evolves into a superposition of $N+1$ symmetric, as well as $2^N - (N+1)$ asymmetric states. For a large value of N , the number of asymmetric states is far greater than that of the symmetric states. It is important to understand the behavior of all the collective states under various non-idealities for the realization of a COSAIN, as well as a collective state atomic clock (COSAC) - a device based on similar principles.

In this thesis, we show first how to formulate the properties of all the collective states under various non-idealities, and use this formulation to understand the dynamics thereof. We show that the collective states corresponding to the absorption of a given number of photons can be visualized as an abstract, multi-dimensional rotation in the Hilbert space spanned by the ordered product states of individual atoms. We also consider the effect of treating the center of mass degree of freedom of the atoms quantum mechanically on the description of the collective states. In particular, we show that it is indeed possible to construct a generalized collective state, as needed for the COSAIN, when each atom is assumed to be in a localized wave packet.

Based on the model of collective states developed thus far, we describe the COSAIN with the signal fringe as a function of ϕ, and therefore, Ω_G narrowed by $\sqrt{N}$ compared

to a conventional Raman atomic interferometer (CRAIN). This effect arises from the interferences among the collective states, and is a manifestation of interference at $2\pi\omega_C = 10^{40}$ Hz, de Broglie wavelength of 4.5×10^{-15} m, for $N = 10^6$ and $v = 1$ m/s. The population of the collective state of interest is detected by a null measurement scheme, in which an event corresponding to detection of zero photons corresponds to the system being in that particular collective state. The signal is detected by collecting fluorescence through stimulated Raman scattering of Stokes photons, which are emitted predominantly against the direction of the probe beam, for a high enough resonant optical density. The sensitivity of the ideal COSAIN is found to be given by the SQL. However, when detection efficiency and collection efficiency are taken into account, the detection scheme of the COSAIN increases the quantum efficiency of detection significantly in comparison to a typical CRAIN employing fluorescence detection, yielding a net improvement in stability by as much as a factor of 10. We discuss how the inhomogeneities arising from the non-uniformity in experimental parameters affect the COSAIN signal. We also describe an alternate experimental scheme to enhance resonant optical density in a COSAIN by using cross-linearly polarized counter-propagating Raman beams.

Finally, we explore the application of spin squeezing echo to surpass the SQL, and achieve Heisenberg scaling of rotation sensitivity in an AIG. We first review the spin representation of two-level atoms, and Coherent Spin States (CSS) which are equivalent of the Dicke collective states in this picture. The quantum fluctuations of a CSS are isotropic in the plane orthogonal to the direction of the mean spin. The application of spin squeezing to correlate the individual spins via a nonlinear interaction suppresses the quantum fluctuations along an orthogonal axis (to the mean spin) while inflating that

along the third axis, generating Squeezed Spin States. We describe the SCAIN, which is a COSAIN with Heisenberg scaling of phase sensitivity, enhanced by the application of squeezing echo. Explicitly, we employ what is known as the one axis twisting (OAT) spin squeezing on an initial CSS followed by a perturbation, at the end of which we seek to reverse the squeezing by switching the sign of the nonlinear interaction. In practice, this encourages increased interference between states with higher contrast in Compton frequency, resulting in the narrowing of signal fringe width by a factor $\sim N$.

The parameter of squeezing μ, which indicates length of interaction, dictates the signal fringe width, and therefore, $\delta\Omega_G$. However, this technique inherently depends on whether N is even or odd. For large ensembles, it is virtually impossible to determine this a priori. The protocol we describe here eliminates this complexity. At $\mu = \pi$, the well known Greenberger–Horne–Zeilinger (GHZ) states are obtained for even values of N. These states are pure cat states of an equal superposition of $|E_0\rangle$ and $|E_N\rangle$. The signal generated from the echo protocol in this regime is narrowed by a factor of N. On the contrary, odd values of N produce a null signal. In an actual experiment, the total signal is averaged over multiple runs, and leads to a signal halved in amplitude than what is expected for even N. The rotation sensitivity of the SCAIN in this regime is given by the Heisenberg limit. For values of $\mu < \pi$, both odd and even N generate almost identical signal fringes. We show that the SCAIN can attain a rotation sensitivity lower than the Heisenberg limit by a factor of $e^{-1/3}$ for interaction times significantly less than $\mu = \pi$.

Acknowledgements

”জানার মাঝে অজানারে করেছি সন্ধান”

This line from Rabindranath Tagore's celebrated *Gitabitan* that roughly translates to ”I have searched for the unknown within the realms of the known” sums up the time I have spent working under the aegis of Selim Shahriar. He is a gifted and willing teacher, whose optimism and encouragement has pushed me to see beyond the boundaries of my limited knowledge. I could not have dreamed of a more benevolent adviser to guide my research.

I would like to thank my committee members, John Ketterson and Brian Odom for their thought-provoking comments, which ignited impassioned debates and have led to several pivotal points in my research. I am also thankful to Phil Hemmer for his insights on the experimental aspects of developing the interferometer that shaped our vision for theoretical modeling.

It would be a matter of unfounded hubris to believe that my academic pursuits were mine alone. I would like to thank Yanfei Tu and Renpeng Fang for being my guides to the world of experimental optics when I first began in this field; Mohamed Fouda for being my live Matlab stackoverflow; Mehjabin Monjur, Minchuan Zhou and Zifan Zhou for their company during conferences and the much needed lighthearted conversations; Ye Wang and Subramanian Krishnamurthy for their constant career counseling even after they had long graduated; and Josh Yablon for supplying the funnies during the most serious situations. Over the course of exploring special relativity as a side project, I

had the privilege of getting acquainted with Daniel Villalon. I thank him for our long deliberations on logic and philosophy.

The environment at Northwestern fosters a spirit of engagement with the community. For this, I am grateful, in particular, to Penelope Warren at TGS for fiercely advocating for graduate students. Her unfaltering support has helped IGSSA thrive, and gifted me friends that I cherish. I also thank Mearah Quinn-Brauner for her patience and continuous encouragement when everything seemed to be failing.

I am thankful for the friends with whom I painted the town purple, particularly Chandrima, Sayantan, Abhishek, Aarohi, Vidya, Amneet, Karthik, Sankar, Rajlakshmi, Amit and Sanket. They have bequeathed upon me their love, sometimes in cooking for me, teaching me new recipes or even by their sheer presence on the other end of the phone.

This journey would have been more sensitive to phase change had it not been for the boisterous rallying of Varun, Srikanth, Breeta, Balachandra, Abhinendra, Shreyas, Sonam, Monalisa, Vatsala and Swapnil *in absentia*. Though thousands of miles have separated us, they have only ever been one phone call and several connecting flights away.

I am eternally indebted to my family - not only *ex officio*, but for unconditionally supporting my choices. To my sister, Madhura for being my first guinea pig when I wanted to teach mathematics. Despite being younger than me, she has on many an occasion reversed the role and awed me by the dignity in her endeavors. Her grit is a beacon of inspiration for me. I would have never developed the mettle for success had it not been for our wrestling matches. To Kunal, my brother-in-law for the love and enthusiasm with which he celebrates my tiny victories, and lends a compassionate ear on stormy days.

To my parents, Manisha and Rabindranath Sarkar, for encouraging me to weave my own dreams, and making sure that I don't ever give up on them. Many a time, it was only their relentless belief in me that fueled my work. Without their sacrifices and the humility that they have inculcated in their children, I would not have been able to achieve an iota of what I have. To my *other* family, Anwesha, Amritesh, Sarmishtha and Animesh Maitra, without whom I would not have even finished college, let alone receive a graduate education. To my mother-in-law, Usha Anil, whose appetite for learning has left me humbled.

Finally, I must acknowledge my husband, Robin Anil for the celebratory cup of tea on my acceptance at Northwestern many moons ago, and every step of the journey that has followed. No amount of gratitude suffices for the incredible patience with which he plays the sounding board to my usually vociferous, and sometimes unscientific rants. For this and more, I cannot thank him enough, and so I wouldn't.

List of abbreviations

ACS Asymmetric Collective States

AI Atomic Interferometer

AIG Atom Interferometric Gyroscope

COM Center of Mass

COSAIN Collective State Atomic Interferometer

COSAC Collective State Atomic Clock

CRAIN Conventional Raman Atomic Interferometer

CSS Coherent Spin States

GSO Gram-Schmidt Orthogonalization

HL Heisenberg Limit

MOT Magneto-Optical Trap

RFAC Ramsey Fringe Atomic Clock

RWA Rotating Wave Approximation

SCAIN Schrödinger Cat Atomic Interferometer

SCAC Schrödinger Cat Atomic Clock

SCS Symmetric Collective States

SQL Standard Quantum Limit

SSS Squeezed Spin States

Dedication

Dedicated to my grandparents, Sovana and Gokul Chandra Sanyal, Basana and Manendra Lal Sarkar, who sparked the flame of struggle in the face of immense adversities.

Contents

List of Figures

CHAPTER 1

Introduction

1.1. Brief History of Atom Interferometry

The primary goal of quantum metrology is to measure a physical quantity *very precisely*. In an atomic interferometer, atoms are split quantum mechanically, and each component is made to travel spatially separated trajectories. The separated components are then recombined to create an interference pattern that is sensitive to the phase difference accumulated by the atoms over their journey. The first demonstration of atomic interference in 1950 by N. F. Ramsey used the method of separated oscillatory fields with rf transitions and an atomic beam source [**1**]. This paved the way for realizing atom interferometers. In 1991, four groups demonstrated atom interferometry using entirely different approaches: gravity measurements using stimulated two-photon Raman transitions with three laser pulses in a $\pi/2 - \pi - \pi/2$ configuration [**2**, **3**], a Sagnac effect measurement using optical excitation with four traveling waves [**4**], a Mach-Zehnder interferometer using three nanofabricated mechanical gratings [**5**], and a Young's double-slit experiment [**6**]. Since then, atom interferometers have been demonstrated as gyroscopes and accelerometers [**7**, **8**], gravity gradiometers [**9**, **10**], matter-wave clocks [**11**] and may lead to a more accurate measurement of the fine structure constant [**12**, **13**]. They also form testbeds for measuring Newton's gravitational constant [**14**], gravitational red-shift [**15**] and for testing universality of free fall [**16**].

1.2. Organization of this Thesis

The rest of the thesis is organized in the following way. Chapter 2 presents a review of the fundamental concepts in atom interferometry theory. This chapter develops notation of the atomic model used throughout this thesis, outlines the derivation of Sagnac effect, and reviews the theoretical model of a Kasevich-Chu interferometer.

Chapter 3 presents an investigation of the collective behavior of an ensemble of non-interacting, identical atoms, excited by a laser. We show first how to formulate the properties of all the Dicke collective states under various non-idealities, and use this formulation to understand the dynamics thereof. We show that the collective states corresponding to the absorption of a given number of photons can be visualized as an abstract, multi-dimensional rotation in the Hilbert space spanned by the ordered product states of individual atoms. We also consider the effect of treating the center of mass degree of freedom of the atoms quantum mechanically on the description of the collective states. This analysis lays the framework that is essential for understanding the dynamics of the collective state atomic interferometer (COSAIN).

Chapter 4 deals with the details of the proposed N-atom COSAIN with the signal fringe as a function of phase-difference or rotation narrowed by $\sqrt{N}$ compared to a conventional interferometer. The details of the null measurement scheme for detecting a collective state of interest is outlined. We also describe an alternate experimental scheme to enhance resonant optical density in a COSAIN by using cross-linearly polarized counter-propagating Raman beams. The effect of inhomogeneities arising from the non-uniformity in experimental parameters discussed in Chapter 3 is investigated. We show that the rotation sensitivity of the COSAIN is given by the SQL. However, the

detection efficiency and collection efficiency from the null detection scheme increase the overall quantum efficiency of the COSAIN as compared to that of a conventional Raman atomic interferometer (CRAIN) by as much as a factor of 10.

Having established the fundamental properties and rotation sensitivity of the COSAIN, we explore the application of spin squeezing to exceed the SQL, and attain Heisenberg limited sensitivity, the ultimate limit to the performance of any quantum device. Chapter 5, presents an overview of the spin representation of two-level atoms. We establish the equivalence between the Dicke collective states and coherent spin states (CSS), and use that to review the CRAIN, and the SQL. We then review the concepts of one-axis twist (OAT) and two-axes counter-twist (TACT) spin squeezing.

In Chapter 6, we propose the Schrödinger cat atomic interferometer (SCAIN) to achieve the Heisenberg limit (HL) with very large N using the experimentally achievable one axis twist spin squeezing in combination with unsqueezing which results in the generation of Schrödinger cat states corresponding to an equal superposition of the extremal Dicke collective states. We describe a protocol which employs null detection of one of the collective states, producing fringes that are narrowed by a factor of N with unit visibility when N is even, and yields zero signal when N is odd. We show that for all N atoms, the sensitivity is below the HL by a factor of $\sqrt{2}$. We also show that a degree of sensitivity enhancement very close to this value can also be achieved for a much lower degree of squeezing than what is required for reaching the cat states. Finally, we note that the proposed scheme can also be used to realize a Heisenberg-limited Schrödinger cat atomic clock, for which the base frequency is effectively enhanced by a factor of N.

CHAPTER 2

Fundamentals of Atom Interferometry

This chapter is a review of the basic concepts involved in atom interferometry which lays the foundation for the rest of this dissertation. We will begin with the description of a two-level atom, and discuss the various considerations and approximations that are applied to derive a practical model. We will then extend this knowledge to a three-level atom in a Λ-configuration, which forms the building block of any atomic interferometer. Though elementary, this encapsulates the physics necessary for the development of the collective state atomic interferometers that form the heart of this research. More details about these atomic models can be found in [**17**–**21**]. Next, we will briefly review the Sagnac effect, and derive the expression for phase difference between the two arms of an interferometer. We will approach this using both the non-relativistic de Broglie wavelength, and the relativistic Compton frequency methods, and discuss their equivalence. Finally, we will use the concepts developed in the previous sections to describe the theory behind the Conventional Raman Atomic Interferometer (CRAIN).

2.1. Atom-Light Interaction

2.1.1. Two-Level Atom

An atom can be often modeled as a two-level system with wavefunction at time t given by

$$|\psi(t)\rangle = c_g(t)\,|g\rangle + c_e(t)\,|e\rangle\,, \tag{2.1}$$

where c_g and c_e are complex numbers, and $|g\rangle$ and $|e\rangle$ are stable or metastable quantum states with internal energies $\hbar\omega_g$ and $\hbar\omega_e$, respectively. This wavefunction must be normalized so that $\langle\psi|\psi\rangle = |c_g|^2 + |c_e|^2 = 1$. The two states are driven by a semiclassical laser with electric field $\mathbf{E}$ and wavelength λ propagating in the $\mathbf{z}$ direction, as shown in Fig. 2.1. An example of such a system is an alkali atom with two hyperfine ground states coupled by a microwave pulse. Assuming that the atom is moving along the $\mathbf{x}$ direction, the Hamiltonian of the atom-field system in the electric dipole approximation is given by

$$H = \frac{\mathbf{p}_z^2}{2m} + H_0 + q\rho \cdot \mathbf{E}, \tag{2.2}$$

where $\mathbf{p}_z$ is the center of mass (COM) momentum in the $\mathbf{z}$ direction, m is the mass of the atom, H_0 is the internal energy, q is the charge of the electron, ρ is the distance between the nucleus and the electron. The electric dipole approximation is valid for this system since $\lambda \gg \rho$.

The Hamiltonian, H and the wavefunction of the COM can be expanded in the basis of the eigenstates of the non-interacting Hamiltonian, $|i\rangle \otimes |p_z\rangle = |i, p_z\rangle$, where $i = g, e$. This forms the complete set of basis states for the present system. Since it is understood

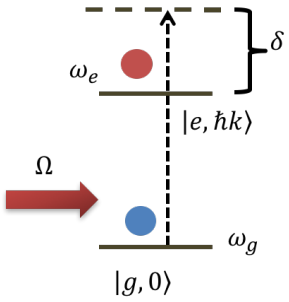

Figure 2.1. A two-level atom driven by a classical laser field.

that all momenta and positions refer to the **z**-direction, the z subscript on all momenta will be dropped henceforth. The identity operator can be written in terms of this basis as

$$\hat{I} = \int \mathrm{d}p \sum_i |i,p\rangle \langle i,p| \tag{2.3}$$

The matrix elements of the form $\langle i| \rho |i\rangle$ are assumed to be zero. Thus, in terms of the dipole matrix elements $\mathbf{d}_{ij} = \langle i| \rho |j\rangle$, the position operator can be written as

$$\begin{aligned} \rho &= \int \mathrm{d}p \int \mathrm{d}p' \sum_{i,j} |i,p\rangle \langle i,p| \rho |j,p'\rangle \langle j,p'| \\ &= \int \mathrm{d}p (\mathbf{d}_{ge} |g,p\rangle \langle e,p| + \mathbf{d}_{eg} |e,p\rangle \langle g,p|). \end{aligned} \tag{2.4}$$

The atomic raising and lowering operators are defined as

$$\sigma_{ij} = |i,p\rangle \langle j,p| . \tag{2.5}$$

The position operator in terms of the above operators is

$$\rho = \int \mathrm{d}p(\mathbf{d}_{ge}\sigma_{ge} + \mathbf{d}_{eg}\sigma_{eg}). \tag{2.6}$$

Since the electric field is modeled semiclassically, it can be written as

$$\begin{aligned}\mathbf{E}(z,t) &= \mathbf{E}_0\cos(\omega t - k\hat{z} + \phi) \\ &= \frac{\mathbf{E}_0}{2}(\mathrm{e}^{\mathrm{i}(\omega t - k\hat{z}+\phi)} + \mathrm{e}^{-\mathrm{i}(\omega t - k\hat{z}+\phi)}),\end{aligned} \tag{2.7}$$

where $\omega = 2\pi c\lambda^{-1}$, and $\hat{z}$ is the operator associated with the COM position of the atom. The dipole matrix elements are assumed to be real, so that $\mathbf{d}_{ge} = \mathbf{d}_{eg}$. Thus,

$$\begin{aligned}\rho\cdot\mathbf{E} &= \int \mathrm{d}p\frac{\mathbf{d}_{ge}\cdot\mathbf{E}_0}{2}\left(\sigma_{ge}\left(\mathrm{e}^{\mathrm{i}(\omega t - k\hat{z}+\phi)} + \mathrm{e}^{-\mathrm{i}(\omega t - k\hat{z}+\phi)}\right) + \sigma_{eg}\left(\mathrm{e}^{\mathrm{i}(\omega t - k\hat{z}+\phi)} + \mathrm{e}^{-\mathrm{i}(\omega t - k\hat{z}+\phi)}\right)\right) \\ &= \int \mathrm{d}p\frac{\mathbf{d}_{ge}\cdot\mathbf{E}_0}{2}\left(\sigma_{ge}\left(\mathrm{e}^{\mathrm{i}(\omega t - k\hat{z}+\phi)} + \mathrm{e}^{-\mathrm{i}(\omega t - k\hat{z}+\phi)}\right) + h.c.\right),\end{aligned} \tag{2.8}$$

where $h.c.$ denotes the Hermitian conjugate term.

For the electric dipole approximation to hold true, the electric field must be close to resonance with the atomic transition, i.e., $\omega - \omega_0 = \delta \approx 0$, where $\omega_0 = \omega_e - \omega_g$, and c is the speed of light in vacuum. Therefore, $\omega + \omega_0 \gg \omega - \omega_0$. Therefore, Eq. 2.8 can be rewritten as

$$\rho\cdot\mathbf{E} = \int \mathrm{d}p\frac{\mathbf{d}_{ge}\cdot\mathbf{E}_0}{2}\left(\sigma_{ge}\mathrm{e}^{\mathrm{i}\omega_0 t}\left(\mathrm{e}^{\mathrm{i}(\delta t - k\hat{z}+\phi)} + \mathrm{e}^{-\mathrm{i}((\omega+\omega_0)t - k\hat{z}+\phi)}\right) + +h.c.\right). \tag{2.9}$$

The term $\mathrm{e}^{-\mathrm{i}((\omega+\omega_0)t - k\hat{z}+\phi)}$ oscillates rapidly, and thus averages to zero over an appreciable time scale. Under the rotating wave approximation (RWA), these terms are neglected,

and the interaction Hamiltonian can be expressed as

$$\rho \cdot \mathbf{E} = \int \mathrm{d}p \frac{\mathbf{d}_{ge} \cdot \mathbf{E}_0}{2} \left(\sigma_{ge} \mathrm{e}^{\mathrm{i}(\omega t - k\hat{z} + \phi)} + h.c. \right) \tag{2.10}$$

The position dependent phase of the electric field can be expanded in the basis of the eigenstates as follows

$$\begin{aligned}
\mathrm{e}^{\mathrm{i}k\hat{z}} &= \sum_{i,j} \int \mathrm{d}p \int \mathrm{d}p' \left|i,p\right\rangle \left\langle i,p\right| \mathrm{e}^{\mathrm{i}kz} \left|j,p'\right\rangle \left\langle j,p'\right| \\
&= \sum_{i,j} \int \mathrm{d}p \int \mathrm{d}p' \left|i,p\right\rangle \left\langle i,p\right| \left|i,z\right\rangle \left\langle i,z\right| \mathrm{e}^{\mathrm{i}kz} \left|j,z'\right\rangle \left\langle j,z'\right| \left|j,p'\right\rangle \left\langle j,p'\right| \\
&= \sum_{i,j} \int \mathrm{d}p \int \mathrm{d}p' \left|i,p\right\rangle \mathrm{e}^{\frac{-\mathrm{i}pz}{\hbar}} \mathrm{e}^{\mathrm{i}kz'} \mathrm{e}^{\frac{\mathrm{i}p'z'}{\hbar}} \delta_{ij} \delta(z - z') \left\langle j,p'\right| \\
&= \sum_{i} \int \mathrm{d}p \left|i,p\right\rangle \left\langle i,p - \hbar k\right| . \qquad (2.11)
\end{aligned}$$

Similarly,

$$\mathrm{e}^{-\mathrm{i}k\hat{z}} = \sum_{i} \int \mathrm{d}p \left|i,p\right\rangle \left\langle i,p + \hbar k\right| . \tag{2.12}$$

The non-interacting part of the Hamiltonian in Eq. 2.2, H_0 may be expanded in terms of this basis as

$$H_0 = \int \mathrm{d}p \sum_i \left(\frac{p^2}{2m} + \hbar\omega_i \right) \sigma_{ii}. \tag{2.13}$$

The complete Hamiltonian in the $|p,i\rangle$ basis is derived by combining Eq. 2.10, Eq. 2.11, and Eq. 2.12:

$$H = \int \mathrm{d}p \Bigg(\sum_i \Big(\frac{p^2}{2m} + \hbar\omega_i \Big) \sigma_{ii} + \frac{\hbar\Omega}{2} \Big(\sigma_{ge} \left|g,p\right\rangle \left\langle e,p+\hbar k\right| \mathrm{e}^{\mathrm{i}(\omega t+\phi)} \\ + \sigma_{eg} \left|e,p+\hbar k\right\rangle \left\langle g,p\right| \mathrm{e}^{-\mathrm{i}(\omega t+\phi)} \Big) \Bigg), \tag{2.14}$$

where $\Omega \equiv q\mathbf{d}_{ge} \cdot \mathbf{E}_0/\hbar$ is the strength of the Rabi oscillations.

It is evident from Eq. 2.14 that the transition $|g,p\rangle \leftrightarrow |e,p+\hbar k\rangle$ is only possible when accompanied by the momentum transition indicated. Therefore, the dynamics of the atom can be succinctly described by considering a single manifold of the momentum p. This aspect of the quantization of the COM of the atom is discussed in detail in Chapter 3. Thus, the present discussion will be restricted to $p = 0$, and can be later generalized and integrated over all momenta to derive the motion of the wavepacket as a whole. For the sake of brevity, the momentum components of the basis states are condensed so that $|g\rangle \equiv |g,0\rangle$ and $|e\rangle \equiv |e,\hbar k\rangle$

The evolution of the atom over time t is dictated by the Schrödinger equation,

$$\mathrm{i}\hbar\partial_t \left|\psi(t)\right\rangle = H \left|\psi(t)\right\rangle . \tag{2.15}$$

A unitary transformation, Q converts $|\psi\rangle$ to an interaction-picture state vector $|\psi'\rangle = Q\,|\psi\rangle$, where Q is defined as

$$Q = \sum_{i=1}^{2} \mathrm{e}^{i(a_i t+b_i)} \left|i\right\rangle \left\langle i\right| , \tag{2.16}$$

where a_i and b_i are arbitrary parameters. The Hamiltonian for $|\psi'\rangle$ is then

$$H' = QHQ^{-1} - \hbar(\partial_t Q)Q^{-1}, \tag{2.17}$$

which dictates the evolution of $|\psi'\rangle$ according to Eq. 2.15. To render H' time independent, we set $a_g = \omega_g$ and $a_e = \omega + \omega_g$. Now, setting $b_g = 0$, $b_e = \phi$ makes H' independent of any phase factor as well. In this frame, the Q-transformed Hamiltonian thus becomes

$$H = \hbar\left(\frac{\Omega}{2}(|g',0\rangle\langle e',\hbar k| + |e',\hbar k\rangle\langle g',0|) - \left(\delta - \frac{\hbar k^2}{2m}\right)|e',\hbar k\rangle\langle e',\hbar k|\right) \tag{2.18}$$

The new basis vectors, $|g',0\rangle$ and $|e',\hbar k\rangle$, are related to the original basis vectors as $\mathrm{e}^{-\mathrm{i}\omega_g t}|g,0\rangle$ and $\mathrm{e}^{-\mathrm{i}((\delta+\omega_e)t)+\phi}|e,\hbar k\rangle$, respectively. Assuming that the atom is initially in $c_g(0)|g'\rangle + c_e(0)|e'\rangle$, its quantum state can be written as

$$\begin{aligned}|\psi'\rangle =& \mathrm{e}^{\mathrm{i}\delta' t/2}((c_g(0)\cos\left(\frac{\Omega' t}{2}\right) - \mathrm{i}\frac{c_g(0)\delta' + c_e(0)\Omega}{\Omega'}\sin\left(\frac{\Omega' t}{2}\right))|g'\rangle \\ &+(-\mathrm{i}\frac{c_g(0)\Omega - c_e(0)\delta'}{\Omega'}\sin\left(\frac{\Omega' t}{2}\right) + c_e(0)\cos\left(\frac{\Omega' t}{2}\right))|e'\rangle),\end{aligned} \tag{2.19}$$

where $\delta' = \delta - \hbar k^2/2m$ is the effective detuning of the atom, and $\Omega' = \sqrt{\Omega^2 + \delta'^2}$ is the effective coupling frequency. In the case where the detuning of the field is matched perfectly with the detuning arising from the COM momentum of the atom, i.e. $\delta = \hbar k^2/2m$, the state of the atom is given by

$$\begin{aligned}|\psi'\rangle =& \left(c_g(0)\cos\left(\frac{\Omega t}{2}\right) - \mathrm{i}c_e(0)\sin\left(\frac{\Omega t}{2}\right)\right)|g'\rangle \\ &+ \left(-\mathrm{i}c_g(0)\sin\left(\frac{\Omega t}{2}\right) + c_e(0)\cos\left(\frac{\Omega t}{2}\right)\right)|e'\rangle\,.\end{aligned} \tag{2.20}$$

In the case where no external field is applied to the atom so that $\Omega = 0$, the atom is in the state $|\psi'\rangle = c_g(0)\,|g'\rangle + \exp(i\delta' t)c_e(0)\,|e'\rangle$. Thus, even during a dark zone, the atom is affected by non-zero detuning while the population of the states remain unchanged. The atom-field system can, in theory, be controlled by changing δ and Ω. This forms the basis of several atomic devices, eg., Ramsey fringe clocks [**22**], Bordé-Chu interferometers [**2**,**23**], etc.

2.1.2. Three-Level Atom

Here, we will review the basic concepts of a three-level atomic model. We will show how it can be reduced to an equivalent two-level model for compact representation in an atomic interferometer. A three-level atom in the Λ-configuration undergoing Raman transitions driven by two counter-propagating semiclassical laser forms the building block of the conventional Raman atomic interferometer (CRAIN) [**2**]. The two metastable states, $|p, g\rangle$ and $|p, e\rangle$ and an excited state $|p, a\rangle$ are coupled by two counter propagating beams of wavelengths λ_1 and λ_2, respectively, as shown in Fig. 2.2(a)). The Hamiltonian for this system can be written as

$$H = \frac{\mathbf{p}_z^2}{2m} + H_0 + q\rho \cdot \mathbf{E}_1 + q\rho \cdot \mathbf{E}_2, \tag{2.21}$$

where $\mathbf{E}_1$ and $\mathbf{E}_2$ are the electric field vectors of the lasers coupling $|g, p\rangle$ to $|a, p\rangle$, and $|a, p\rangle$ to $|e, p\rangle$, respectively. Drawing analogy from Eq. 2.4, the position operator can be

written as

$$\rho = \int \mathrm{d}p(\mathbf{d}_{ga}\,|g,p\rangle\,\langle a,p| + \mathbf{d}_{ag}\,|a,p\rangle\,\langle g,p| + \mathbf{d}_{ea}\,|e,p\rangle\,\langle a,p| + \mathbf{d}_{ae}\,|a,p\rangle\,\langle e,p|)$$

$$= \int \mathrm{d}p(\mathbf{d}_{ga}\sigma_{ga} + \mathbf{d}_{ag}\sigma_{ag} + \mathbf{d}_{ea}\sigma_{ea} + \mathbf{d}_{ae}\sigma_{ae}). \tag{2.22}$$

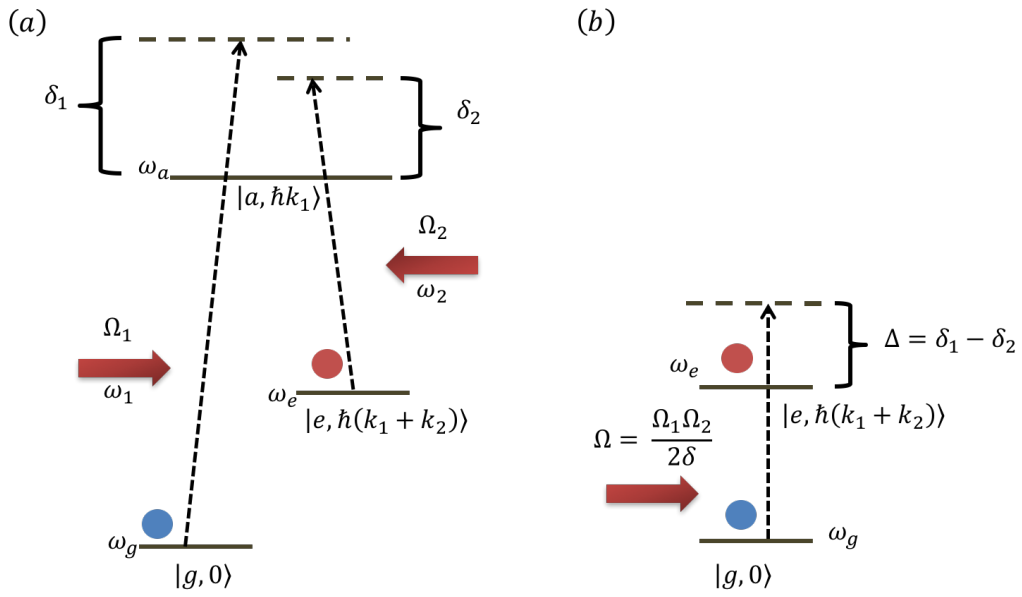

Figure 2.2. (a) A three level atom. (b) An equivalent reduced two-level atom model.

Each semiclassical laser field can be expressed as $\mathbf{E}_j(z,t) = \mathbf{E}_{0j}\cos(\omega_j t - k_j\hat{z} + \phi_j)$, $j = 1, 2$. The field, $\mathbf{E}_1$ interacts only with that part of the electron position operator which induces the transition $|g\rangle \leftrightarrow |a\rangle$, and $\mathbf{E}_2$ interacts only with that part which causes the transition $|a\rangle \leftrightarrow |e\rangle$. Upon making the RWA to eliminate the terms which do not

conserve energy, we get

$$\rho \cdot \mathbf{E}_1 = \int \mathrm{d}p \Bigg(\frac{\mathbf{d}_{ga} \cdot \mathbf{E}_{01}}{2} \left(\sigma_{ga} \mathrm{e}^{\mathrm{i}(\omega_1 t - k_1 \hat{z} + \phi_1)} + \sigma_{ag} \mathrm{e}^{-\mathrm{i}(\omega_1 t - k_1 \hat{z} + \phi_1)} \right) + \frac{\mathbf{d}_{ea} \cdot \mathbf{E}_{02}}{2} \left(\sigma_{ea} \mathrm{e}^{\mathrm{i}(\omega_2 t - k_2 \hat{z} + \phi_2)} + \sigma_{ae} \mathrm{e}^{-\mathrm{i}(\omega_2 t - k_2 \hat{z} + \phi_2)} \right) \Bigg). \tag{2.23}$$

From Eq. 2.11 and Eq. 2.12 we get $\mathrm{e}^{\mathrm{i}k_j \hat{z}} = \sum_i \int \mathrm{d}p \, |i, p\rangle \langle i, p - \hbar k_j|$ and $\mathrm{e}^{-\mathrm{i}k_j \hat{z}} = \sum_i \int \mathrm{d}p \, |i, p\rangle \langle i, p - \hbar k_j|$, $j = 1, 2$. Finally, the full Hamiltonian in the $|i, p\rangle$ basis is

$$\begin{aligned} H = \int \mathrm{d}p \Bigg(\sum_i \left(\frac{p^2}{2m} + \hbar \omega_i \right) \sigma_{ii} + \frac{\hbar \Omega_1}{2} \Big(& |g, p\rangle \langle a, p + \hbar k_1| \, \mathrm{e}^{\mathrm{i}(\omega_1 t + \phi_1)} \\ & + |a, p + \hbar k_1\rangle \langle g, p| \, \mathrm{e}^{-\mathrm{i}(\omega_1 t + \phi_1)} \Big) + \frac{\hbar \Omega_2}{2} \Big(|e, p\rangle \langle a, p + \hbar k_2| \, \mathrm{e}^{\mathrm{i}(\omega_2 t + \phi_2)} \\ & + |a, p + \hbar k_2\rangle \langle e, p| \, \mathrm{e}^{-\mathrm{i}(\omega_2 t + \phi_2)} \Big) \Bigg), \end{aligned} \tag{2.24}$$

where $\Omega_1 \equiv q \mathbf{d}_{ga} \cdot \mathbf{E}_{01}/\hbar$ and $\Omega_2 \equiv q \mathbf{d}_{ea} \cdot \mathbf{E}_{02}/\hbar$

As discussed in Sec. 2.1.1, the Hamiltonian H creates only the following transitions: $|g, p\rangle \leftrightarrow |a, p + \hbar k_1\rangle \leftrightarrow |e, p + \hbar k_1 + \hbar k_2\rangle$, for a given value of p. Therefore, the following substitutions for momentum variables are made

$$\begin{aligned} \int \mathrm{d}p \left(\frac{p^2}{2m} + \hbar \omega_a \right) |a, p\rangle \langle a, p| = \int \mathrm{d}q_1 \Bigg(& \frac{(q_1 + \hbar k_1)^2}{2m} + \hbar \omega_a \Bigg) \\ & \times |a, q_1 + \hbar k_1\rangle \langle a, q_1 + \hbar k_1| \, , \end{aligned} \tag{2.25a}$$

$$\begin{aligned} \int \mathrm{d}p \left(\frac{p^2}{2m} + \hbar \omega_e \right) |e, p\rangle \langle e, p| = \int \mathrm{d}q_2 \Bigg(& \frac{(q_2 + \hbar k_1 - \hbar k_2)^2}{2m} + \hbar \omega_e \Bigg) \\ & \times |e, q_2 + \hbar k_1 - \hbar k_2\rangle \langle e, q_2 + \hbar k_1 - \hbar k_2| \, , \end{aligned} \tag{2.25b}$$

$$\int \mathrm{d}p \, |e,p\rangle \langle a, p+\hbar k_2| = \int \mathrm{d}q_2 \, |e, q_2+\hbar k_1-\hbar k_2\rangle \langle a, q_2+\hbar k_1| \,. \tag{2.25c}$$

Thus, Eq. 2.24 can be rewritten as

$$\begin{aligned} H = \int \mathrm{d}p \Bigg(& \sum_i \hbar\omega_i' \sigma_{ii} + \frac{\hbar\Omega_1}{2}\Big(|g\rangle \langle a| \, \mathrm{e}^{\mathrm{i}(\omega_1 t+\phi_1)} + |a\rangle \langle g| \, \mathrm{e}^{-\mathrm{i}(\omega_1 t+\phi_1)} \Big) \\ & + \frac{\hbar\Omega_2}{2}\Big(|e\rangle \langle a| \, \mathrm{e}^{\mathrm{i}(\omega_2 t+\phi_2)} + |a\rangle \langle e| \, \mathrm{e}^{-\mathrm{i}(\omega_2 t+\phi_2)} \Big) \Bigg), \end{aligned} \tag{2.26}$$

where ω_i' is the sum of internal energy and COM motion energy of the i-th state. Here, the momentum components of the basis states have been dropped for the sake of brevity, and represent $|g\rangle \equiv |g,p\rangle$, $|a\rangle \equiv |a, p+\hbar k_1\rangle$, and $|e\rangle \equiv |e, p+\hbar k_1-\hbar k_2\rangle$. It is evident from the above Hamiltonian that the only transitions allowed for the atom at momentum p are those governed by these particular momentum changes. Thus, it is sufficient to consider only a single manifold of p to describe the dynamics of the atom. As such, it is sufficient to restrict to $p = 0$ for the purpose of this section. The resulting Hamiltonian is, therefore,

$$\begin{aligned} H = {} & \hbar\omega_g' |g\rangle \langle g| + \hbar\omega_a' |a\rangle \langle a| + \hbar\omega_e' |e\rangle \langle e| + \frac{\hbar\Omega_1}{2}\Big(|g\rangle \langle a| \, \mathrm{e}^{\mathrm{i}(\omega_1 t+\phi_1)} + |a\rangle \langle g| \, \mathrm{e}^{-\mathrm{i}(\omega_1 t+\phi_1)} \Big) \\ & + \frac{\hbar\Omega_2}{2}\Big(|e\rangle \langle a| \, \mathrm{e}^{\mathrm{i}(\omega_2 t+\phi_2)} + |a\rangle \langle e| \, \mathrm{e}^{-\mathrm{i}(\omega_2 t+\phi_2)} \Big) \end{aligned} \tag{2.27}$$

The laser beams are far detuned from resonances. These detunings are defined with respect to energies of the states as follows

$$\delta_1 = \omega_1 - (\omega_a' - \omega_g'), \tag{2.28a}$$

$$\delta_2 = \omega_2 - (\omega'_a - \omega'_e). \tag{2.28b}$$

The state of the atom, $|\psi(t)\rangle = c_g(t)\,|g\rangle + c_a(t)\,|a\rangle + c_e(t)\,|e\rangle$, evolves according to the Schrödinger equation in Eq. 2.15. The unitary transformation to rid $|\psi(t)\rangle$ of its time and phase dependence is of the form given in Eq. 2.16, where $i = 1, 2, 3$. The evolution of the transformed state vector $|\psi'\rangle = c'_g(t)\,|g'\rangle + c'_a(t)\,|a'\rangle + c'_e(t)\,|e'\rangle$ is governed by the Hamiltonian H', where $H' = QHQ^{-1} - \hbar(\partial_t Q)Q^{-1}$. The time dependence of H' is eliminated by setting $a_i = \omega'_g$, $a_2 = \omega'_a + \delta + \Delta/2$, and $a_3 = \omega'_e + \Delta$, where $\delta = (\delta_1 + \delta_2)/2$, and $\Delta = \delta_1 - \delta_2$. Setting $b_1 = 0$, $b_2 = -\phi_1$, and $b_3 = -(\phi_1 + \phi_2)$ removes the phase dependence of H'. The Q-transformed Hamiltonian is thus,

$$\begin{aligned} H' =& \hbar\Bigg(\left(-\delta - \frac{\Delta}{2}\right)|a'\rangle\langle a'| - \Delta\,|e'\rangle\langle e'| \\ &+ \frac{\Omega_1}{2}(|g'\rangle\langle a'| + |a'\rangle\langle g'|) + \frac{\Omega_2}{2}(|e'\rangle\langle a'| + |a'\rangle\langle e'|)\Bigg). \end{aligned} \tag{2.29}$$

The transformed basis vectors are related to the original vectors as: $|g'\rangle = \mathrm{e}^{-i(\omega_g + \Delta/2)t}\,|g\rangle$, $|a'\rangle = \mathrm{e}^{-i((\omega_a+\delta)t - \phi_1)}\,|a\rangle$, and $|e'\rangle = \mathrm{e}^{-i((\omega_e+\Delta/2)t - (\phi_1+\phi_2))}\,|e\rangle$. The equation of motion for these states are

$$\mathrm{i}\dot{c'_g}(t) = \frac{\Omega_1}{2}c'_a(t), \tag{2.30a}$$

$$\mathrm{i}\dot{c'_a}(t) = \frac{\Omega_1}{2}c'_g(t) - \left(\delta + \frac{\Delta}{2}\right)c'_a(t) + \frac{\Omega_2}{2}c'_e(t), \tag{2.30b}$$

$$\mathrm{i}\dot{c'_e}(t) = \frac{\Omega_2}{2}c'_a(t) - \Delta c'_e(t). \tag{2.30c}$$

Since $|\delta_1|, |\delta_2| \gg 0$, the adiabatic approximation is applied at this point to reduce the three-level system to a two-level system. This approximation is accomplished by assuming that the population of the intermediate state $|a'\rangle$ is negligible, and $\dot{c'_e}(t)$ can be set to zero, and solving for $c'_a(t)$ in Eq. 2.30b as follows

$$\mathrm{i}\dot{c'_g}(t) = \frac{\Omega_1^2}{4\left(\delta + \frac{\Delta}{2}\right)} c'_g(t) + \frac{\Omega_1\Omega_2}{4\left(\delta + \frac{\Delta}{2}\right)} c'_e(t), \tag{2.31a}$$

$$\mathrm{i}\dot{c'_e}(t) = \frac{\Omega_1\Omega_2}{4\left(\delta + \frac{\Delta}{2}\right)} c'_g(t) + \left(-\Delta + \frac{\Omega_2^2}{4\left(\delta + \frac{\Delta}{2}\right)}\right) c'_e(t). \tag{2.31b}$$

These represent the equations of motion of a reduced two-level system driven by a single pulse of strength

$$\Omega = \frac{\Omega_1\Omega_2}{2(\delta + \Delta/2)}, \tag{2.32}$$

as depicted in Fig. 2.2(b). Assuming that the strength of the two counter-propagating lasers are almost equal, $\Omega_1 = \Omega_2$, and that $\delta \gg \Delta$, we get the Hamiltonian of the effective two-level system

$$H_{red} = \hbar\left(\frac{\Omega}{2}(|g'\rangle\langle e'| + |e'\rangle\langle g'|) - \Delta\,|e'\rangle\langle e'|\right). \tag{2.33}$$

The state of this system at time t is given by Eq. 2.19, by replacing δ' with Δ.

2.2. Sagnac Effect

The precise measurement of rate of rotation harnessing the Compton frequency of atoms is the central thesis of this research. The Sagnac effect was originally proposed

to demonstrate the phase shift arising from rotation in an optical interferometer [**24**]. A schematic representation of his interferometer is given in Fig. 2.3(a). The fringes observed at the detection port are affected by any phase difference, ϕ between the two paths.

For the sake of simplicity, a circular interferometer of radius r is considered. A generalized approach using Feynman path integrals for loops of arbitrary configuration is given in [**25**]. An incoming wave is split at point A, and directed to two counter-propagating paths, as shown in Fig 2.3(b). The velocity of the wave in the rest frame is v. The time required for the waves traveling along the clockwise and counter-clockwise paths to arrive at the detector at point D are the same, by symmetry. However, this symmetry is broken if the interferometer is rotating with angular velocity Ω_G about an axis normal to the plane of the loop and passing through its center. The phase shift elicited from this difference in arrival times can be calculated via two different approaches. In the following text, the non-relativistic, and more common approach is discussed first, followed by the method of relativistic addition of velocities.

2.2.1. Non-Relativistic Method

The wave traveling against the direction of rotation travels a shorter path, and arrives first at the detector, at time t_-. On the other hand, the wave traveling along the direction of rotation arrives at the detector later at t_+, since it travels a longer path. The travel times are given by

$$vt_- = \pi r - \Omega_G r t_-, \tag{2.34a}$$

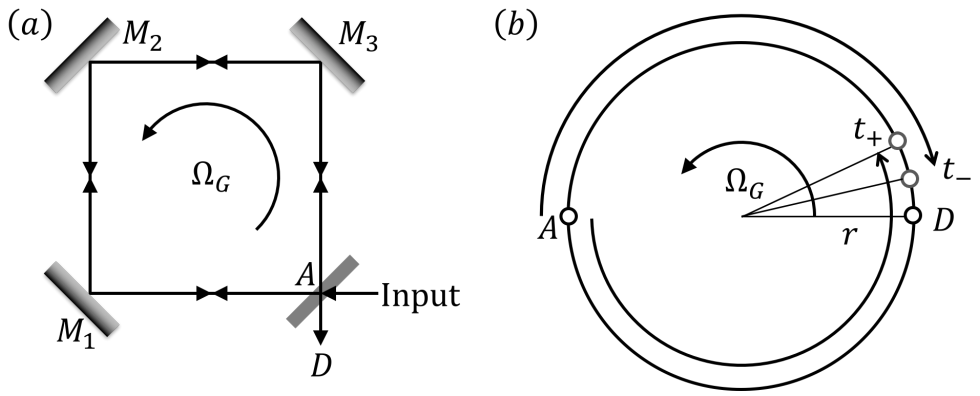

Figure 2.3. (a) Diagram of Sagnac's original Mach-Zehnder type interferometer. An incoming light beam is split into two beams by the beam-splitter, A. Two counter-propagating beams then circulate the interferometer. The beams interfere at A. There are two detection ports, one back towards the input, the other towards the detector. (b) Waves leaving a beam-splitter at A and traversing the interferometer in opposite directions until detection at D, which is also moving with the loop, at times t_- andt_+ depending on the direction of travel.

(2.34b) $$vt_+ = \pi r + \Omega_G r t_+.$$

Therefore, the time difference between the two counter-propagating waves is given by

(2.35) $$\Delta t = t_+ - t_- = \frac{2A\Omega_G}{v^2 - \Omega_G^2 r^2},$$

where A is the area of the loop enclosed by the interferometer. For slow rotation rates, which fall under the regime in which the majority of the atomic interferometers operate, $\Delta t = 2A\Omega_G/v^2$. The phase difference between the two paths is given by $\phi = v\Delta t/\lambda$, where λ is the wavelength of the wave. For massive particle, λ is the de Broglie wavelength, $\lambda_{dB} = 2\pi\hbar/mv$, where m is the mass of the particle. Therefore, the phase shift between

the paths can be written as

$$\phi = \frac{2mA\Omega_G}{\hbar}. \tag{2.36}$$

Thus, for a massive particle, the phase shift is independent of the velocity with which it is traveling.

2.2.2. Relativistic Method

This method invokes the relativistic addition of velocities to determine the time lag in the arrival of the two branches of the wave. The relative velocity of the wave moving against the direction of rotation of the interferometer is given by

$$v_- = \frac{v - r\Omega_G}{1 - vr\Omega_G/c^2}, \tag{2.37}$$

c being the speed of light in vacuum. Similarly, the relative velocity of the wave moving along the direction of rotation of the interferometer is

$$v_+ = \frac{v + r\Omega_G}{1 + vr\Omega_G/c^2}. \tag{2.38}$$

The travel times of each of these waves before arriving at the detector, D are

$$v_-t_- = \pi r - \Omega_G r t_-, \tag{2.39a}$$

$$v_+t_+ = \pi r + \Omega_G r t_+, \tag{2.39b}$$

Therefore, the time difference is given by

$$\Delta t = \frac{2A\Omega_G}{c^2(1-(r\Omega_G)^2/c^2)}. \tag{2.40}$$

The phase difference between the paths is given by $\phi = \omega\Delta t$, where ω is the angular frequency of the wave. For a massive particle, this frequency is the Compton frequency, $\omega_C = mc^2/\hbar$. Therefore, for slow rotation rates, the phase shift between the paths can be written as

$$\phi = \frac{2mA\Omega_G}{\hbar}. \tag{2.41}$$

A more rigorous derivation of the Sagnac effect involves the application of general relativity [**26**]. In the present context of atomic interferometers, the application of special relativity suffices.

2.2.3. Equivalence of the Two Approaches

The two approaches described in Sec. 2.2.1 and Sec 2.2.2 are equivalent due to the fact that λ_{dB} is the laboratory-frame manifestation of the ω_C induced phase variation in the rest-frame of the atom [**11**,**27**–**29**]. To understand this without loss of generality, consider the direction of the velocity of the particle as $\hat{\mathbf{x}}$. For non-relativistic velocities, mixing between the spinors can be ignored, and the phase factor of a positive energy spinor, in the rest frame of the particle, is given simply as $\exp(-i\phi)$, where $\phi = \omega_C\tau$ with τ being the proper time. The phase, ϕ, is a Lorentz invariant parameter, and can in general be written as a contraction between the position four vector x^μ and momentum four vector $\hbar k^\mu : \phi = k_\mu x^\mu$. In the rest frame of the particle, the position four-vector is $x^\mu =$

$\{c\tau, 0, 0, 0\}$ and the momentum four vector is $\hbar k^\mu = \hbar\{\omega_C/c, 0, 0, 0\}$. In the laboratory frame, the position four vector is, by definition, $x^\mu = \{ct, 0, 0, 0\}$, and application of Lorentz transform shows that the momentum four vector is $\hbar k^\mu = \hbar\{\omega'_C/c, k_{dB}, 0, 0\}$, where $k_{dB} = \gamma mv/\hbar = 2\pi/\lambda_{dB}$ and the phase factor becomes $\phi = \omega'_C t - k_{dB}x$. Again, in the non-relativistic limit, $\gamma \approx 1$ and we get $\lambda_{dB} \approx 2\pi\hbar/mv$. Thus, the de Broglie wavelength is simply the laboratory frame manifestation of the phase variation in the rest frame due to the Compton frequency.

2.3. Conventional Raman Atomic Interferometer

This section gives an overview of the theory behind the Conventional Raman Atomic Interferometer (CRAIN) which is based on the Kasevich-Chu interferometer [**2**]. The quantum state transitions that take place in an interferometer, leading to the observation of phase dependent signal fringes, are worked out. This is necessary for understanding the collective state atomic interferometer (COSAIN) which operates on the same basic principles [**30**], but has properties that differ significantly from a CRAIN employing the same $\pi/2 - \pi - \pi/2$ sequence.

An atomic interferometer is based on the principle that two or more intermediate states evolving from an initial quantum state are not uniquely distinguishable by a measurement process:

$$|\psi\rangle \rightarrow |g\rangle + |e\rangle\,. \tag{2.42}$$

The probability of finding the atom in $|\psi_f\rangle$ is given by the expectation value of the projection operator $|\psi_f\rangle\langle\psi_f|$ as follows

$$\langle|\psi_f\rangle\langle\psi_f|\rangle = |\langle g|\psi_f\rangle|^2 + |\langle e|\psi_f\rangle|^2 + 2\mathrm{Re}\{\langle\psi_f|g\rangle\langle e|\psi_f\rangle\}. \tag{2.43}$$

The interference is observed due to the cross-term, which carries the signature of the phase difference between the states $|g\rangle$ and $|e\rangle$.

A three-level atom of the type described in Sec. 2.1.2 is initially prepared in the state $|g, p_z = 0\rangle \equiv |g, 0\rangle$. The atom is assumed to be initially situated at $(x = 0, z = 0)$ and traveling along the **x**-direction with a velocity v. Three pairs of counter-propagating laser beams with rectangular intensity profile form the splitting-reflecting-combining sequence of an interferometer. It is assumed that the single-photon detuning of the beams is considerably greater than the Rabi frequencies of the beams, i.e., $\delta \gg \Omega_1, \Omega_2$. Therefore, the atom-laser interaction can be effectively described as a reduced two-level system with states $|g, 0\rangle$ and $|e, \hbar k\rangle$ excited by an effective traveling wave with a momentum $\hbar k = \hbar(k1 + k2)$, and a Rabi frequency given by Eq. 2.32 (Fig. 2.2 (b)). It is also assumed that $\delta \gg \Gamma$, where Γ is the decay rate of $|a\rangle$, so that the effect of Γ can be neglected.

For simplicity, we assume for now that $\Delta \ll \Omega$, so that its effect can be ignored during the laser-atom interactions. The more rigorous treatment that takes into account the effect of Δ is given in Chapter 4. At $t = 0$, a first $\pi/2-$pulse of duration τ is applied to the atoms, such that $\Omega\tau = \pi/2$. The state of each atom at the end of the pulse is given by Eq. 2.20

$$|\psi(\tau)\rangle = \frac{|g\rangle - i\,|e\rangle}{\sqrt{2}}. \tag{2.44}$$

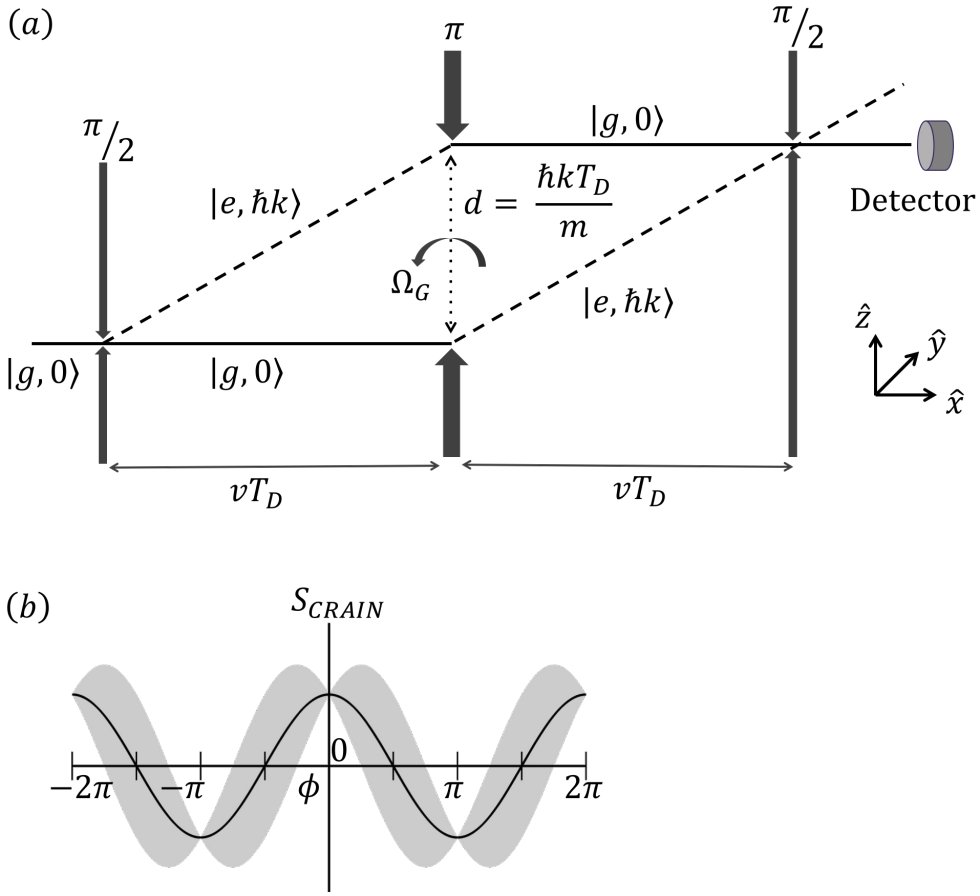

Figure 2.4. (a) A CRAIN produced via $\pi/2-$dark$-\pi-$dark$-\pi/2$ sequence of excitation. (b) Signal of the CRAIN, depicted by solid black line depends on teh phase shift as $S_{CRAIN} = N\cos^2\phi/2$. The standard deviation of the signal, $\Delta S_{CRAIN} = \sqrt{S_{CRAIN}(1 - S_{CRAIN}}$ is shown by the gray area.

At this point, the first dark zone ensues, and continues for a duration T_D. During the dark zone, the component of each atom in state $|e_i\rangle$ drifts to $(x = vT_D, z = \hbar kT_D/m)$. The state $|g_i\rangle$ continues along the **x**-direction. The trajectories taken by $|g_i\rangle$ and $|e_i\rangle$, are labeled A and B respectively. The dark zone also imparts a phase to the atom, so that

at its conclusion the state of the atom is

$$
\begin{aligned}
|\psi(\tau+T_D)\rangle &= |\psi(\tau+T_D)\rangle_A + |\psi(\tau+T_D)\rangle_B\,,\\
|\psi(\tau+T_D)\rangle_A &= \frac{1}{\sqrt{2}}\,|g\rangle\,,\\
|\psi(\tau+T_D)\rangle_B &= \frac{-i\exp(i\Delta T_D)}{\sqrt{2}}\,|e\rangle\,.
\end{aligned}
\tag{2.45}
$$

At this point, a $\pi-$pulse is applied to the atoms. This pulse acts as a mirror, and affects the transition $|g\rangle \leftrightarrow |e\rangle$, so that the state of the atoms at $t = 3\tau + T_D$ is

$$
\begin{aligned}
|\psi(3\tau+T_D)\rangle &= |\psi(3\tau+T_D)\rangle_A + |\psi(3\tau+T_D)\rangle_B\,,\\
|\psi(3\tau+T_D)\rangle_A &= -\frac{i}{\sqrt{2}}\,|e\rangle\,,\\
|\psi(3\tau+T_D)\rangle_B &= -\frac{\exp(i\Delta T_D)}{\sqrt{2}}\,|g\rangle\,.
\end{aligned}
\tag{2.46}
$$

A second dark zone begins at the end of the $\pi-$pulse. During this, the component of the atom in trajectory A begins to drift diagonally, as shown in Fig. 2.4(a), due to the gain of momentum in **z**-direction. On the other hand, the component following path B starts moving along the **x**-direction because of loss of momentum in **z**-direction. At the end of the second dark-zone the two trajectories converge, and the state of the atom is

$$
\begin{aligned}
|\psi(3\tau+2T_D)\rangle &= |\psi(3\tau+2T_D)\rangle_A + |\psi(3\tau+2T_D)\rangle_B\,,\\
|\psi(3\tau+2T_D)\rangle_A &= -\frac{i\exp(i\Delta T_D)}{\sqrt{2}}\,|e\rangle\,,\\
|\psi(3\tau+2T_D)\rangle_B &= -\frac{\exp(i\Delta T_D)}{\sqrt{2}}\,|g\rangle\,.
\end{aligned}
\tag{2.47}
$$

Following this, a last $\pi/2-$pulse is applied, causing an interference between the two trajectories. If the entire interferometer system is rotating about the **y**-axis, a phase difference ϕ is introduced between the two paths A and B, as explained in Sec. 2.2. The state of the atom at the end of the $\pi/2-$dark$-\pi-$dark$-\pi/2$ sequence is, therefore,

$$
\begin{aligned}
|\psi(4\tau+2T_D)\rangle &= |\psi(4\tau+2T_D)\rangle_A + |\psi(4\tau+2T_D)\rangle_B\,, \\
|\psi(4\tau+2T_D)\rangle_A &= -\exp(i\Delta T_D)\frac{(\exp(-i\phi)\,|g\rangle + i\,|e\rangle)}{2}, \\
|\psi(4\tau+2T_D)\rangle_B &= -i\exp(i\Delta T_D)\frac{(-i\,|g\rangle + \exp(i\phi)\,|e\rangle)}{2}.
\end{aligned} \tag{2.48}
$$

The final fringe pattern is the result of the interference of the states from the two trajectories. This is observed by measuring the number of atoms in either of the two states. The signal as a measure of the number of atoms in $|g\rangle$ is, therefore,

$$
\begin{aligned}
S_{CRAIN} &= N\left|\frac{1+\exp(-i\phi)}{2}\right|^2 \\
&= N\cos^2\left(\frac{\phi}{2}\right).
\end{aligned} \tag{2.49}
$$

A CRAIN of this type can be realized by employing an atomic beam with a continuous flux, or by employing pulses of atoms pushed out periodically from a magneto-optical-trap (MOT). The behavior of the CRAIN is essentially the same in both modes if the number of atoms interrogated in a given time window is the same. However, as will be described in Chapter 4, the collective state atomic interferometer (COSAIN) must operate in the latter (pulsed) mode. Thus, for proper comparison, the rest of this document will assume that the CRAIN is operated in the pulsed mode.

In the next chapter, we will detail upon the nature of collective states of atomic ensembles, the study of which is indispensable to the understanding of the COSAIN [**30**]. In particular, we will describe the conditions under which the asymmetric collective states (ACS) are intercoupled with the symmetric collective states of an ensemble of non-interacting, identical atoms excited by a laser. Additionally, we will also consider the effect of treating the center of mass degree of freedom of the atoms quantum mechanically on the description of the collective states, illustrating that it is indeed possible to construct a generalized collective state, as needed for the COSAIN, when each atom is assumed to be in a localized wave packet.

CHAPTER 3

Effects of Non-idealities on Collective States

3.1. Introduction

The rotation sensitivity of an atom interferometric gyroscope (AIG) due to the phase difference ϕ between two paths arising from the Sagnac effect has been described in Sec 2.2. This phase difference is proportional to the area enclosed by the interferometer as well as the mass of each atom. Motivated by this mass dependence of the rotation sensitivity of an AIG, we proposed an interferometer that exploits the collective excitation of an ensemble of atoms [**30**]. The principle behind the COSAIN is discussed at length in Chapter 4. In this chapter, we present a description of collective states under generalized and non-ideal conditions, including a situation where the motion of the COM of each atom is treated quantum mechanically. Such a comprehensive model of the collective states is important for understanding the behavior of the COSAIN. The analysis presented in this chapter, including the case where the COM motion is quantized, is also likely to help advance the analysis and optimization of spin squeezing [**31**–**34**], under non-idealities that are unavoidable in any practical scheme.

Dicke showed that for a dilute ensemble of N atoms where the atoms do not interact, the ensemble evolves to a superposition of $N+1$ symmetric states (shown in Fig. 3.1) [**35**].

Some of the possible Dicke states are defined as follows

$$
\begin{aligned}
|E_0\rangle &= |g_1, g_2, ..., g_N\rangle\,, \\
|E_1\rangle &= \textstyle\sum_{i=1}^{N} |g_1, g_2, ..., e_i, ..., g_N\rangle \,/\sqrt{N}, \\
|E_2\rangle &= \textstyle\sum_{j,k(j\neq k)}^{\binom{N}{2}} |g_1, ..., e_j, ...e_k, ..., g_N\rangle \,/\sqrt{\binom{N}{2}}, \\
|E_{N-1}\rangle &= \textstyle\sum_{i=1}^{N} |e_1, e_2, ..., g_i, ..., e_N\rangle \,/\sqrt{N}, \\
|E_N\rangle &= |e_1, e_2, ..., e_N\rangle\,,
\end{aligned}
\tag{3.1}
$$

etc. where $\binom{N}{n} = N!/n!(N-n)!$.

As noted in Sec. 2.3, the CRAIN as well as the COSAIN makes use of counter-propagating Raman transitions. As such, the characteristic wave number is k, where $k = (k_1 + k_2)$, and k_1 and k_2 are the wave numbers of the two laser beams. The non-zero temperature of a MOT provides a spread in the velocity of the constituent atoms. Therefore, each atom in the ensemble experiences a Doppler shift leading to a spread in detuning, with a zero mean value. Due to the finite size of the ensemble, each atom may experience a slightly different Rabi frequency depending on the spatial variation in the intensity profile of the laser beam. These factors contribute to a complex picture of an ensemble in a practical experiment. Furthermore, a semiclassical treatment of a quantum mechanical problem is not adequate. The wavepacket nature of the atoms must also be taken into account by considering the COM momentum of the atomic states.

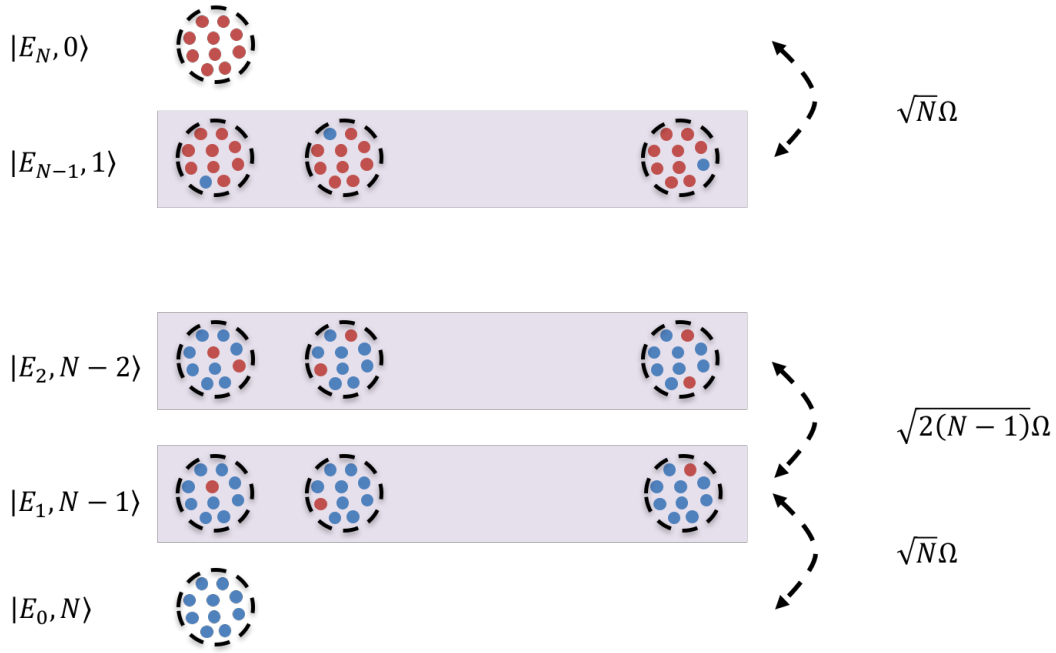

Figure 3.1. Schematic illustration of some of the possible symmetric collective states and coupling strength to their adjacent states. Blue represents the atoms being in $|g\rangle$, red represents the atoms in $|e\rangle$.

The rest of the chapter is organized as follows. Sec. 3.2 presents a description of the semiclassical model of generalized collective excitation to lay down the mathematical framework on which the present analysis is based. For the sake of simplicity and transparency, the concepts are first introduced with the example of a 2-atom ensemble identical to the Dicke formalism of collective excitation. Next, an analysis of how variable Rabi frequencies and atomic velocities affect this simple ensemble is presented. In Sec. 3.3, this investigation is extended to a general N-atom ensemble. In particular, it is shown that under certain conditions, the generalized asymmetric states of an ensemble are not decoupled from the symmetric set. The general method of finding the generalized

collective symmetric and asymmetric states in an ensemble of arbitrary size is developed. In Sec.3.4, the COM motion degree of freedom of the atoms is considered to investigate the implications of the wavepacket nature of the atoms, and therefore, of the ensemble. Finally, the equivalence between the phase shift induced due to Doppler shift, and that due to position change is presented in Sec. 3.5.

3.2. Semiclassical Model of Generalized Collective Excitation

Without loss of generality, consider a collection of N two level atoms, released from a cold trap, excited by a laser field traveling in the **z** direction, assuming the field amplitude to be of Gaussian profile in **x** and **y** directions, and constant in the **z** direction. Each atom is modeled as having two energy levels, $|g_i\rangle$ and $|e_i\rangle$. As mentioned in Sec. 2.1.2, a Λ-type atomic system excited by a pair of optically off-resonant laser fields propagating in opposite directions can be modeled as an effective two level system of this type [**17**], so that the decay rate of the $|e_i\rangle$ state can be set to zero. This effective two-level system is shown in Fig. 2.2(b). The laser field is assumed to be resonant for stationary atoms so that $\omega = \omega_0$. Each atom, however, experiences a different Doppler shift due to the thermal motion of the atoms, and consequently, a different effective laser frequency, ω_{0i}. The net consequence of this is that the i-th atom picks up a detuning of δ_i depending on its velocity. The Rabi frequency, Ω_i experienced by the i-th atom depends on its position.

The laser field is assumed, arbitrarily, to be polarized in the **x** direction. In the laboratory frame, the electric field at any point $\mathbf{r} = x\hat{\mathbf{x}} + y\hat{\mathbf{y}} + z\hat{\mathbf{z}}$, defined arbitrarily with

respect to an origin, can be expressed as

$$\mathbf{E_i}(\mathbf{r},t) = \hat{\mathbf{x}} E_0 \exp\left(-\frac{(x^2+y^2)}{2\sigma_L^2}\right)\cos(\omega_0 t - kz), \tag{3.2}$$

where σ_L represents the width of the laser beam in the transverse directions. At $t = 0$, the i-th atom is positioned at

$$\mathbf{r}_{0i} = x_{0i}\hat{\mathbf{x}} + y_{0i}\hat{\mathbf{y}} + z_{0i}\hat{\mathbf{z}}, \tag{3.3}$$

and is moving at a velocity

$$\mathbf{v}_i = v_{xi}\hat{\mathbf{x}} + v_{yi}\hat{\mathbf{y}} + v_{zi}\hat{\mathbf{z}}. \tag{3.4}$$

Any change to this velocity due to the interaction with the laser field is ignored for now. This issue will be addressed later when the motion of the COM of the atom is considered quantum mechanically. In the reference frame of this atom, which is defined by the vector $\mathbf{r}_i = \mathbf{r}_{0i} + \mathbf{v}_i t$, the electric field can be expressed as

$$\mathbf{E_i}(\mathbf{r_i},t) = \hat{\mathbf{x}} E_0 \exp\left(-\frac{(x_{0i}+v_{xi}t)^2 + (y_{0i}+v_{yi}t)^2}{2\sigma_L^2}\right)\cos\left(\omega_0 t - k(z_{0i}+v_{zi}t)\right). \tag{3.5}$$

The transverse motion of the atom will lead to a time dependent variation of the amplitude of the Rabi frequency. For typical systems of interest, $|v_{xi}t \ll \sigma_L|$ and $|v_{yi}t \ll \sigma_L|$, so that this variation can be ignored. The field seen by the atom in its reference frame as can then be written as

$$\mathbf{E_i}(\mathbf{r},t) = \hat{\mathbf{x}} E_0 \exp\left(-\frac{(x_{0i}^2+y_{0i}^2)}{2\sigma_L^2}\right)\cos(\omega_{0i} t - \xi_i), \tag{3.6}$$

where $\omega_{0i} = \omega_0 - kv_{zi}$ is the Doppler shifted frequency seen by the atom, and $\xi_i = kz_{0i}$ is a reference phase relation, determined by the initial position of the atom, between the atom and the field for all values of t.

In the electric dipole approximation, the Hamiltonian for the i-th atom can be written as $H_i = \mathbf{P}_i{}^2/2m + H_{0i} + q\rho_\mathbf{i}.\mathbf{E_i}$, where $\mathbf{P}_i$ is the COM momentum in the z-direction, H_{0i} is the internal energy of the atom, ρ_i is the position of the electron with respect to the nucleus, q is the electronic charge, and m is the mass of the atom. As mentioned above, we are treating the motion of the COM of the atom semiclassically, deferring the quantum mechanical model thereof to Sec. 3.4. As such, the COM term in the Hamiltonian can be ignored. Upon making the RWA, and Q-transformation (Eq. 2.16, setting $a_{i1} = \omega_g$ and $a_{i2} = \omega_{0i} + \omega_g$and, $b_{i1} = 0$, $b_{i2} = -\xi_i$), the Hamiltonian in the basis $|g_i'\rangle = \exp(-i\omega_g t)\,|g_i\rangle$ and $|e_i'\rangle = \exp(-i((\omega_e + \delta_i)t - \xi_i))\,|e_i\rangle$ is

$$H_i'/\hbar = -\delta_i\,|e_i'\rangle\,\langle e_i'| + \Omega_i(|g_i'\rangle\,\langle e_i'| + h.c.)/2. \tag{3.7}$$

Assuming that the i-th atom is initially in the state $c_{gi}(0)\,|g_i'\rangle + c_{ei}(0)\,|e_i'\rangle$, its quantum state can be written as

$$\begin{aligned} |\psi_i'\rangle =& e^{i\delta_i t/2}((c_{gi}(0)\cos\left(\frac{\Omega_i' t}{2}\right) - i\frac{c_{gi}(0)\delta_i + c_{ei}(0)\Omega_i}{\Omega_i'}\sin\left(\frac{\Omega_i' t}{2}\right))\,|g_i'\rangle \\ &+ (-i\frac{c_{gi}(0)\Omega_i - c_{ei}(0)\delta_i}{\Omega_i'}\sin\left(\frac{\Omega_i' t}{2}\right) + c_{ei}(0)\cos\left(\frac{\Omega_i' t}{2}\right))\,|e_i'\rangle), \end{aligned} \tag{3.8}$$

where $\Omega_i' = \sqrt{\Omega_i^2 + \delta_i^2}$ is the effective coupling frequency of this atom.

Since the atoms are assumed to be non-interacting, the ensemble Hamiltonian is the sum of all the individual Hamiltonians corresponding to each atom in the ensemble, $H_C' =$

$\Sigma_i H'_i$. The state of the ensemble, therefore, evolves according to the Schrödinger equation, $i\hbar\partial \left|\Psi'_C\right\rangle / \partial t = H'_C \left|\Psi'_C\right\rangle$. For illustrative purposes, as well as transparency, consider first the case of $N = 2$. H'_C can be expressed as

$$H'_1 \otimes I'_2 + I'_1 \otimes H'_2, \tag{3.9}$$

where I'_i is the identity operator in the basis of $|g'_i\rangle$ and $|e'_i\rangle$ for the i-th atom. For instance,

$$\begin{aligned} \left\langle g'_1 g'_2\right| H'_C \left|g'_1 e'_2\right\rangle &= \left\langle g'_1\right| H'_1 \left|g'_1\right\rangle \left\langle g'_2\right| I'_2 \left|e'_2\right\rangle + \left\langle g'_1\right| I'_1 \left|g'_1\right\rangle \left\langle g'_2\right| H'_2 \left|e'_2\right\rangle \\ &= \left\langle g'_2\right| H'_2 \left|e'_2\right\rangle \\ &= \hbar \frac{\Omega_2}{2}. \end{aligned} \tag{3.10}$$

Using this process, we can now express H'_C in the basis of product states of the two atoms, $|g'_1 g'_2\rangle$, $|e'_1 g'_2\rangle$, $|g'_1 e'_2\rangle$ and $|e'_1 e'_2\rangle$ as

$$\begin{aligned} H'_C/\hbar = &- \delta_1 \left|e'_1 g'_2\right\rangle \left\langle e'_1 g'_2\right| - \delta_2 \left|g'_1 e'_2\right\rangle \left\langle g'_1 e'_2\right| - (\delta_1 + \delta_2) \left|e'_1 e'_2\right\rangle \left\langle e'_1 e'_2\right| \\ &+ \Omega_1 (\left|g'_1 g'_2\right\rangle \left\langle e'_1 g'_2\right| + \left|e'_1 e'_2\right\rangle \left\langle g'_1 e'_2\right| + h.c.)/2 + \Omega_2 (\left|g'_1 g'_2\right\rangle \left\langle g'_1 e'_2\right| \\ &+ \left|e'_1 e'_2\right\rangle \left\langle e'_1 g'_2\right| + h.c.)/2. \end{aligned} \tag{3.11}$$

Consider first the case where all the Rabi frequencies are the same, and there are no detunings. The Q-transformed Hamiltonian for each atom is then formally identical, since the phase factors due to different positions are encoded in the transformed basis states $|g'_i\rangle$ and $|e'_i\rangle$. Thus, the coupled collective states would now be formally identical to the

symmetric Dicke states. For example,

$$
\begin{aligned}
|E_0'\rangle &= |g_1'\rangle\,|g_2'\rangle\,, \\
|E_1'\rangle &= (|g_1'e_2'\rangle + |e_1'g_2'\rangle)/\sqrt{2}, \\
|E_2'\rangle &= |e_1'\rangle\,|e_2'\rangle\,.
\end{aligned}
\tag{3.12}
$$

It should be noted that each of the constituent individual atomic states in these expressions include the temporal and spatial phase factors. Thus, these states behave the same way as the conventional Dicke symmetric collective states, independent of the distance between the two atoms. It should also be noted that there exists another collective state, $|E_{1,1}'\rangle \equiv (|g_1'e_2'\rangle - |e_1'g_2'\rangle)/\sqrt{2}$ which remains fully uncoupled from the symmetric set. The states $|E_1'\rangle$ and $|E_{1,1}'\rangle$ result from a $\pi/4$ rotation in the Hilbert subspace spanned by $|e_1'g_2'\rangle$ and $|g_1'e_2'\rangle$, as illustrated in Fig. 3.2(a).

Consider next the case where there is still no detuning, but the Rabi frequencies are unequal. It is not obvious what the form of the symmetric collective states should be in this case. Consider first the task of finding the first excited symmetric collective state (SCS). Since the $|E_0'\rangle$ state will, by definition, be coupled only to this state, we can define this state, in general, as

$$
|E_1'\rangle = \frac{H_C'\,|E_0'\rangle}{\sqrt{\langle E_0'|H_C'^{\dagger}H_C'|E_0'\rangle}},
\tag{3.13}
$$

where the denominator ensures that this state is normalized. When applied to the particular case at hand, we thus get

$$|E_1'\rangle = \frac{(\Omega_1 |e_1' g_2'\rangle + \Omega_2 |g_1' e_2'\rangle)}{\sqrt{\Omega_1^2 + \Omega_2^2}}. \tag{3.14}$$

A rotation operator, R, rotates the Hilbert sub-space, $\Phi_{2,1}$, formed by $|e_1' g_2'\rangle$ and $|g_1' e_2'\rangle$ by an angle $\theta = \tan^{-1}(\Omega_1/\Omega_2)$, such that one of the resulting states is $|E_1'\rangle$. This also produces a state

$$|E_{1,1}'\rangle = \frac{(\Omega_2 |e_1' g_2'\rangle - \Omega_1 |g_1' e_2'\rangle)}{\sqrt{\Omega_1^2 + \Omega_2^2}}, \tag{3.15}$$

which is orthogonal to $|E_1'\rangle$. In this rotated frame, the ensemble Hamiltonian, $\tilde{H_C'} = RH_C'R^{-1}$ becomes

$$\begin{aligned} \tilde{H_C'}/\hbar =& \sqrt{\Omega_1^2 + \Omega_2^2} |E_0'\rangle \langle E_1'| /2 + \Omega_1 \Omega_2 |E_1'\rangle \langle E_2'| /\sqrt{\Omega_1^2 + \Omega_2^2} \\ &+ (\Omega_2^2 - \Omega_1^2) |E_{1,1}'\rangle \langle E_2'| /2\sqrt{\Omega_1^2 + \Omega_2^2} + h.c. \end{aligned} \tag{3.16}$$

Thus, the asymmetric collective state (ACS), $|E_{1,1}'\rangle$ does not remain isolated but is coupled to $|E_2'\rangle$, which, in turn is coupled to $|E_1'\rangle$. Consider next the case where we also allow for potentially different detunings for the two atoms, δ_1 and δ_2. It is easy to see, based on the general definition in Eq. (3.13) of the first excited SCS, that $|E_1'\rangle$ has the same form as in Eq. (3.13). Similarly, the expression for $|E_{1,1}'\rangle$ is also the same as above, and these states are generated by the same rotation operator, R, as given above. However, the coupling between the states in this rotated basis are now modified. Explicitly the

ensemble Q-transformed Hamiltonian in the rotated frame becomes

$$\begin{aligned}\tilde{H}'_C/\hbar = &-(\delta_1\Omega_1^2+\delta_2\Omega_2^2)(|E'_1\rangle\langle E'_1|+|E'_{1,1}\rangle\langle E'_{1,1}|)/(\Omega_1^2+\Omega_2^2)\\ &-(\delta_1+\delta_2)|E'_2\rangle\langle E'_2|+\sqrt{\Omega_1^2+\Omega_2^2}\,|E'_0\rangle\langle E'_1|/2\\ &+\Omega_1\Omega_2|E'_1\rangle\langle E'_2|/\sqrt{\Omega_1^2+\Omega_2^2}+(\Omega_2^2-\Omega_1^2)|E'_{1,1}\rangle\langle E'_2|/2\sqrt{\Omega_1^2+\Omega_2^2}\\ &-(\delta_1-\delta_2)\Omega_1\Omega_2|E'_1\rangle\langle E'_{1,1}|/(\Omega_1^2+\Omega_2^2)+h.c.\end{aligned} \tag{3.17}$$

Thus, the ACS $|E'_{1,1}\rangle$ is now coupled directly to the SCS $|E'_1\rangle$, in addition to being coupled to the state $|E'_2\rangle$. Furthermore, the energies of the states are also shifted with respect to $|E'_0\rangle$. These couplings and shifts are illustrated in Fig. 3.2(b).

In an ensemble with a large number of atoms, the number of asymmetric states is far larger than that of the symmetric states. A more generalized view of collective states, considering the variations in different parameters and manifestations thereof in the behavior of the collective states is discussed in the next section.

The preceding discussions take into account the facts that each atom is at a unique position (which means that it sees a unique phase of the laser), sees a potentially unique Rabi frequency, and is moving with a particular velocity which in turn produces a Doppler shift. A natural question that may arise is whether the change in position of the atom with time is accounted for, so that it would see a time varying Rabi frequency and laser phase. The temporal variation in Rabi frequency can be ignored because the velocity of each atom is assumed to be very small. In Sec. 3.5, it is shown that the temporal change in the laser phase seen by the atom is akin to taking into account the Doppler shift.

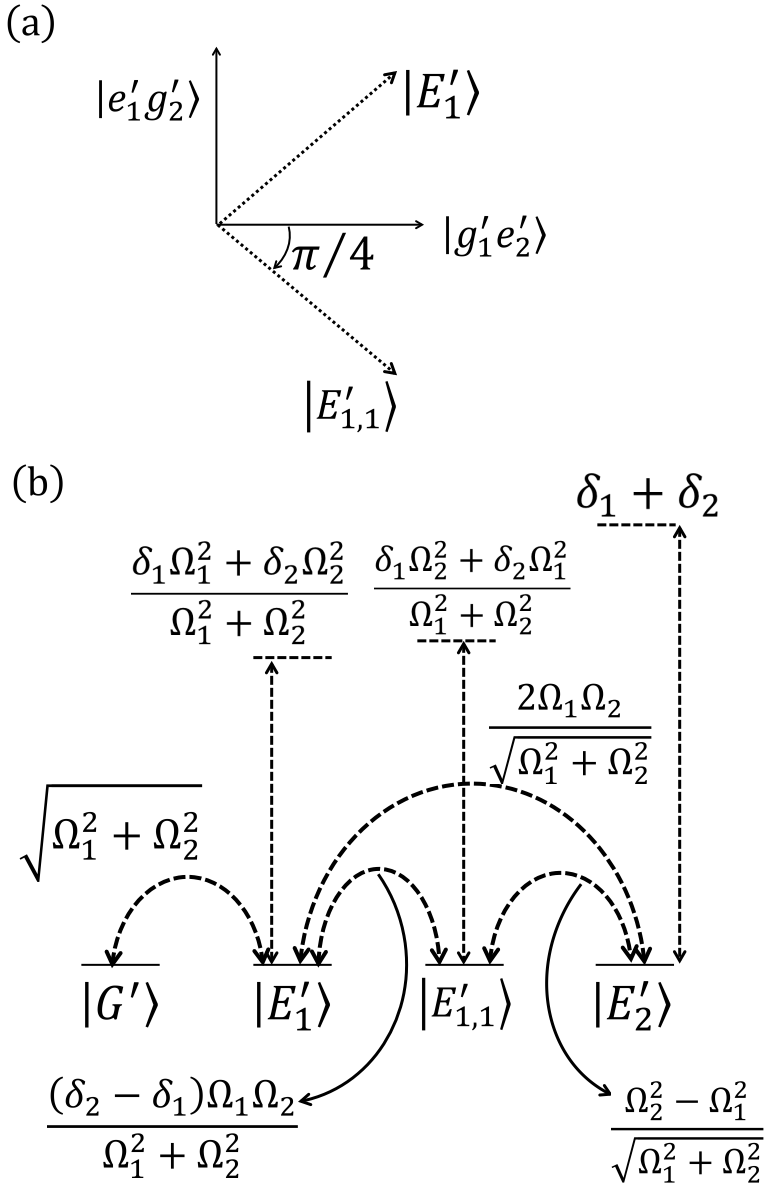

Figure 3.2. (a) Rotation of basis states to form collective states in a two-atom ensemble, (b) the complete set of all collective states and relevant couplings and detunings in a two-atom ensemble. Here $|G'\rangle \equiv |E_0'\rangle$

3.3. N-Atom Ensemble

The Hamiltonian of an ensemble of N non-interacting and non-overlapping atoms is simply given by the sum of the Hamiltonians of the constituent atoms as noted above. It is convenient to express these as a sum of three parts: raising, lowering and detuning:

$$\begin{aligned} H'_C &= H'_r + H'_l + H'_d, \\ H'_r &= \sum_i^N \frac{\hbar\Omega_i}{2} \left|e'_i\right\rangle \left\langle g'_i\right|, \\ H'_l &= \sum_i^N \frac{\hbar\Omega_i}{2} \left|g'_i\right\rangle \left\langle e'_i\right|, \\ H'_d &= -\sum_i^N \hbar\delta_i \left|e'_i\right\rangle \left\langle e'_i\right|. \end{aligned} \tag{3.18}$$

The raising part of the Hamiltonian, H'_r couples $|E'_n\rangle$ to its adjacent higher SCS, $|E'_{n+1}\rangle$. Similarly, the lowering part of the Hamiltonian, H'_l couples $|E'_n\rangle$ to its adjacent lower SCS, $|E'_{n-1}\rangle$. The function of the third term, H'_d is two fold. First, it leads to a shift in the energy of the collective states (symmetric and asymmetric). Second, under certain conditions, it leads to a coupling between the SCS and all the ACS's, as well as among all the ACS's, within the same manifold (i.e., the set of collective states corresponding to the absorption of a given number of photons). Analogous to Eq. (3.13), $|E'_{n+1}\rangle$ can be generated from $|E'_n\rangle$, for any value of n, using the following prescription

$$|E'_{n+1}\rangle = \frac{H'_r \left|E'_n\right\rangle}{\sqrt{\langle E'_n|H'^{\dagger}_r H'_r|E'_n\rangle}}. \tag{3.19}$$

To illustrate the use of Eq. (3.19), consider first the ideal case where each atom sees the same Rabi frequency, and experiences no Doppler shift, while still allowing for the

fact that different atoms see different spatial phases. Since $H'_d = 0$, the asymmetric states remain fully uncoupled from the symmetric states. Using Eq. (3.19), $|E'_1\rangle$ can be easily found. Application of H'_r to $|E'_0\rangle$, upon normalization, then leads to the result that $|E'_1\rangle = \sum_{k=1}^{N} |g'_1 g'_2, ...e'_k, ..., g'_N\rangle / \sqrt{N}$. This is essentially the same as the well-known first-excitation Dicke state, with the exception that the spatial phases seen by the individual atoms are incorporated in the constituent states $|g'\rangle$ and $|e'\rangle$, as noted before in the context of $N = 2$.

It is now easy to see how to generate $|E'_n\rangle$ for any value of n, by repeated application of H'_r, and allowing for the normalization, as prescribed by Eq. (3.19). Specifically,

$$|E'_n\rangle = J(N,n)^{-1/2} \sum_{k=1}^{J(N,n)} P_k \, |g'^{\otimes(N-n)} e'^{\otimes n}\rangle \,, \tag{3.20}$$

where $J(N,n) \equiv J = \binom{N}{n}$, and P_k is the permutation operator [**36**].

Under the ideal condition being considered here, the ACS's remain fully decoupled from the symmetric set at all times, as noted above. As such, an explicit description of the forms of the ACS's is not necessary for understanding the behavior of the ensemble. However, the understanding of the form of the ACS's is important when considering the non-idealities. Therefore, in what follows, the method for determining these states explicitly in the ideal case is presented. A simple modification of this is used later on for the non-ideal cases, where the ACS's are relevant.

Consider a particular manifold corresponding to the absorption of n photons. The SCS is $|E'_n\rangle$, and there are $(J-1)$ ACS's, denoted as $|E'_{n,j}\rangle$ for $j = 1$ to $(J-1)$. To find these states, we consider $\Phi_{N,n}$, the Hilbert sub-space of dimension J spanned by the states $P_k \, |g'^{\otimes(N-n)} e'^{\otimes n}\rangle$. The elements of $\Phi_{N,n}$ are arbitrarily labeled $\hat{s}_1, \hat{s}_2, \ldots, \hat{s}_J$. The

SCS is a particular vector in this Hilbert space, and the ACS's are any set of mutually orthogonal vectors that are all normal to the SCS. Thus, the set of ACS's is not unique, and there are many ways to construct them. The standard procedure for finding such a set of orthonormal vectors is the Gram-Schmidt Orthogonalization (GSO) process. From a geometric point of view, the GSO process can be seen as a set of generalized rotations (with potentially complex angles) in the Hilbert space. Given that the SCS consists of a superposition of the basis vectors with real coefficients, these rotations can be viewed in terms of physical angles for $N = 2$ and 3, whereas for $N > 3$, the angles have to be interpreted in an abstract manner. In order to elucidate an understanding of the ACS's, the construction of ACS's for arbitrary N and n, by successive rotations of the Hilbert subspace, $\Phi_{N,n}$ is formulated first. Next, this model is applied to $N = 3$ for constructing some explicit version of the ACS's (noting that the $N = 2$ case has only a single ACS which can be found trivially and has been explained in detail in Sec. 3.2).

The elements of $\Phi_{N,n}$, labeled $\hat{s}_1, \hat{s}_2, \ldots, \hat{s}_J$, form the coordinate axes of this Hilbert space. In this picture, the SCS can be represented as $\mathbf{V} = (\hat{s}_1 + \hat{s}_2 + \ldots + \hat{s}_J)/\sqrt{J}$, a vector that makes an angle, $\theta = \cos^{-1}(1/\sqrt{J})$ with each of the axes. Thus, the process to find all the collective states of $\Phi_{N,n}$, including the SCS and all the ACS's, is as follows. Starting with the original set of coordinate axes: $\hat{s}_1, \hat{s}_2, \ldots, \hat{s}_J$, a set of $(J-1)$ rotations are carried out, producing a new set of coordinate axes that are mutually orthogonal. The rotation angles are chosen to ensure that after the $(J-1)$ rotations, one of the coordinate axes is parallel to $\mathbf{V}$ (which is the SCS), so that the remaining set of coordinate axes can be identified as the ACS's. This is accomplished by carrying out the following steps:

Step 1: $\mathbf{V}$ is written as a sum of two terms, $\mathbf{V}_{12}$ and $\mathbf{V}_{rest}$, where $\mathbf{V}_{12} = (\hat{s}_1+\hat{s}_2)/\sqrt{J}$. Normalization of $\mathbf{V}_{12}$ gives the unit vector $\hat{\mathbf{V}}_{12} = (\hat{s}_1 + \hat{s}_2)/\sqrt{2}$, revealing that it makes an angle $\cos^{-1}(1/\sqrt{2})$ with $\hat{s}_1$ and $\hat{s}_2$. Therefore, the plane of $\hat{s}_1$ and $\hat{s}_2$ must be rotated around the origin by $\theta_2 = (-\cos^{-1}(1/\sqrt{2}))$ to give $\hat{s}'_1 = (\hat{s}_1-\hat{s}_2)/\sqrt{2}$ and $\hat{s}'_2 = (\hat{s}_1+\hat{s}_2)/\sqrt{2}$. Obviously, $\hat{s}'_2$ is parallel to $\mathbf{V}_{12}$. By construction, $\hat{s}'_1$ is orthogonal to $\hat{s}'_2$, and therefore to $\mathbf{V}_{12}$. Since $\mathbf{V}_{rest}$ does not contain any component in the $\{\hat{s}_1, \hat{s}_2\}$ plane, it then follows that $\hat{s}'_1$ is orthogonal to $\mathbf{V}$, and is therefore an ACS. For $N = 2$ described in Sec. 3.2, $\hat{s}'_1 = |E'_{1,1}\rangle$ and $\hat{s}'_2 = |E'_1\rangle$, and the process stops at this point.

Step 2: The vector, $\mathbf{V}$ is rewritten as another sum of two terms, $\mathbf{V}_{123}$ and $\mathbf{V}'_{rest}$, where $\mathbf{V}_{123} = (\hat{s}_1 + \hat{s}_2 + \hat{s}_3)/\sqrt{J}$. Normalization of $\mathbf{V}_{123}$ gives the unit vector $\hat{\mathbf{V}}_{123} = (\hat{s}_1 + \hat{s}_2 + \hat{s}_3)/\sqrt{3}$, showing that it makes an angle $\cos^{-1}(1/\sqrt{3})$ with $\hat{s}_1$, $\hat{s}_2$ and $\hat{s}_3$. Since $\hat{s}'_1$ is orthogonal to $\mathbf{V}$, we leave it undisturbed. The plane of $\hat{s}'_2$ and $\hat{s}_3$ is rotated around the origin by $\theta_3 = (-\cos^{-1}(1/\sqrt{3}))$, resulting in $\hat{s}''_2 = (\hat{s}_1 + \hat{s}_2 - 2\hat{s}_3)/\sqrt{6}$ and $\hat{s'}_3 = (\hat{s}_1 + \hat{s}_2 + \hat{s}_3)/\sqrt{3}$. It is clear that $\hat{s}'_3$ is parallel to $\mathbf{V}_{123}$. By construction, $\hat{s}''_2$ is orthogonal to $\hat{s}'_3$, and therefore, to $\mathbf{V}_{123}$. Furthermore, since $\mathbf{V}'_{rest}$ does not contain any component in the $\{\hat{s}_1, \hat{s}_2, \hat{s}_3\}$ plane, it then follows that $\hat{s}''_2$ is orthogonal to $\mathbf{V}$. $\hat{s}''_2$ is also orthogonal to $\hat{s}'_1$, since it is a linear combination of $\hat{s}'_2$ and $\hat{s}'_3$, which are both orthogonal to $\hat{s}'_1$. Thus, $\hat{s}''_2$ is the second ACS. For $N = 3$ and $n = 2$, this is the terminal step, resulting in $\hat{s}'_1 = |E'_{2,1}\rangle$, $\hat{s}''_2 = |E'_{2,2}\rangle$ and $\hat{s}'_3 = |E'_2\rangle$, as shown in Fig. 3.3.

Step 3: $\mathbf{V}$ is written again as $\mathbf{V} = \mathbf{V}_{1234}+\mathbf{V}''_{rest}$, where $\mathbf{V}_{1234} = (\hat{s}_1+\hat{s}_2+\hat{s}_3+\hat{s}_4)/\sqrt{J}$. Again, normalizing $\mathbf{V}_{1234}$ gives $\hat{\mathbf{V}}_{1234} = (\hat{s}_1 + \hat{s}_2 + \hat{s}_3 + \hat{s}_4)/\sqrt{4}$, showing that it makes an angle $\cos^{-1}(1/\sqrt{4})$ with $\hat{s}_1$, $\hat{s}_2$, $\hat{s}_3$ and $\hat{s}_4$. As described in Step 2 above, $\hat{s}'_1$ and $\hat{s}''_2$ are orthogonal to each other and to $\mathbf{V}$, and, therefore, these two are left undisturbed. To

find the vector orthogonal to this pair as well as to $\mathbf{V}$, the plane of $\hat{s}'_3$ and $\hat{s}_4$ is rotated about the origin by $\theta_4 = (-\cos^{-1}(1/\sqrt{4}))$, and derive $\hat{s}''_3 = (\hat{s}_1 + \hat{s}_2 + \hat{s}_3 - 3\hat{s}_4)/\sqrt{12}$ and $\hat{s}'_4 = (\hat{s}_1 + \hat{s}_2 + \hat{s}_3 + \hat{s}_4)/\sqrt{4}$. Following the same set of arguments presented in Step 2, it is easy to show that $\hat{s}''_3$ is orthogonal to $\hat{s}'_1, \hat{s}''_2$ and $\mathbf{V}$. As such, this is the third ACS. For $N = 4$ and $n = 1$, this is the terminal step, resulting in $\hat{s}'_1 = |E'_{1,1}\rangle$, $\hat{s}''_2 = |E'_{1,2}\rangle$, $\hat{s}''_3 = |E'_{1,3}\rangle$ and $\hat{s}'_4 = |E'_1\rangle$.

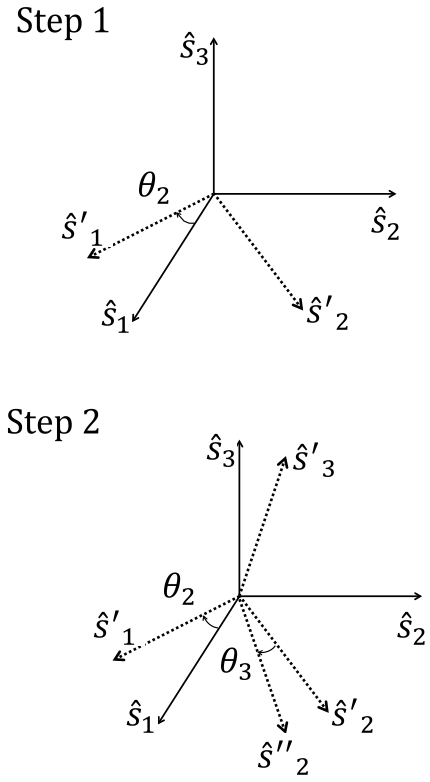

Figure 3.3. Hilbert sub-space rotation of the first excited state of an ensemble of three atoms.

For arbitrary N and n, there are $(J-1)$ such steps to arrive at the Hilbert sub-space $\Phi'_{N,n}$ spanned by $\hat{s}'_1, \hat{s}''_2, \hat{s}''_3, \ldots, \hat{s}'_J$, where $\hat{s}'_J$ is the SCS and the rest are the ACS's. This process can be formalized by the method of matrix rotations considering the column

vector formed by the elements of the space $\Phi_{N,n}$ as follows

$$\mathbf{S} = \begin{bmatrix} \hat{s}_1 & \hat{s}_2 \dots & \hat{s}_J \end{bmatrix}^T . \tag{3.21}$$

The vector, $\mathbf{S}$ undergoes a series of rotations that transforms it to another vector, $\mathbf{S}_C$ whose elements are the symmetric and asymmetric collective states for that particular manifold of the ensemble. The first rotation matrix, $R(2)$ causes a rotation of $\mathbf{S}$ in the $\{\hat{s}_1, \hat{s}_2\}$ plane to form $\mathbf{S}_2$ whose elements are $\{\hat{s'}_1, \hat{s'}_2, \hat{s}_3, \dots, \hat{s}_J\}$. The second rotation matrix, $R(3)$ further rotates the vector $\mathbf{S}_2$ in the $\{\hat{s'}_2, \hat{s}_3\}$ plane to give $\mathbf{S}_3$. This process is continued until the vector, $\mathbf{S}_J \equiv \mathbf{S}_C$ is formed by applying $R(J)$ on $\mathbf{S}_{J-1}$. Therefore, the overall process may be expressed as $\mathbf{S}_C = R_T \mathbf{S}$, where $R_T = R(J)R(J-1)\dots R(3)R(2)$. The j-th rotation vector is of the form

$$R(j)_{m,n} = \begin{cases} 1 \text{ for } m = n, m \neq j-1, j \\ \cos\theta_j \text{ for } m = n = j-1, j \\ -\sin\theta_j \text{ for } m = j, n = j-1 \\ \sin\theta_j \text{ for } m = j-1, n = j \\ 0 \text{ otherwise} \end{cases} , \tag{3.22}$$

where $\theta_j = \cos^{-1}(1/\sqrt{j})$, so that $\cos\theta_j = 1/\sqrt{j}$ and $\sin\theta_j = \sqrt{(j-1)/j}$. This matrix represents a simple rotation by an angle of $(-\theta_j)$ in the plane of $\hat{s}'_{j-1}$ and $\hat{s}_j$. To visualize

this, the explicit form of $R(2)$, $R(3)$ and $R(4)$ is shown below.

$$R(2) = \begin{bmatrix} \cos\theta_2 & -\sin\theta_2 & 0 & 0 & \dots & 0 \\ \sin\theta_2 & \cos\theta_2 & 0 & 0 & \dots & 0 \\ 0 & 0 & 1 & 0 & \dots & 0 \\ 0 & 0 & 0 & 1 & \dots & 0 \\ \vdots & \vdots & \vdots & \vdots & \ddots & \vdots \\ 0 & 0 & 0 & 0 & \dots & 1 \end{bmatrix},$$

$$\theta_2 = \cos^{-1}(1/\sqrt{2}) \tag{3.23a}$$

$$R(3) = \begin{bmatrix} 1 & 0 & 0 & 0 & \dots & 0 \\ 0 & \cos\theta_3 & -\sin\theta_3 & 0 & \dots & 0 \\ 0 & \sin\theta_3 & \cos\theta_3 & 0 & \dots & 0 \\ 0 & 0 & 0 & 1 & \dots & 0 \\ \vdots & \vdots & \vdots & \vdots & \ddots & \vdots \\ 0 & 0 & 0 & 0 & \dots & 1 \end{bmatrix},$$

$$\theta_3 = \cos^{-1}(1/\sqrt{3}) \tag{3.23b}$$

$$R(4) = \begin{bmatrix} 1 & 0 & 0 & 0 & \dots & 0 \\ 0 & 1 & 0 & 0 & \dots & 0 \\ 0 & 0 & \cos\theta_4 & -\sin\theta_4 & \dots & 0 \\ 0 & 0 & \sin\theta_4 & \cos\theta_4 & \dots & 0 \\ \vdots & \vdots & \vdots & \vdots & \ddots & \vdots \\ 0 & 0 & 0 & 0 & \dots & 1 \end{bmatrix},$$

$$\theta_4 = \cos^{-1}(1/\sqrt{4}). \tag{3.23c}$$

In general, for arbitrary N, n and therefore, J, the SCS and ACS's can be expressed as follows

$$\begin{aligned} |E'_n\rangle =& \sum_{l=1}^{J} \hat{s}_l/\sqrt{J}, \\ |E'_{n,j}\rangle =& (\sum_{l=1}^{j} \hat{s}_l - j\hat{s}_{j+1})/\sqrt{j(j+1)}, \end{aligned} \tag{3.24}$$

where $j = 1, 2, \dots, n-1$. Conversely, the original unrotated vectors can be written in terms of the rotated, collective states bases as follows

$$\begin{aligned} \hat{s}_1 =& |E'_n\rangle /\sqrt{J} + \sum_{j=1}^{J-1} |E'_{n,j}\rangle /\sqrt{j(j+1)}, \\ \hat{s}_j =& |E'_n\rangle /\sqrt{J} + \sum_{l=j}^{J-1} |E'_{n,l}\rangle /\sqrt{l(l+1)} - \sqrt{j-1}\, |E'_{n,j-1}\rangle /\sqrt{j}, \end{aligned} \tag{3.25}$$

where $j = 2, \dots, n-1$. This inversion is useful in illustrating the behavior of the collective states in more complex situations, an example of which will be presented shortly.

In order to get a clearer picture of how the spread in detuning affects the behavior of the ensemble, the simple case of a 3-atom ensemble interacting with a laser of uniform profile is considered next. Additionally, the i-th atom is assumed to experience a detuning of δ_i. The manifold corresponding to the absorption of 1 photon is spanned by the set $\Phi_{3,1}$, whose elements, given by $|e'_1g'_2g'_3\rangle, |g'_1e'_2g'_3\rangle$ and $|g'_1g'_2e'_3\rangle$, are now labeled as $\hat{s}_1, \hat{s}_2$ and $\hat{s}_3$, respectively. The SCS of this manifold, as defined in Eq. (3.24), is given by

$$|E'_1\rangle = (\hat{s}_1 + \hat{s}_2 + \hat{s}_3)/\sqrt{3} = (|e'_1g'_2g'_3\rangle + |g'_1e'_2g'_3\rangle + |g'_1g'_2e'_3\rangle)/\sqrt{3}. \tag{3.26}$$

One of the possible ways of forming the set of ACS's is

$$|E'_{1,1}\rangle = \frac{\hat{s}_1 - \hat{s}_2}{\sqrt{2}} = \frac{|e'_1g'_2g'_3\rangle - |g'_1e'_2g'_3\rangle}{\sqrt{2}}, \tag{3.27}$$

and

$$|E'_{1,2}\rangle = \frac{(\hat{s}_1 + \hat{s}_2 - 2\hat{s}_3)}{\sqrt{6}} = \frac{|e'_1g'_2g'_3\rangle + |g'_1e'_2g'_3\rangle - 2\,|g'_1g'_2e'_3\rangle}{\sqrt{6}}. \tag{3.28}$$

The action of the ensemble Hamiltonian, $H'_C = H'_r + H'_l + H'_d$ on $|E'_1\rangle$ shows how it experiences an energy shift, and couples with its adjacent states as follows:

$$H'_r\,|E'_1\rangle\,/\hbar = \Omega(|e'_1e'_2g'_3\rangle + |e'_1g'_2e'_3\rangle + |g'_1e'_2e'_3\rangle)/\sqrt{3}, \tag{3.29a}$$

$$H'_l\,|E'_1\rangle\,/\hbar = \sqrt{3}\Omega\,|g'_1g'_2g'_3\rangle\,/2, \tag{3.29b}$$

$$H'_d\,|E'_1\rangle\,/\hbar = (-\delta_1\,|e'_1g'_2g'_3\rangle - \delta_2\,|g'_1e'_2g'_3\rangle - \delta_3\,|g'_1g'_2e'_3\rangle)/\sqrt{3}. \tag{3.29c}$$

It can be seen from Eq. (3.24) that Eq. (3.29a) can be written as $H_r' \left|E_1'\right\rangle / \hbar = \Omega \left|E_2'\right\rangle$ and Eq. (3.29b) can be written as $H_l' \left|E_1'\right\rangle / \hbar = \sqrt{3}\Omega \left|E_0'\right\rangle / 2$. Furthermore, each term on the right hand side in Eq. (3.29c) can be written in terms of the relevant SCS and ACS's according to Eq. (3.25):

$$\begin{aligned} H_d' \left|E_1'\right\rangle / \hbar = & -\delta_1 \hat{s}_1 / \sqrt{3} - \delta_2 \hat{s}_2 / \sqrt{3} - \delta_3 \hat{s}_3 / \sqrt{3} \\ = & -\left(\delta_1 + \delta_2 + \delta_3\right) \left|E_1'\right\rangle / 3 - \left(\delta_1 - \delta_2\right) \left|E_{1,1}'\right\rangle / \sqrt{6} \\ & -\left(\delta_1 + \delta_2 - 2\delta_3\right) \left|E_{1,2}'\right\rangle / \sqrt{18}. \end{aligned} \tag{3.30}$$

The first term in parentheses on the right hand side of Eq. (3.30) is the energy shift in $\left|E_1'\right\rangle$. The second and third terms give the coupling strength of $\left|E_1'\right\rangle$ with $\left|E_{1,1}'\right\rangle$ and $\left|E_{1,2}'\right\rangle$, respectively. In the case that each atom in the ensemble experiences the same detuning due to Doppler shift, these two terms go to zero, and the ACS's remain uncoupled from the symmetric set.

In the more complex case where each atom in the ensemble experiences a unique Rabi frequency, the raising part of the ensemble Hamiltonian applied to any SCS yields the next higher SCS of that ensemble, as prescribed in Eq. (3.19). To illustrate this, consider the example of a 4-atom ensemble where the raising part of the Hamiltonian is

$H'_r = \sum_{i=1}^{4} \hbar\Omega_i \left|e'_i\right\rangle \left\langle g'_i\right| /2$. The set of SCS's are therefore, the following:

$$
\begin{aligned}
\left|E'_1\right\rangle =&(\Omega_1 \left|e'_1 g'_2 g'_3 g'_4\right\rangle + \Omega_2 \left|g'_1 e'_2 g'_3 g'_4\right\rangle + \Omega_3 \left|g'_1 g'_2 e'_3 g'_4\right\rangle + \Omega_4 \left|g'_1 g'_2 g'_3 e'_4\right\rangle) \\
&\times (\Omega_1^2 + \Omega_2^2 + \Omega_3^2 + \Omega_4^2)^{-1/2} \\
\left|E'_2\right\rangle =&(\Omega_1\Omega_2 \left|e'_1 e'_2 g'_3 g'_4\right\rangle + \Omega_1\Omega_3 \left|e'_1 g'_2 e'_3 g'_4\right\rangle + \Omega_1\Omega_4 \left|e'_1 g'_2 g'_3 e'_4\right\rangle + \Omega_2\Omega_3 \left|g'_1 e'_2 e'_3 g'_4\right\rangle \\
&+ \Omega_2\Omega_4 \left|g'_1 e'_2 g'_3 e'_4\right\rangle + \Omega_3\Omega_4 \left|g'_1 g'_2 e'_3 e'_4\right\rangle)((\Omega_1\Omega_2)^2 + (\Omega_1\Omega_3)^2 + (\Omega_1\Omega_4)^2 \\
&+ (\Omega_2\Omega_3)^2 + (\Omega_2\Omega_4)^2 + (\Omega_3\Omega_4)^2)^{-1/2} \\
\left|E'_3\right\rangle =&(\Omega_1\Omega_2\Omega_3 \left|e'_1 e'_2 e'_3 g'_4\right\rangle + \Omega_1\Omega_2\Omega_4 \left|e'_1 e'_2 g'_3 2'_4\right\rangle + \Omega_1\Omega_3\Omega_4 \left|e'_1 g'_2 e'_3 e'_4\right\rangle \\
&+ \Omega_2\Omega_3\Omega_4 \left|g'_1 e'_2 e'_3 e'_4\right\rangle)((\Omega_1\Omega_2\Omega_3)^2 + (\Omega_1\Omega_2\Omega_4)^2 + (\Omega_1\Omega_3\Omega_4)^2 \\
&+ (\Omega_2\Omega_3\Omega_4)^2)^{-1/2}
\end{aligned}
$$

$$
\left|E'_4\right\rangle = \left|e'_1 e'_2 e'_3 e'_4\right\rangle . \tag{3.31}
$$

The set of ACS's corresponding to $\left|E'_n\right\rangle$ in the present case of non-uniform Rabi frequency consists of $(J-1)$ elements that are orthogonal to one another as well as to $\left|E'_n\right\rangle$. As mentioned above, they can be constructed using the GSO process. The realization of this process as a set of rotations follows a similar set of rules as described above. However, the rotation angles will now depend on the relative amplitudes of all the Rabi frequencies. The details of this process are beyond the scope of the present discussion and will be presented elsewhere.

3.4. Quantized COM Model of Ensemble

In a Conventional Raman Atomic Interferometer (CRAIN), one must take into account the quantum nature of the COM motion. Similarly, for a COSAIN, the COM motion of the atom must be considered quantum mechanically. In doing so, one must consider all the degrees of freedom of the COM. However, for a CRAIN as well as the COSAIN (which is a variant of the CRAIN), only the motion in the direction parallel to the laser beams (which we have chosen to be the **z** direction) has to be quantized. As such, in what follows, the discussion is kept confined to such a scenario.

The i-th atom is now a Gaussian wavepacket formed by the superposition of an infinite number of plane waves, where the p-th plane wave can exist in two energy states, $|g_{ip}, \hbar k'_{ip}\rangle$ and $|e_{ip}, \hbar(k'_{ip}+k)\rangle$, which differ by a momentum $\hbar k$. Since the laser field amplitude is assumed to be constant in the **z** direction, the Rabi frequency experienced by each plane wave manifold of the i-th atom is Ω_i. The Doppler shift induced due to the thermal motion of the atoms in the **z** direction ascribes a detuning of δ_{Ti} to this atom. As such, the Hamiltonian of the p-th plane wave of the i-th atom is

$$\begin{aligned} H_{ip}/\hbar =&(\omega_g + \hbar k'^2_{ip}/2m)\,|g_{ip}\rangle\,\langle g_{ip}| \\ &+ (\omega_e + \hbar(k'_{ip}+k)^2/2m)\,|e_{ip}\rangle\,\langle e_{ip}| \\ &+ \Omega_i(\exp\left(i(\omega_{0i}t - \xi_i)\right)|g_{ip}\rangle\,\langle e_{ip}| + h.c.)/2. \end{aligned} \tag{3.32}$$

The Schrödinger equation governing the evolution of the state vector of this plane wave, $|\psi_{ip}\rangle$, is $i\hbar\partial\,|\psi_{ip}\rangle\,/\partial t = H_{ip}\,|\psi_{ip}\rangle$. Similar to the description given in Sec 2.1.1, a

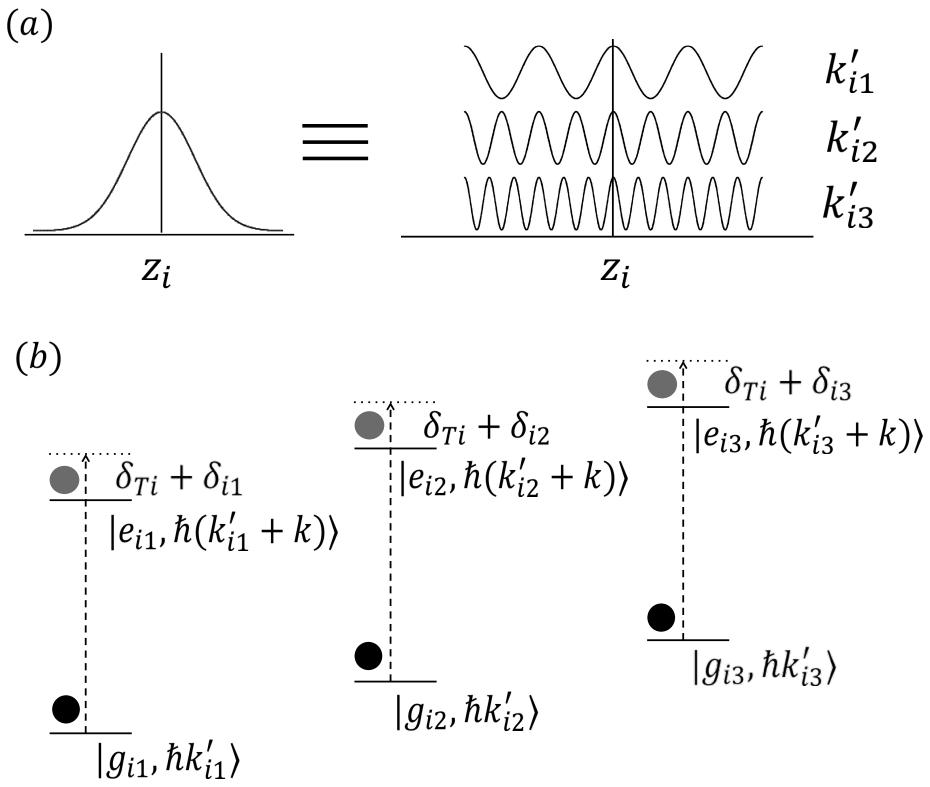

Figure 3.4. (a) Quantized COM model of an atom, (b) two level model of each plane wave component.

unitary transformation, Q_{ip} changes $|\psi_{ip}\rangle$ to $|\psi'_{ip}\rangle$ such that

$$Q_{ip} = \sum_{j=1}^{2} \exp\left(i(a_{ipj}t + b_{ipj})\right) |j\rangle \langle j| , \tag{3.33}$$

where a_{ipj} and b_{ipj} are arbitrary parameters. The Hamiltonian in the new basis vector thus formed is $H'_{ip} = Q_{ip}H_{ip}Q_{ip}^{-1} - \hbar\dot{Q}_{ip}Q_{ip}^{-1}$, so that $i\hbar\partial |\psi'_{ip}\rangle / \partial t = H'_{ip} |\psi'_{ip}\rangle$. It can be stripped of its time dependence by setting $a_{ip1} = \omega_g + \hbar k'^2_{ip}/2m$ and $a_{ip2} = \omega_e + \delta_{vi} + \hbar k'^2_{ip}/2m$. For $b_{ip1} = 0$ and $b_{ip2} = -\xi_i$, H'_{ip} is rendered independent of any phase factors. In the

transformed frame, the Hamiltonian is thus

$$H'_{ip}/\hbar = (-\delta_{vi} + \hbar k^2/2m + \hbar k k'_{ip}/m)\,|e'_{ip}\rangle\langle e'_{ip}| + \Omega_i(|g'_{ip}\rangle\langle e'_{ip}| + h.c.)/2. \tag{3.34}$$

Since the atom is a sum of these individual plane waves, it evolves according to the equation that is the sum of the individual Schrödinger equations, $i\hbar\partial(\sum_{p\to-\infty}^{\infty}|\psi'_{ip}\rangle)/\partial t = \sum_{p\to-\infty}^{\infty} H'_{ip}\,|\psi'_{ip}\rangle$. In the limit that the Rabi frequency of the i-th atom is large compared to the Doppler shift due to the COM momentum of each of the constituent plane waves, i.e. $\Omega_i \gg \hbar k k'_{ip}/m$, the corresponding Hamiltonians become identical to one another. The resulting evolution equation is then $i\hbar\partial\,|\psi'_i\rangle\,/\partial t = H'_i\,|\psi'_i\rangle$, where $|\psi'_i\rangle = \sum_{p\to-\infty}^{\infty}|\psi'_{ip}\rangle$ and $H'_i = H'_{i1} = H'_{i2}$, etc. In this regime, the atom's Hamiltonian becomes $H'_i/\hbar = -\delta_i\,|e'_i\rangle\langle e'_i| + \Omega_i(|g'_i\rangle\langle e'_i| + h.c.)/2$, where $\delta_i = \delta_{vi} - \hbar k^2/2m$. This is identical to the semiclassical Hamiltonian of the atom where the COM mass degree of freedom of the atom is not considered. Thus, it is concluded that, under approximations that are valid for the COSAIN, a semi-classical description of the COM motion of each atom is sufficient. As such, all the results derived above regarding the properties of collective state remain valid for the COSAIN.

3.5. Equivalence Between Doppler Effect Induced Phase Shift and Position Change Induced Phase Shift

Consider an ideal two level atom, excited by a laser field traveling in the **z** direction, assuming the field amplitude to be uniform in all directions. The atom is modeled as having two energy levels, $|g\rangle$ and $|e\rangle$. For the issue at hand, it is not necessary to consider the radiative decay of $|e\rangle$. As such, both of the states are assumed to be long-lived.

This two-level system is shown in Fig. 3.5(a), where ω_0 is the frequency of the laser field, assumed to be resonant for a stationary atom. The laser field is assumed to be polarized, arbitrarily, in the $\mathbf{x}$ direction. As illustrated in Fig. 3.5(b), the atom is initially ($t = 0$) positioned at $\mathbf{r_{0i}} = x_{0i}\hat{\mathbf{x}} + y_{0i}\hat{\mathbf{y}} + z_{0i}\hat{\mathbf{z}}$ and is moving in the $\mathbf{z}$ direction with a non-relativistic velocity v. The electric field at a time t, in the atom's frame of reference, is $\mathbf{E}(\mathbf{r}, t) = \hat{\mathbf{x}}E_0 \cos(\omega_0 t - kz)$, where $z = z_{0i} + vt$. In the semiclassical model employed here, the Hamiltonian of this atom can be written as $H = H_{0i} + q\rho \cdot \mathbf{E}$, where the terms have their usual meanings as given in Sec. 3.2. After making the RWA as prescribed in Sec. 3.2, H can be written in the bases of $|g\rangle$ and $|e\rangle$ as

$$H/\hbar = \omega_g |g\rangle \langle g| + \omega_e |e\rangle \langle e| + \Omega(\exp(i(\omega_0 t - k(z_{0i} + vt))) |g\rangle \langle e| + h.c.)/2, \tag{3.35}$$

where $\Omega \equiv \langle g| (\mathbf{x} \cdot \rho) |e\rangle E/\hbar = \langle e| (\mathbf{x} \cdot \rho) |g\rangle E/\hbar$.

The state of this atom, $|\psi\rangle$ evolves according to the Schrödinger equation, $i\hbar\partial |\psi\rangle /\partial t = H |\psi\rangle$. A unitary transformation, Q defined as $Q = \sum_{j=1}^{2} \exp(i(a_j t + b_j)) |j\rangle \langle j|$ changes $|\psi\rangle$ to $|\psi'\rangle = Q |\psi\rangle$, where a_j and b_j are arbitrary parameters. The Q-transformed Hamiltonian for this state vector is then $H' = QHQ^{-1} - \hbar\dot{Q}Q^{-1}$, so that $i\hbar\partial |\psi'\rangle /\partial t = H' |\psi'\rangle$. H' is stripped of its time dependence by setting $a_1 = \omega_g$ and $a_2 = \omega_0 + \omega_g = \omega_e - kv$. Now, setting $b_1 = 0$, $b_2 = -kz_{0i}$ makes H' independent of any phase factor as well. The Q-transformed Hamiltonian thus becomes

$$H'/\hbar = kv |e'\rangle \langle e'| + \Omega(|g'\rangle \langle e'| + h.c.)/2. \tag{3.36}$$

Therefore, the velocity of the atom induces a net detuning of $\delta = -kv$. The new basis vectors, $|g'\rangle$ and $|e'\rangle$, are related to the original basis vectors as $\exp(-i\omega_g t) |g\rangle$ and

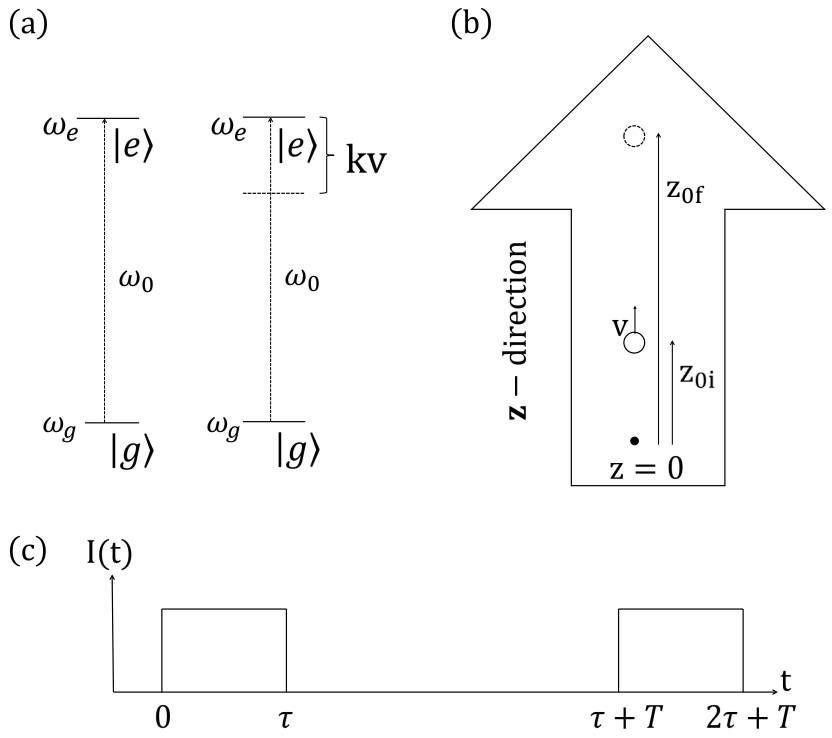

Figure 3.5. (a) (left) Two level atom in the lab frame frame, (right) in the atom's frame of reference, (b) change in the coordinates of the atom over the duration of interaction with the laser pulses, (c) laser beam intensity variation over the duration of interaction.

$\exp(-i((\omega_e - kv)t - kz_{0i}))\,|e\rangle$, respectively. If the atom is initially in $c_{gi}(0)\,|g_i'\rangle + c_{ei}(0)\,|e_i'\rangle$, its state after interaction for a time t is given by Eq. (4.10).

This atom interacts with two consecutive laser fields separated by a dark zone of duration T, as illustrated in Fig. 3.5(c). The time of interaction of the atom with each field is such that $\tau = \pi/2\Omega$. The atom initially at $z = z_{0i}$ drifts to $z = z_{0f}$ by the end of the entire interaction sequence. For the sake of simplicity, it is assumed that $kv \ll \Omega$ and that the atom's position does not change appreciably over the duration of the pulse. Starting with the atom in state $|g\rangle$ at $t = 0$, the state of the atom at the end of the first pulse ($t = \tau$) is $|\psi'\rangle = (|g'\rangle - i\,|e'\rangle)/\sqrt{(2)}$. The Q-transformed Hamiltonian in the dark

zone is given by $H'_d = kv\,|e'\rangle\,\langle e'|$. At $t = \tau + T$, the state of the atom can be expressed as

$$|\psi'\rangle = (|g'\rangle - i\exp(-ikvT)\,|e'\rangle)/\sqrt{2}. \tag{3.37}$$

After the atom's encounter with the second pulse ($t = 2\tau + T$), its quantum state can be written as $|\psi'\rangle = (1 - \exp(-ikvT))\,|g'\rangle\,/2 - i(1 + \exp(-ikvT))\,|e'\rangle\,/2$. In the original bases of $|g\rangle$ and $|e\rangle$, the final state of the atom at the end of the separated field interaction sequence is given by

$$\begin{aligned} |\psi\rangle =&(1 - \exp(-ikvT))\exp(-i\omega_g t)\,|g\rangle\,/2 - i(1 + \exp(-ikvT)) \\ &\times \exp(-i(\omega_e - kv)t + ikz_{0i})\,|e\rangle\,/2. \end{aligned} \tag{3.38}$$

Now, the same interaction shown in Fig. 3.5(c) is considered in the laboratory frame of reference in which the electric field at any point along the laser's direction of propagation (**z** direction) is given by $\mathbf{E}(\mathbf{r}, t) = \hat{\mathbf{x}}E_0\cos(\omega_0 t - kz)$. Considering that at $t = 0$ the atom is positioned at $z = z_{0i}$, the Hamiltonian for the first interaction zone is given by $H_{L1}/\hbar = \omega_g\,|g\rangle_{LL}\langle g| + \omega_e\,|e\rangle_{LL}\langle e| + \Omega(\exp(i(\omega_0 t - kz_{0i}))\,|g\rangle_{LL}\langle e| + h.c.)/2$, where the subscript L indicates that this is in the laboratory frame. The state of the atom evolves according to $i\hbar\partial\,|\psi\rangle_L\,/\partial t = H_{L1}\,|\psi\rangle_L$. Therefore, the transformation Q_1 to remove time and phase dependence from H_{L1} is given by $Q_1 = \exp(i\omega_g t)\,|1\rangle\,\langle 1| + \exp(i(\omega_e t - kz_{0i}))\,|2\rangle\,\langle 2|$. The resulting Q-transformed Hamiltonian in the bases of $|g'\rangle_L$ and $|e'\rangle_L$ is $H'_{L1}/\hbar = (\Omega\,|g'\rangle_{LL}\langle e'| + h.c.)/2$. As a result, considering that the atom is in state $|g'\rangle_L$ at $t = 0$, the state of the atom at $t = \tau$ is $|\psi'\rangle = (|g'\rangle_L - i\,|e'\rangle_L)/\sqrt{2}$.

The dark zone Q-transformed Hamiltonian, H'_{Ld} contains no non-zero elements. Thus, at the end of the dark zone ($t = \tau + T$), the quantum state of the atom remains unaltered. Since the atom has a non zero velocity, v along $\mathbf{z}$ direction, by the end of the dark zone it will have moved to $z = z_{0f}$. As a consequence, the Hamiltonian for the second pulse will be $H_{L2}/\hbar = \omega_g \left|g\right\rangle_{LL}\!\left\langle g\right| + \omega_e \left|e\right\rangle_{LL}\!\left\langle e\right| + \Omega(\exp(i(\omega_0 t - kz_{0f}))\left|g\right\rangle_{LL}\!\left\langle e\right| + h.c.)/2$. The Q-transformation required to make H_{L2} time and phase factor independent may be written as $Q_2 = \exp(i\omega_g t)\left|1\right\rangle\left\langle 1\right| + \exp(i(\omega_e t - kz_{0f}))\left|2\right\rangle\left\langle 2\right|$ so that $\left|\psi''\right\rangle_L = Q_2\left|\psi\right\rangle_L$. The new basis states thus formed are $\left|g''\right\rangle_L = \exp(i\omega_g t)\left|g\right\rangle_L$ and $\left|e''\right\rangle_L = \exp(i(\omega_e t - kz_{0f}))\left|e\right\rangle_L$. Therefore, the quantum state of the atom at the end of the dark zone ($t = \tau + T$), must now be written in the Q_2-transformed bases of $\left|g''\right\rangle_L$ and $\left|e''\right\rangle_L$. Therefore, $\left|\psi''\right\rangle_L = Q_2 Q_1^{-1}\left|\psi'\right\rangle_L = (\left|g''\right\rangle_L - i\exp(ik(z_{0i} - z_{0f}))\left|e''\right\rangle_L)/\sqrt{2}$. This is the initial condition for the second pulse. At the end of the second pulse, $t = 2\tau + T$, the atom's quantum state is, therefore, given by $\left|\psi''\right\rangle_L = (1 - \exp(ik(z_{0i} - z_{0f})))\left|g''\right\rangle_L/2 - i(1 + \exp(ik(z_{0i} - z_{0f})))\left|e''\right\rangle_L/2$. Thus, in the original bases of $\left|g\right\rangle_L$ and $\left|e\right\rangle_L$, the state of the atom is

$$\begin{aligned}\left|\psi\right\rangle_L =& (1 - \exp(ik(z_{0i} - z_{0f})))\exp(-i\omega_g t)\left|g\right\rangle_L/2 \\ & - i(1 + \exp(ik(z_{0i} - z_{0f})))\exp(-i\omega_e t + ikz_{0f})\left|e\right\rangle_L/2.\end{aligned} \tag{3.39}$$

Since $z_{0f} = z_{0i} + vT$, Eq. (3.39) is identical to Eq. (3.38). Thus, when one takes into account the Doppler shift, it is no longer necessary to consider explicitly the fact that the atom sees a different laser phase at different times.

3.6. Summary

In this chapter, we investigated the behavior of an ensemble of N non-interacting, identical atoms, excited by a laser with a wavelength of λ. In doing so, it was assumed that the wavefunctions of the atoms do not overlap with one another, so that quantum statistical properties are not relevant. In general, the i-th atom sees a Rabi frequency Ω_i, an initial position dependent laser phase ϕ_i, and a motion induced Doppler shift of δ_i. When $\Omega_i = \Omega$ and $\delta_i = \delta$ for all atoms, the system evolves into a superposition of $(N+1)$ generalized symmetric collective states, independent of the values of ϕ_i. If $\phi_i = \phi$ for all atoms, these states simplify to the well known Dicke collective states. When Ω_i or δ_i is distinct for each atom, the system evolves into a superposition of symmetric as well as asymmetric collective states. For large values of N, the number of asymmetric states $(2^N - (N+1))$ is far larger than that of the symmetric states. For a COSAIN and a COSAC it is important to understand the behavior of all the collective states under various conditions. Here, we described how to formulate systematically the properties of all the collective states under various non-idealities, and used this formulation to understand the dynamics thereof. Specifically, for the case where $\Omega_i = \Omega$ and $\delta_i = \delta$ for all atoms, we showed how the amplitudes of each of the generalized collective states can be determined explicitly in a simple manner. For the case where Ω_i or δ_i is distinct for each atom, we have shown how the symmetric and asymmetric collective states can be treated on the same footing. Furthermore, we have shown that the collective states corresponding to the absorption of a given number of photons can be visualized as an abstract, multi-dimensional rotation in the Hilbert space spanned by the ordered product states of individual atoms. This technique enables one to construct the explicit expression for any asymmetric state of

interest. Such expressions in turn can be used to determine the evolution of such a state in the COSAIN or the COSAC. We have also considered the effect of treating the COM degree of freedom of the atoms quantum mechanically on the description of the collective states. This is particularly relevant for the COSAIN. In particular, we have shown that it is indeed possible to construct a generalized collective state when each atom is assumed to be in a localized wave packet.

CHAPTER 4

Collective State Atomic Interferometer

4.1. Introduction

A COSAIN is configured essentially the same way as the CRAIN, with two exceptions. First, it must make use of trapped atoms, released sequentially to the interferometer. Second, the detection process is designed to measure the probability of finding all the atoms in one of the collective states, such as $|E_0\rangle$. It is, therefore, essential to recapitulate the dynamics of the CRAIN here briefly. A detailed description of this is given in Sec. 2.3. The building block of a CRAIN is a three level atom, with two metastable states, $|g, p_z = 0\rangle \equiv |g, 0\rangle$ and $|e, p_z = \hbar(k_1 + k_2)\rangle \equiv |e, \hbar k\rangle$ and an excited state $|a, p_z = \hbar k_1\rangle \equiv |a, \hbar k_1\rangle$ coupled by two counter propagating beams, with a single photon detuning δ (Fig. 4.1(a)). One of the beams, with Rabi frequency Ω_1, couples $|g, 0\rangle$ to $|a, \hbar k_1\rangle$, while the other beam, with Rabi frequency Ω_2, couples $|a, \hbar k_1\rangle$ to $|e, \hbar k\rangle$. For $\delta \gg \Omega_1, \Omega_2$, the interaction can be described as an effective two level system excited by an effective traveling wave with a momentum $\hbar k = \hbar(k_1 + k_2)$, with a Rabi frequency $\Omega = \Omega_1\Omega_2/2\delta$ (Fig. 4.1(b)) [**17**]. We assume that $\delta \gg \Gamma$, where Γ is the decay rate of $|a\rangle$, so that the effect of Γ can be neglected. Under a sequence of $\pi/2 - \pi - \pi/2$ pulses (Fig. 4.1 (c)), the wavepacket first separates into two components, then gets redirected and finally recombined. If this interferometer is rotating at a rate Ω_G about an axis normal to the area, a time lag is introduced between the two paths. The phase difference, ϕ

is then the product of the time lag and the wave frequency. For the CRAIN, this is the Compton-frequency of the atom, $\Omega_C = mc^2/\hbar$, for non-relativistic velocities, where m is the rest mass of the atom. A detailed derivation of this effect is given in Sec. 2.2. The expression for ϕ (Eq. 2.41), in terms of Ω_C is

$$\phi = \frac{2\Theta\Omega_G\omega_C}{c^2}. \tag{4.1}$$

The signal of the CRAIN, which is a measure of the amplitude of $|g\rangle$ at the end varies as $\cos^2(\phi/2)$ [**2**, **23**].

The dependence of ϕ on ω_C has motivated matter wave interferometry with large molecules. To date, the largest molecule used has a mass of $\sim$ 10000 atomic-mass-unit [**37**], corresponding to the mass of $\sim$ 75 ^{133}Cs atoms. These interferometers, based on the Talbot effect, are not suited for rotation sensing. Furthermore, for interferometry with much larger particles it would be necessary to use gratings with spacings too small to be realized with existing technologies. Additionally, effects such as van der Waals interaction would become dominant for such gratings. Inspired by these developments, we proposed an experiment that would reveal evidence of matter wave interference where a collection of N non-interacting, unentangled atoms acts as a *single* particle. For ^{87}Rb and $N = 10^6$, ω_C is $\sim$ ten nonillion Hz, and λ_{dB} is $\sim$ 4.5 femtometer at a velocity of 1 m/s. Furthermore, it can improve the phase measurement ability by a factor of as much as 10. This type of matter wave interferometry may also open up new opportunities for sensitive measurement of gravitational redshift [**15**] or matter wave clocks [**11**]. It may also serve as a testbed for macroscopic quantum decoherence due to gravitational redshift [**38**].

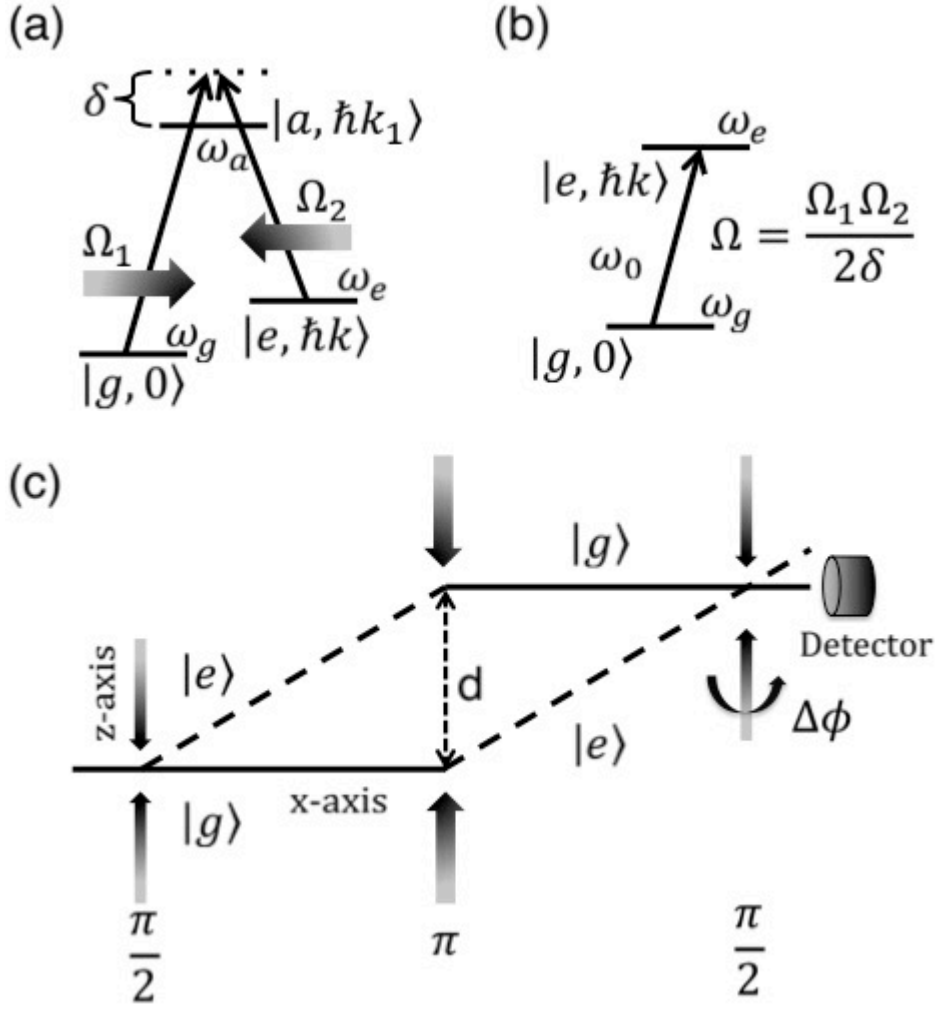

Figure 4.1. (a) A three level atom. (b) An equivalent reduced two-level atom model. (c) A CRAIN produced via $\pi/2 - \pi - \pi/2$ sequence of excitation.

Consider an assembly of N identical noninteracting atoms, subjected to the $\pi/2 - \pi - \pi/2$ sequence. If we imagine a situation where the ground state, $|E_0\rangle \equiv |g_1, g_2, \ldots, g_N\rangle$ is coupled, directly and only, to the state where all the atoms are in the excited state, $|E_N\rangle \equiv |e_1, e_2, \ldots, e_N\rangle$, the resulting ensemble interferometer would experience a phase-difference, $\phi_{EI} = N\phi$. However, existing technology does not enable such an excitation.

Even if one were to use a pure Fock state of $N' > N$ photons, the ensemble would evolve into a superposition of $(N+1)$ symmetric collective states $|E_n\rangle\,|N'-n\rangle$, where $|N'-n\rangle$ is a state of the field with $(N'-n)$ photons, and $|E_n\rangle = J(N,n)^{-1/2}\sum_{k=1}^{J(N,n)} P_k\,|g^{\otimes(N-n)}e^{\otimes n}\rangle$, where $J(N,n)\equiv\binom{N}{n}$,P_k is the permutation operator, and $n = 0, 1, 2, \ldots, N$ [**36**]. Since a laser is a superposition of many Fock states, the evolution of this system under laser excitation would produce a seemingly intractable superposition of these collective states. Modeling the laser field as a semi-classical one also does not simplify the picture much []. However, we show here that, by measuring the quantum state of a single collective state, it is possible to determine the effect of the interference among all the collective states, and describe how such a measurement can be done. Choosing this collective state to be one of the two extremal states (i.e., $|E_0\rangle$ or $|E_N\rangle$) also makes it possible to calculate this signal easily, since the state of the whole system can be described as the tensor product of individual atomic states. We show that the fringe width is reduced by a factor of $\sqrt{N}$, without using entanglement. For the current state of the art, the value of N can easily exceed 10^6, so that a reduction of fringe width by a factor of more than 10^3 is feasible. We also show that the phase fluctuation of the COSAIN can be significantly smaller, by as much as a factor of 10, than that for a conventional interferometer employing the same transition and the same atomic flux. The extremely narrow resonances produced in the COSAIN may also help advance the field of spin squeezing [**35**, **39**–**41**], which in turn is useful for approaching the Heisenberg limit in precision metrology. A collective state atomic clock, which employs the principle of collective excitation of atomic ensemble, and exhibits a similar narrowing in signal fringe [**42**].

In this chapter, we discuss the various aspects of the COSAIN. The rest of the chapter is arranged in the following way: in Sec. 4.2, we describe the theory of the working principle of a COSAIN. We also describe the physical phenomenon behind the narrowing of the signal fringes. Sec. 4.3 gives an account of the various parameter inhomogeneities that affect the signal amplitude and width. Sec. 4.4 details the description of the COSAIN experiment, also including a discussion of the role of the optical density of the ensemble. We also propose an alternate experimental scheme to achieve a higher value of effective optical density in Sec. 4.5. In Sec. 4.6, we analyze the performance of the COSAIN as compared to that of the CRAIN. We consider the effect of quantum and classical noise, detector efficiency, and collection efficiency.

4.2. Description of the COSAIN

Consider an ensemble of N noninteracting atoms of the kind described above [**35**], with the i-th atom in its ground state, $|g_i\rangle$. The ensemble is assumed to be initially situated at $(x = 0, z = 0)$ and traveling along the **x**-direction with a velocity v. The ensemble undergoes the same $\pi/2{-}\pi{-}\pi/2$ sequence as described for the CRAIN. Assuming resonant excitation, the Hamiltonian of the i-th atom after the rotating-wave transformation is $H_i = \Omega_i |g_i\rangle \langle e_i| /2 + c.c.$ [**39**], where Ω_i is the Rabi frequency of the i-th atom. Here, a phase transformation on the Hamiltonian has also been applied to render Ω_i real. For the sake of simplicity and brevity, we consider only the case where the intensity profile of the beams are rectangular, so that $\Omega_i = \Omega$. In a real experiment, the Rabi-frequency of each atom depends on its position relative to the Gaussian distribution of the beam intensity profile. Due to the non-zero temperature of the trapped atoms, they also experience

Doppler shift arising from thermal motion. A detailed description of the effect of these inhomogeneities on the COSAIN signal is presented in Sec. 4.3.

A $\pi/2$-pulse of duration τ is applied to the ensemble at $t = 0$, following which each atom is in state $|\psi_i(\tau)\rangle = (|g_i\rangle - i\,|e_i\rangle)/\sqrt{2}$. After the first dark-zone of duration of T_d, the component of the atom in state $|e_i\rangle$ drifts to $(x = vT_d, z = \hbar kT_d/m)$. The state $|g_i\rangle$ continues along the **x**-direction. We label the trajectories taken by $|g_i\rangle$ and $|e_i\rangle$, A and B respectively. The state of an atom at $t = \tau + T_d$ is $|\psi_i(\tau+T_d)\rangle = |\psi_i(\tau+T_d)\rangle_A + |\psi_i(\tau+T_d)\rangle_B$, where $|\psi_i(\tau+T_d)\rangle_A = |g_i\rangle/\sqrt{2}$ and $|\psi_i(\tau+T_d)\rangle_B = -i\,|e_i\rangle/\sqrt{2}$. At the end of this zone, a π-pulse causes the state $|g_i\rangle$ to evolve into $|e_i\rangle$ and vice-versa. The state at the end of this pulse is $|\psi_i(3\tau+T_d)\rangle = |\psi_i(3\tau+T_d)\rangle_A + |\psi_i(3\tau+T_d)\rangle_B$, such that $|\psi_i(3\tau+T_d)\rangle_A = -i\,|e_i\rangle/\sqrt{2}$ and $|\psi_i(3\tau+T_d)\rangle_B = -\,|g_i\rangle/\sqrt{2}$. Following the second dark zone of duration T_d, the two trajectories converge, as shown in Fig. 4.1(c), and $|\psi_i(3\tau+2T_d)\rangle = |\psi_i(3\tau+T_d)\rangle$. At $t = 3\tau+2T_d$, a third pulse of duration τ is applied to the atoms. If a phase-difference of ϕ is introduced between the paths, the state of the atom at the end of the last $\pi/2$-pulse is $|\psi_i(4\tau+2T_d)\rangle = |\psi_i(4\tau+2T_d)\rangle_A + |\psi_i(4\tau+2T_d)\rangle_B$, where $|\psi_i(4\tau+2T_d)\rangle_A = -i(-i\exp(-i\phi)\,|g_i\rangle + |e_i\rangle)/2$ and $|\psi_i(4\tau+2T_d)\rangle_B = -(|g_i\rangle - i\exp(i\phi)\,|e_i\rangle)/2$. This phase-difference can occur, for example, due to a rotation of the entire system about the **y**-direction.

The final fringe pattern is the result of the interference of the states from the two trajectories. This is observed by measuring the probability of finding the atom in either of the two states. The signal as a measure of the amplitude of $|g\rangle$, is therefore, $S_{CRAIN} = |(1+\exp(-i\phi))/2|^2 = \cos^2(\phi/2)$. We note now that the state $|\Psi\rangle$ of the ensemble is the direct product of its constituent atoms: $|\Psi\rangle = \prod_{i=1}^{N} |\psi_i\rangle$ [**39**,**40**]. The signal of the COSAIN is a measurement of any of the arising collective states. We choose to measure the state

$|E_0\rangle$, so that the resulting signal is the probability of finding all the atoms of the ensemble simultaneously in $|g\rangle$. This choice of state will be explained later on when we discuss the detection system of the COSAIN. The signal of the COSAIN is thus the product of the signals from the constituent atoms, $S_{COSAIN} = \prod_{i=1}^{N} S_{CRAIN} = \cos^{2N}(\phi/2)$. The fringe linewidth as a function of ϕ decreases with increasing N. We define this linewidth as the full width at half maximum (FWHM) of the signal fringe, $\varrho(N) = 2\cos^{-1}(2^{-1/2N})$. We have verified that $\varrho(1)/\varrho(N) \approx \sqrt{N}$.

4.2.1. Physical Interpretation of Fringe Narrowing

The narrowing of the signal fringes in a COSAIN can be understood by considering the physical properties of the collective excitations. If the ensemble in the ground state interacts with a single photon of momentum $\hbar k$, it will oscillate between $|E_0, 0\rangle \leftrightarrow |E_1, \hbar k\rangle$. Consequently, it will exhibit collective behavior such that its center of mass recoils with a velocity in the **z**-direction equal to $\hbar k/Nm$. Thus, this ensemble can be viewed as a single entity with a mass of Nm, and a Compton frequency, ω_C that is N times that of a single atom, despite no interaction between the atoms. Conversely, the ensemble can be viewed as having a λ_{dB} of h/Nmv that is N times lower than that of a single atom, where v is the magnitude of its total velocity (e.g., a constant velocity in the **x**-direction that is much larger than the velocity in the **z**-direction due to the recoil). In the ideal case of uniform Rabi-frequencies and no Doppler shift related detunings, the first $\pi/2$-pulse splits the ensemble into a superposition of $N + 1$ symmetric collective states (we have shown the corresponding interpretation of the other, more general cases in ref. [**39**]). The state $|E_n\rangle$ receives a recoil of $n\hbar k$ due to the first $\pi/2$-pulse and is deflected in the **z**-direction

by $n\hbar kT_d/Nm$ by the end of the first dark zone, making an angle $\theta_n = \tan^{-1}(n\hbar k/Nmv)$ with the **x**-axis. We label the path taken by this state as Path-n. The subsequent π-pulse causes $|E_n\rangle$ to evolve to $|E_{N-n}\rangle$. This results in the deflection of the trajectory of the states so that all the $N+1$ trajectories converge by the end of the second dark-zone. The third pulse causes each of the $N+1$ states to split further. The resulting COSAIN is, thus, $J(N+1,2)$ collective interferometers operating simultaneously. Of these, there are x interferometers of area $(N-x+1)\Theta/N$, producing signal fringe amplitudes equaling $\cos^2((N-x+1)\phi/2)$, where x assumes values $1, 2, \ldots, N$. The interference between these cosinusoidal fringes result in the narrowing of the total fringe width. In what follows, we illustrate the physical mechanism behind this narrowing by considering first the role of Compton frequency in a CRAIN. We then extend this analysis to an ensemble of N atoms to describe the phenomenon of narrowing in the COSAIN.

We consider the product state of the atom and a Fock state with N' photons denoted by $|N'\rangle$ or with $N'-1$ photons denoted by $|N'-1\rangle$. Thus, at $t=0$, the atom photon system is assumed to be in the state $|g\rangle\,|N'\rangle \equiv |g, N'\rangle$. The atom-field interaction couples it to the state $|e\rangle\,|N'-1\rangle \equiv |e, N'-1\rangle$, as illustrated in Fig. 4.2(a). We assume that the photon energy, $\hbar\omega$, exactly matches the energy difference between the atomic internal states $|e\rangle$ and $|g\rangle$. We define the dressed frequency of the atom-photon system as ω_{PA}, which is a constant, for all possible states of the system. If we define $\omega_{C,e} = m_e c^2/\hbar$ as the Compton frequency of the excited atom, where $m_e = m_g + \hbar\omega/c^2$ is the rest mass of the excited atom, and $m_g = m$ is the rest mass of the atom in the ground state, then we have $\omega_{PA} = m_e c^2/\hbar + (N'-1)\omega = m_g c^2/\hbar + N'\omega$. The Compton frequency of the atom in the ground state is $\omega_{C,g} = m_g c^2/\hbar$. The effect of temporal

phase accumulation on the system during an interval Δt, if the system is in an arbitrary superposition of $|g\rangle$ and $|e\rangle$, i.e. $c_g|g\rangle + c_e|e\rangle$ at the start of the interval, will be $\exp(-i\omega_{PA}\Delta t)(c_g|g,N'\rangle + c_e|e,N'-1\rangle)$. Thus, after the first $\pi/2$ pulse of a time duration, τ, the quantum state of the system is $\exp(\omega_{PA}\tau)(|g,N'\rangle_A - i|e,N'-1\rangle_B)/\sqrt{2}$, where the subscripts A and B indicate the lower and upper trajectory of the interferometer, respectively. This is followed by a dark zone of duration T_d at the end of which the quantum state of the system is $\exp(-i\omega_{PA}(\tau+T_d))(|g,N'\rangle_A - i|e,N'-1\rangle_B)/\sqrt{2}$. A π-pulse is applied at the end of the first dark zone, and therefore, at $t = 3\tau + T_d$, the quantum state of the system is $|\psi(3\tau+T_d)\rangle = |\psi(3\tau+T_d)\rangle_A + |\psi(3\tau+T_d)\rangle_B$, where $|\psi(3\tau+T_d)\rangle_A = -i\exp(-i\omega_{PA}(3\tau+T_d))|e,N'-1\rangle/\sqrt{2}$ and $|\psi(3\tau+T_d)\rangle_B = -\exp(-i\omega_{PA}(3\tau+T_d))|g,N'\rangle/\sqrt{2}$. At this point the second dark zone begins, at the end of which the state of the system can be written as $|\psi(3\tau+2T_d)\rangle = |\psi(3\tau+2T_d)\rangle_A + |\psi(3\tau+2T_d)\rangle_B$, where $|\psi(3\tau+2T_d)\rangle_A = -i\exp(-i\omega_{PA}(3\tau+2T_d))|e,N'-1\rangle/\sqrt{2}$ and $|\psi(3\tau+2T_d)\rangle_B = -\exp(-i\omega_{PA}(3\tau+2T_d))|g,N'\rangle/\sqrt{2}$. Finally, the last $\pi/2$-pulse causes each of the arms to further split in to $|g,N'\rangle$ and $|e,N'-1\rangle$, so that the state of the system at $t = 4\tau + 2T_d$ is given by $|\psi(4\tau+2T_d)\rangle = |\psi(4\tau+2T_d)\rangle_A + |\psi(4\tau+2T_d)\rangle_B$, where

$$
\begin{aligned}
|\psi(4\tau+2T_d)\rangle_A &= \frac{-i}{2}\exp(-i\omega_{PA}(4\tau+2T_d)) \\
&\quad\times(-i|g,N'\rangle + |e,N'-1\rangle), \\
|\psi(4\tau+2T_d)\rangle_B &= \frac{-1}{2}\exp(-i\omega_{PA}(4\tau+2T_d)) \\
&\quad\times(|g,N'\rangle - i|e,N'-1\rangle).
\end{aligned}
\tag{4.2}
$$

The two arms, thus, yield identical proportions of $|g, N'\rangle$ and $|e, N'-1\rangle$. The probability of finding the atom in the ground state, which is the signal for the CRAIN, is therefore, $S_{CRAIN} = 1$. However, if the entire system is rotating at the rate Ω_G about an axis perpendicular to the area carved by the interferometer, a time delay, ΔT is introduced between the two paths. To consider its effect on the signal of the CRAIN, we note that the state of the system at $t = 3\tau + 2T_d$ is such that

$$\begin{aligned}
|\psi(3\tau + 2T_d)\rangle_A &= \frac{-i}{\sqrt{2}} \exp(-i\omega_{PA}(3\tau + 2T_d)) \\
&\quad \times \exp(i(\omega_{C,g} + \omega_{C,e})\Delta T/4) \, |e, N'-1\rangle \, , \\
|\psi(3\tau + 2T_d)\rangle_B &= \frac{-1}{\sqrt{2}} \exp(-i\omega_{PA}(3\tau + 2T_d)) \\
&\quad \times \exp(-i(\omega_{C,e} + \omega_{C,g})\Delta T/4) \, |g, N'\rangle \, .
\end{aligned} \tag{4.3}$$

Finally, the state of the system due to rotation at the end of the $\pi/2$-dark-π-dark-$\pi/2$ sequence is such that

$$\begin{aligned}
|\psi(4\tau + 2T_d)\rangle_A &= \frac{-i}{2} \exp(-i\omega_{PA}(4\tau + 2T_d)) \\
&\quad \times \exp(i\omega_{C,avg}\Delta T/2)(-i \, |g, N'\rangle \\
&\quad + |e, N'-1\rangle), \\
|\psi(4\tau + 2T_d)\rangle_B &= \frac{-1}{2} \exp(-i\omega_{PA}(4\tau + 2T_d)) \\
&\quad \times \exp(-i\omega_{C,avg}\Delta T/2)(|g, N'\rangle \\
&\quad - i \, |e, N'-1\rangle),
\end{aligned} \tag{4.4}$$

where $\omega_{C,avg} = (\omega_{C,g} + \omega_{C,e})/2$. The probability of finding the atom in the ground state, which is the signal for the CRAIN, is therefore given by $S_{CRAIN} = \cos^2(\phi/2)$, where $\phi = \omega_{C,avg}\Delta T$. From the special relativistic addition of velocities along the two trajectories, the time delay is found to be $\Delta T = 2\theta\Omega_G/c^2$, where θ is the area enclosed by the CRAIN [**28**]. In a real experiment, one makes use of a laser, which is a coherent state, and not a Fock state. However, when the mean photon number in the laser is very large, the excitation is akin to what we described here. In effect, the laser in this limit can be viewed effectively as a Fock state with a photon number equaling the mean photon number in the laser. This is the semiclassical approximation, where the quantum state of the field is assumed to remain unchanged (and thus factorized) independent of the state of the atom.

Next, we consider an ensemble of N such two level atoms that are independent and non-interacting. Furthermore, we consider the product state of this ensemble and a Fock state of N' photon as described above. Initially, all the atoms are in the state $|g\rangle$, so that the state of the ensemble-photon system is $|E_0\rangle\,|N'\rangle \equiv |E_0, N'\rangle$, where $|E_0\rangle = |g_1, g_2, \ldots, g_N\rangle$. Now, let us imagine a scenario (which is impossible in practice) that the state $|E_0, N'\rangle$ is directly coupled to the state $|E_N, N' - N\rangle$ via the exchange of N photons between the states, where $|E_N\rangle = |e_1, e_2, \ldots, e_N\rangle$ as illustrated in 4.2(b). Such a process can be used to realize an atomic interferometer in a manner analogous to the CRAIN, as illustrated in 4.2(c). The area enclosed in this case would be the same as that for a CRAIN. However, the average Compton frequency will now be $N\omega_{C,avg}$ (and the de Broglie wavelength will be $\lambda_{dB,SingleAtom}/N$), so that the signal given by the population of state $|E_0\rangle$ measured at the end, will be $S_{ensemble} = \cos^2(N\phi/2)$, where ϕ is the phase shift experienced by a CRAIN for the same amount of rotation.

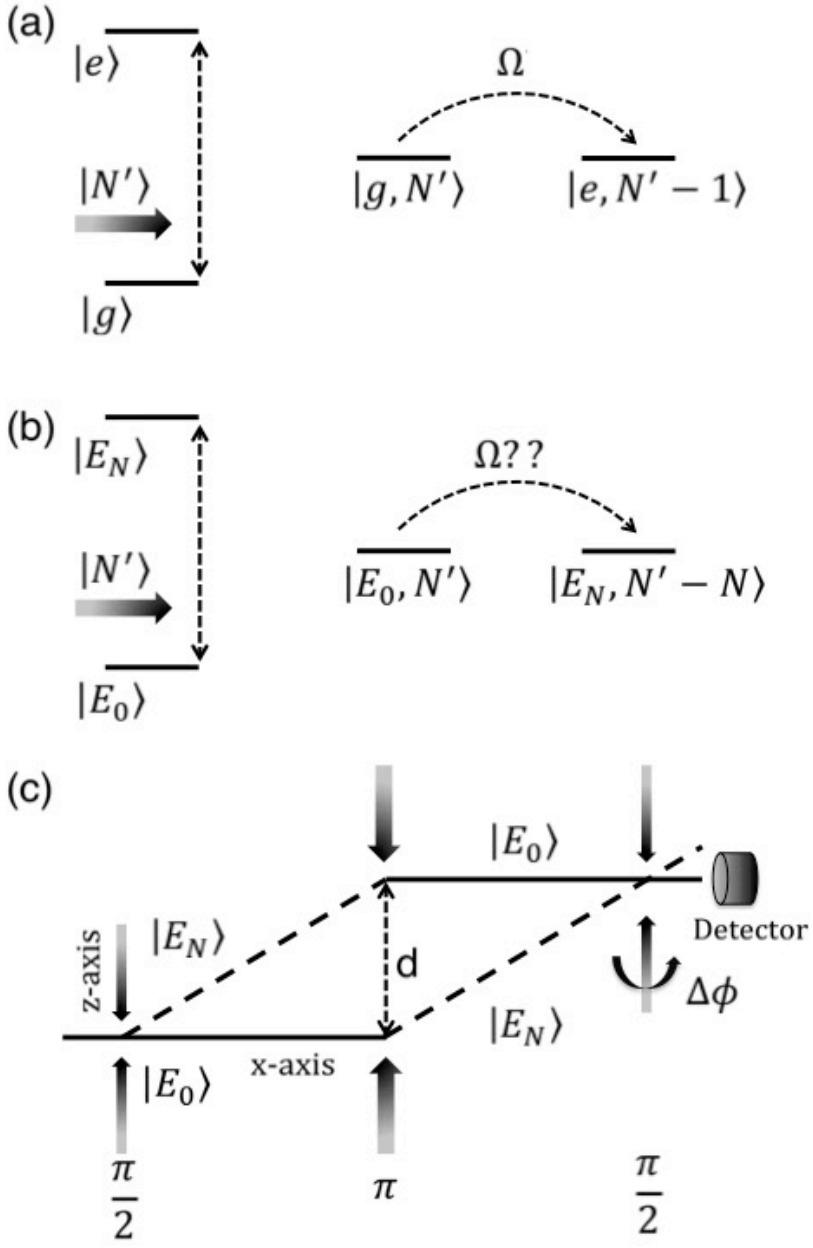

Figure 4.2. (a) Single atom coupled to an N'-photon state, (b)N-atom ensemble coupled to an N'-photon state, (c) Ensemble interferometer formed by splitting and recombining of $|E_0\rangle$ and $|E_N\rangle$.

However, since the electric dipole moment for a superposition of $|E_0\rangle$ and $|E_N\rangle$ vanishes, there is no way to realize the type of excitation envisioned above. Instead, when excited by a Fock state of $N'(> N)$ photons, this ensemble unfolds into a superposition of $(N+1)$ symmetric collective states given by $|E_n\rangle\,|N'-n\rangle$, where $|N'-n\rangle$ is a state of the field with $(N'-n)$ photons and $|E_n\rangle = J(N,n)^{-1/2}\sum_{k=1}^{J(N,n)} P_k\,|g^{\otimes(N-n)}e^{\otimes n}\rangle$, $J(N,n) = \binom{N}{n}$, P_k is the permutation operator, and $n = 0, 1, 2, \ldots, N$ [**36**]. The state $|E_n\rangle$ has a momentum of $n\hbar k$ in the direction of the beam, since it has absorbed n photons. Thus, it will exhibit collective behavior such that its center of mass (COM) recoils with a velocity equal to $n\hbar k/Nm$. As such, an ensemble in such a state can be viewed as a single entity with a mass of Nm and a Compton frequency ω_C that is N times that of a single constituent atom, despite no interaction between the atoms. Conversely, the ensemble can also be viewed as having a de Broglie wavelength $\lambda_{dB} = h/Nmv$ that is N times smaller than that of a single atom, where v is the magnitude of the total velocity (e.g., a constant velocity in the **x**-direction that is much larger than the recoil velocity). This is illustrated schematically in Fig 4.3.

Some of these states and their relevant couplings are illustrated in Fig. 4.4. For example, state $|E_0, N'\rangle$ is coupled to the state $|E_1, N'-1\rangle$ at the rate of $\sqrt{N}\Omega_{N'}$, where $\Omega_{N'} = \sqrt{N'}\Omega_0$, with Ω_0 being the single-photon Rabi frequency (for exciting a single atom) and the $\sqrt{N}$ factor results from the collective enhancement of coupling. If the excitation is carried out by a laser field where the mean photon number is much larger than N, then we can make a semiclassical approximation that $\Omega_{N'} \cong \Omega_{N'-1} \cong \ldots \cong \Omega_{N'-N} \equiv \Omega$. Furthermore, the quantum state of the laser remains unchanged, (and thus factorized) independent of the state of the ensemble. The Compton frequency of the state $|E_n\rangle$ is given

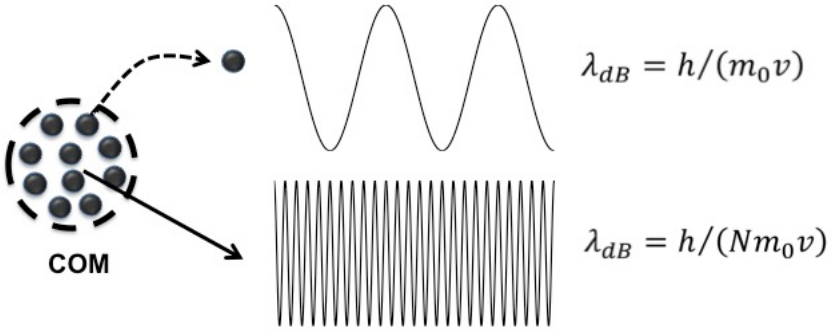

Figure 4.3. λ_{dB} of an Rb-87 atom moving at a constant velocity of 1 m/s is 4.56 nm). In the rest frame of the atom, its characteristic Compton frequency is $1.96(10^{25}$Hz). A cluster of 10^6 such atoms will exhibit the characteristics of a single entity of mass that is a million times that of a single Rb-87 atom. Therefore, λ_{dB} will be $4.56(10^{-15}$ m) and Compton frequency is $1.96(10^{31}$ Hz).

by $\omega_{C,En} = m_{En}c^2/\hbar$, where $m_{En} = m_{E0} + n\hbar\omega/c^2$ is the rest mass of the ensemble in state $|E_n\rangle$, and $m_{E0} = Nm$ is the rest mass of the ensemble in state $|E_0\rangle$. Thus, the dressed frequency of the ensemble-photon system ω_{PE}, which is a constant for all possible states of the system can be written as $\omega_{PE}(N, N') = m_{En}c^2/\hbar + (N' - n)\omega = m_{E0}c^2/\hbar + N'\omega$.

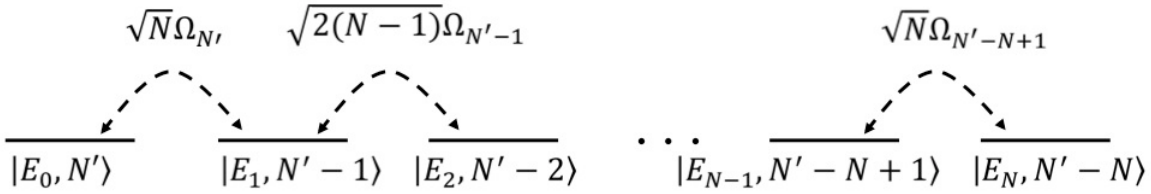

Figure 4.4. Coupling between an N-atom ensemble symmetric collective states and N' photons.

In the absence of an effective detuning, the COSAIN is based on the coherent splitting and recombining of all of these symmetric collective states. The signal of the COSAIN is, thus, the product of the signals of the constituent CRAIN's that work simultaneously, resulting in the narrowing of the signal fringes. The fringe linewidth,

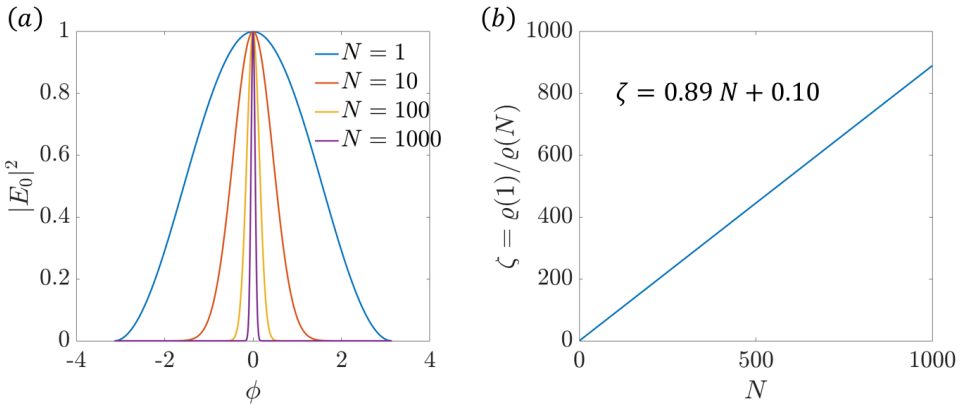

Figure 4.5. (a) Measurement of the COSAIN signal (amplitude of $|E_0\rangle$) shows a narrowing of the fringe width. (b) The ratio $\varrho(1)/\varrho(N)$ increases with $\sqrt{N}$.

defined as the full width at half maximum (FWHM) of the signal fringe is given by $\varrho(N) = 2\cos^{-1}(2^{-1/2N})$. It is evident from Fig. 4.5 that the $\varrho(N)$ decreases with increasing N. To illustrate the mechanism behind the COSAIN more transparently, we now consider the simplest ensemble: an assembly of two atoms of the kind described above and N' photons. At $t = 0$, the ensemble-photons system is assumed to be in the state $|E_0, N'\rangle$. The atom-field interaction couples it to the state $|E_1, N'-1\rangle$, which in turn is coupled to the state $|E_2, N'-2\rangle$. Following the notations of the $\pi/2$-dark-π-dark-$\pi/2$ sequence established for the CRAIN, the state of the ensemble after the first $\pi/2$ pulse is $|\Psi(\tau)\rangle = \exp(-i\omega_{PE}\tau)(|E_0, N'\rangle_A - i\sqrt{2}\,|E_1, N'-1\rangle_B - |E_2, N'-2\rangle_C)/2$, where $\omega_{PE} \equiv \omega_{PE}(2, N')$ and the subscripts A, B, and C denote the lower, middle and upper trajectories of the interferometer, respectively, as shown in Fig. 4.6. This

is followed by a dark zone of duration T_d, at the end of which the state of the ensemble is $|\Psi(\tau + T_d)\rangle = \exp(-i\omega_{PE}T_d)\,|\Psi(\tau)\rangle$. The component $|E_1, N' - 1\rangle_B$ is displaced by $\hbar k T_d/2m$ along the **z**-axis since it has absorbed the recoil from one photon ($\hbar k$), and it has a mass of $2(m_{C,g} + m_{C,e}) \approx 2m$. Similarly, $|E_2, N' - 2\rangle$ is displaced by $\hbar k T_d/m$ along the **z**-axis since it has absorbed recoils from two photons ($2\hbar k$), and it has a mass of $2m_{C,e} \approx 2m$. At $t = \tau + T_d$, the system interacts with the π-pulse (of duration 2τ) which causes the transition $|E_0, N'\rangle \leftrightarrow |E_2, N' - 2\rangle$. The state $|E_1, N' - 1\rangle$, however only picks up a phase due to the π interaction, and its trajectory remains unchanged. Explicitly, the state of the system at the end of the π-pulse is $|\Psi(3\tau + T_d)\rangle = |\Psi(3\tau + T_d)\rangle_A + |\Psi(3\tau + T_d)\rangle_B + |\Psi(3\tau + T_d)\rangle_C$, where

$$
\begin{aligned}
|\Psi(3\tau + T_d)\rangle_A &= -\frac{1}{2}\exp(-i\omega_{PE}(3\tau + T_d))\,|E_2, N' - 2\rangle\,, \\
|\Psi(3\tau + T_d)\rangle_B &= -\frac{1}{\sqrt{2}}\exp(-i\omega_{PE}(3\tau + T_d)) \\
&\qquad \times |E_1, N' - 1\rangle\,, \\
|\Psi(3\tau + T_d)\rangle_C &= \frac{1}{2}\exp(-i\omega_{PE}(3\tau + T_d))\,|E_0, N'\rangle\,.
\end{aligned}
\tag{4.5}
$$

At the end of this pulse, the system passes through a second dark zone of duration T_d, which causes the state of the system to become

$$
|\Psi(3\tau + 2T_d)\rangle = |\Psi(3\tau + 2T_d)\rangle_A + |\Psi(3\tau + 2T_d)\rangle_B + |\Psi(3\tau + 2T_d)\rangle_C\,,
\tag{4.6}
$$

where

$$
|\Psi(3\tau + 2T_d)\rangle_A = \exp(-i\omega_{PE}T_d)\,|\Psi(3\tau + T_d)\rangle_A\,,
\tag{4.7a}
$$

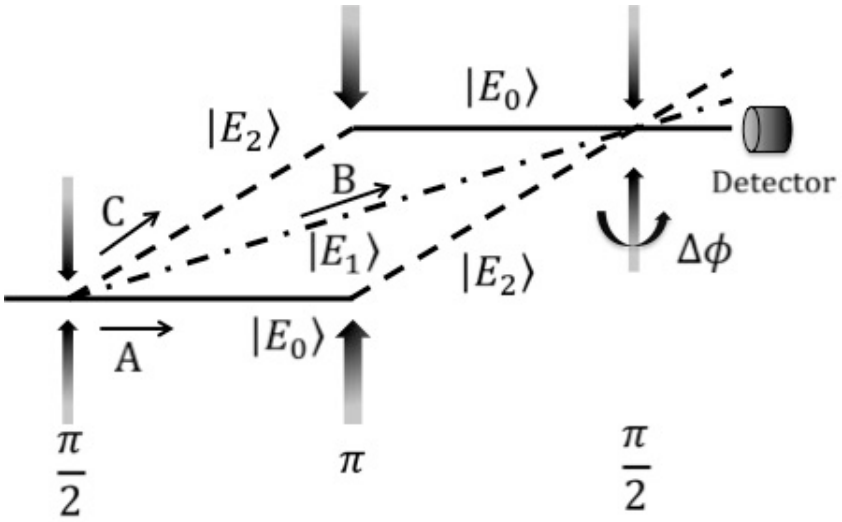

Figure 4.6. Illustration of a two atom COSAIN depicting the state trajectories.

(4.7b) $$ket\Psi(3\tau + 2T_d)_B = \exp(-i\omega_{PE}T_d)\,|\Psi(3\tau + T_d)\rangle_B\,,$$

(4.7c) $$|\Psi(3\tau + 2T_d)\rangle_C = \exp(-i\omega_{PE}T_d)\,|\Psi(3\tau + T_d)\rangle_C\,.$$

By the end of this dark zone, the three trajectories converge and a last $\pi/2$-pulse is applied which causes each of the trajectories to further split as follows:

$$
\begin{aligned}
|\Psi\rangle_A &= \frac{-1}{4}\exp(-i\omega_{PE}(4\tau+2T_d))(-|E_0,N'\rangle \\
&\quad - i\sqrt{2}\,|E_1,N'-1\rangle + |E_2,N'-2\rangle), \\
|\Psi\rangle_B &= \frac{1}{2}\exp(-i\omega_{PE}(4\tau+2T_d))(|E_0,N'\rangle \\
&\quad + |E_2,N'-2\rangle), \\
|\Psi\rangle_C &= \frac{1}{4}\exp(-i\omega_{PE}(4\tau+2T_d))(|E_0,N'\rangle \\
&\quad - i\sqrt{2}\,|E_1,N'-1\rangle - |E_2,N'-2\rangle).
\end{aligned} \tag{4.8}
$$

The signal of the COSAIN is the probability of finding the ensemble in any of the collective states. We choose to measure the probability of $|E_0,N'\rangle$. The probability of finding the ensemble in state $|E_0,N'\rangle$, is therefore, $S_{COSAIN}=1$. However, as explained above for the case of the CRAIN, if the entire system is rotating at the rate Ω_G about an axis perpendicular to the area carved by the interferometer, a time delay is introduced between the paths. This time delay depends only on the area enclosed and the rate of rotation, as noted earlier. Let us assume that the delay between the paths C and A, which forms the $A-C$ loop, is ΔT. Therefore, the delay between paths B and A which form the $A-B$ loop, will be $\Delta T/2$. Similarly, the delay between paths C and B, which form the $B-C$ loop, will also be $\Delta T/2$. Since only the relative delay between two paths matter, we assume, for simplicity, that there is no delay on path B. Thus, just before the final $\pi/2$ pulse, we can write the quantum states of these paths under rotation as $|\Psi\rangle_{BR} = |\Psi(3\tau+2T_d)\rangle_B$, $|\Psi\rangle_{AR} = \exp(i(\omega_{C,E0}+\omega_{C,E2})\Delta T/4)\,|\Psi(3\tau+2T_d)\rangle_A$, and

$|\Psi\rangle_{CR} = \exp(-i(\omega_{C,E2} + \omega_{C,E0})\Delta T/4)\,|\Psi(3\tau + 2T_d)\rangle_C$. The last $\pi/2$-pulse causes each of these components to further split so that the state of the system at the end of the $\pi/2$-dark-π-dark-$\pi/2$ sequence is

$$
\begin{aligned}
|\Psi\rangle_{AR} &= \frac{-1}{4}\exp(-i\omega_{PE}(4\tau + 2T_d)) \\
&\quad \times \exp(i(\omega_{C,E0} + \omega_{C,E2})\Delta T/4) \\
&\quad \times (-|E_0, N'\rangle - i\sqrt{2}\,|E_1, N'-1\rangle + |E_2, N'-2\rangle), \\
|\Psi\rangle_{BR} &= \frac{1}{2}\exp(-i\omega_{PE}(4\tau + 2T_d))(|E_0, N'\rangle \\
&\quad + |E_2, N'-2\rangle), \\
|\Psi\rangle_{CR} &= \frac{1}{4}\exp(-i\omega_{PE}(4\tau + 2T_d)) \\
&\quad \times \exp(-i(\omega_{C,E2} + \omega_{C,E0})\Delta T/4) \\
&\quad \times (|E_0, N'\rangle - i\sqrt{2}\,|E_1, N'-1\rangle - |E_2, N'-2\rangle).
\end{aligned}
\tag{4.9}
$$

The signal of the COSAIN can, thus, be viewed as the aggregation of interference patterns due to three independent CRAIN's working simultaneously., i.e. those formed by paths $A-B$, $B-C$ and $A-C$. To illustrate this, we denote the component of $|E_0, N'\rangle$ in paths A, B and C as χ_A, χ_B and χ_C, respectively. The interferometers formed by $A-B$ and $B-C$ are identical. The measurement of the amplitude of $|E_0, N'\rangle$ from each of these interferometers is given by $S_{A-B} = S_{B-C} = |\chi_A + \chi_B|^2 = |\chi_B + \chi_C|^2 = 3/16 + \cos^2(\omega_{C,avg}\Delta T/2)/4$. This corresponds to a CRAIN that is operating with an atom of average Compton frequency $\omega_{C,avg}$. The interferometer formed by $A-C$ yields the signal value $S_{A-C} = |\chi_A + \chi_C|^2 = \cos^2(\omega_{C,avg}\Delta T)/4$, behaving analogously to a

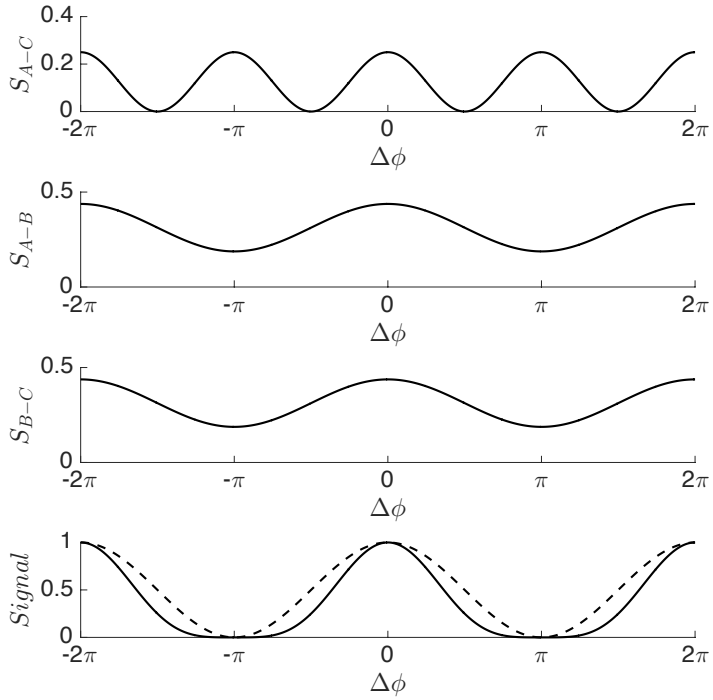

Figure 4.7. Signals derived from the interferometers formed by trajectories $A-C$, $A-B$, and $B-C$. The bottom panel shows the signal of CRAIN (broken line) to the signal of a 2-atom COSAIN (solid line).

CRAIN formed by an atom of average Compton frequency $2\omega_{C,avg}$. The total COSAIN signal arises due to the interference of the component of $|E_0, N'\rangle$ from the three paths, $S_{COSAIN} = |\chi_A+\chi_B+\chi_C|^2 = \cos^4(\omega_{C,avg}\Delta T/2)$, as shown in Fig 4.7. This is reconciled by the fact that $|\chi_A+\chi_B+\chi_C|^2 = |\chi_A+\chi_B|^2+|\chi_B+\chi_C|^2+|\chi_A+\chi_C|^2-(|\chi_A|^2+|\chi_B|^2+|\chi_C|^2)$. The collective atomic recoil laser (CARL) mechanism is similar to this concept presented here, in the sense that no interaction between atoms are needed [**43**, **44**]. On the other hand, the Dicke Phase transition pertains to the BEC regime, and is not closely related to what is being presented here [**45**].

4.3. Parameter Inhomogeneities Affecting Signal

In this section, we present a detailed description of the effect of inhomogeneity in Rabi frequency and Doppler shift on the signal of a COSAIN. These inhomogeneities put significant constraints on the ensemble size, temperature of the trapped atoms, and the intensity profile and size of the laser beams. The manifestations of these effects can be analyzed by considering an ensemble of N identical non-interacting and independent atoms of the type described in Sec. 4.2.1. A laser beam propagating along the **z**-axis will impart a momentum $\hbar k$ to an atom upon absorption of recoil from a single photon, driving it to a superposition of the states $|g_i, 0\rangle$ and $|e_i, \hbar k\rangle$, with the amplitude of each state depending on the intensity of the laser beam and the time of interaction. The field amplitude of the laser beams are assumed to be of Gaussian profile in **x** and **y** directions, and constant in the **z** direction. At $t = 0$, the position of the i-th atom is given by $\tilde{\mathbf{r}} = x_i\hat{\mathbf{x}} + y_i\hat{\mathbf{y}} + z_i\hat{\mathbf{z}}$. Due to the thermal motion of the atoms, each atom experiences a different Doppler shift and therefore, a different effective laser frequency, ω_{0i}. The net consequence of this is that the i-th atom picks up a detuning of $\delta_i = k\mathbf{v_{iz}}$, where $\mathbf{v_{iz}}$ denotes the atom's velocity in the **z**-direction. Furthermore, each atom sees a different electric field, $\mathbf{E_i} = \hat{\mathbf{x}} E_0 \exp(-(x_i^2 + y_i^2)/2/\sigma_L^2) \cos(\omega_{0i} t - k z_i)$, due to the finite extent of the ensemble. Here σ_L represents the width of the laser beam in the transverse directions. Therefore, the Rabi frequency experienced by the i-th atom is given by $\Omega_i = \Omega_0 \exp[-(x^2 + y^2)/2\sigma_L^2]$, where $\Omega_0 \equiv \langle g_i | (\mathbf{x} \cdot \rho_\mathbf{i}) | e_i \rangle E_0/\hbar = \langle e_i | (\mathbf{x} \cdot \rho_\mathbf{i}) | g_i \rangle E_0/\hbar$ and ρ_i is the position of the electron with respect to the nucleus.

In the electric dipole approximation, the Hamiltonian for the i-th atom can be written as $H_i = |\mathbf{p}_i|^2/2m + H_{0i} + q\rho_\mathbf{i}.\mathbf{E_i}$, where H_{0i} is the internal energy of the atom, q is the

electronic charge, m is the mass of the atom, and $\mathbf{p_i}$ is the momentum of the i-th atom. The COM motion kinetic energy term be expressed as $|\mathbf{p}_i|^2/2m = |\mathbf{p}_{iz}|^2/2m + |\mathbf{p}_{i\perp}|^2/2m$, where $\mathbf{p}_{iz}$ is the momentum in the $\mathbf{z}$ direction, and $\mathbf{p}_{i\perp}$ is the momentum in a direction perpendicular to $\mathbf{z}$. Consider first the effect of the second term: $|\mathbf{p}_{i\perp}|^2/2m$. In a typical experimental scenario, this accounts for the motion of the atom, typically at a large velocity, in the $\mathbf{x}$-direction (see Fig. 4.1), acquired, for example by the initial push imparted to the trapped atoms before they enter the first interaction zone. Thus, any variation in this due to a velocity spread within the ensemble can be ignored, and this term can be treated as an overall constant energy which can be subtracted from the Hamiltonian. Consider next the first term: $|\mathbf{p}_{iz}|^2/2m$. This term shows that the state $|g, \mathbf{p_{iz}}\rangle$ coupled to $|e, \mathbf{p_{iz}} + \hbar k\rangle$ by the laser differ in energy by $(\hbar k v_{iz} + \hbar^2 k^2/2m)$, where the first term is the Doppler shift and the second term is the recoil energy which is a constant for all atoms, and can be subtracted from the Hamiltonian. Thus, after subtraction of constant terms, the net effect of the kinetic energy term is to account for the Doppler shift. Finally, as we have shown in detail in ref. [**39**], a fully quantum mechanical description of the COM motion (e.g., by keeping track explicitly of the momentum of the atoms in the $|g\rangle$ and $|e\rangle$ states) is not essential in describing the collective states in the limit where the Rabi frequency of the i-th atom, Ω_i, is large compared to the Doppler shift due to the COM motion. This regime is valid for the COSAIN, and, therefore, a semiclassical description of the COM motion of each atom suffices for the case at hand. Upon making the rotating-wave approximation, H_i can then be expressed in the bases of $|g_i\rangle$ and $|e_i\rangle$ as $H_i/\hbar = \omega_g |g_i\rangle \langle g_i| + \omega_e |e_i\rangle \langle e_i| + \Omega_i(\exp(i(\omega_{0i}t - kz_i)) |g_i\rangle \langle e_i| + h.c.)/2$, where ω_e includes the Doppler shift. Performing the rotating-wave transformation and removing any phase

factors causes the transformation $H_i \rightarrow H_i'$, such that $H_i'/\hbar = -\delta_i \left|e_i'\right\rangle \left\langle e_i'\right| + \Omega_i(\left|g_i'\right\rangle \left\langle e_i'\right| + h.c.)/2$. The new basis vectors, $\left|g_i'\right\rangle$ and $\left|e_i'\right\rangle$, are related to the original basis vectors as $\exp(-i\omega_g t)\left|g_i\right\rangle$ and $\exp(-i((\omega_e + \delta_i)t - kz_i))\left|e_i\right\rangle$, respectively. Assuming that the i-th atom is initially in the state $c_{gi}(0)\left|g_i'\right\rangle + c_{ei}(0)\left|e_i'\right\rangle$, its quantum state can be written as

$$\begin{aligned}\left|\psi_i'\right\rangle =& e^{i\delta_i t/2}((c_{gi}(0)\cos\left(\frac{\Omega_i' t}{2}\right) \\ &- i\frac{c_{gi}(0)\delta_i + c_{ei}(0)\Omega_i}{\Omega_i'}\sin\left(\frac{\Omega_i' t}{2}\right))\left|g_i'\right\rangle \\ &+ (-i\frac{c_{gi}(0)\Omega_i - c_{ei}(0)\delta_i}{\Omega_i'}\sin\left(\frac{\Omega_i' t}{2}\right) \\ &+ c_{ei}(0)\cos\left(\frac{\Omega_i' t}{2}\right))\left|e_i'\right\rangle), \end{aligned} \tag{4.10}$$

where $\Omega_i' = \sqrt{\Omega_i^2 + \delta_i^2}$ is the effective coupling frequency of this atom. The relative separation of the atoms along the direction of propagation of the laser beam has no effect on the fidelity of the collective states that can be attained by the ensemble [**39**]. For the purpose of the present discussion, we stay in the bases of $\left|g_i'\right\rangle$ and $\left|e_i'\right\rangle$.

At $t = 0$, the first pulse of duration τ is applied to the atoms so that $\Omega_0\tau = \pi/2$. The state of the i-th atom following this interaction can be written as $\left|\psi_i'(\tau)\right\rangle = c_{gi}(\tau)\left|g_i'\right\rangle_A + c_{ei}(\tau)\left|e_i'\right\rangle_B$, where $c_{gi}(\tau) = \exp(i\delta_i\tau/2)((\cos\left(\Omega_i'\tau/2\right) - i\delta_i\sin\left(\Omega_i'\tau/2\right)/\Omega_i')$ and $c_{ei}(\tau) = \exp(i\delta_i\tau/2)(-i\Omega_i\sin\left(\Omega_i'\tau/2\right)/\Omega_i')$. The subscripts A and B denote the lower and upper arm of the interferometer trajectory. The ensuing dark zone lasts for a duration T_d wherein the atoms are left to drift freely so that at $t = \tau + T_d$, the COM of state $\left|e_i'\right\rangle$ is separated from that of state $\left|g_i\right\rangle$ by $d = \hbar k T_d/m$. During this dark zone where no atom-light interaction is taking place, the portion of the atom in state $\left|e_i'\right\rangle$ picks up a phase due to

detuning, making the state of the atom at the end of this pulse $|\psi_i'(\tau+T_d)\rangle = c_{gi}(\tau+T_d)\,|g_i'\rangle_A + c_{ei}(\tau+T_d)\,|e_i'\rangle_B$, where $c_{gi}(\tau+T_d) = c_{gi}(\tau)$ and $c_{ei}(\tau+T_d) = \exp(i\delta_i T_d)c_{ei}(\tau)$. At this point a second pulse of duration 2τ (π-pulse) is applied to atoms, and each trajectory undergoes further splitting, as shown in Fig. 4.1. The π-pulse can, in principle, be perfect only for one group of atoms, such as those with $\delta = 0$. For all other atoms, the pulse duration will differ slightly from π. As a result, for example, the $|e_i'\rangle$ state will not fully evolve into the $|g_i'\rangle$ state, and a residual amount will stay in the $|e_i'\rangle$ state. In the regime where $\Omega_i \gg \delta_i$ for all i, the effect of these residual components can be safely ignored. Under this approximation, the state of the atom is given by $|\psi_i'(3\tau+T_d)\rangle = c_{ei}(3\tau+T_d)\,|e_i'\rangle_A + c_{gi}(3\tau+T_d)\,|g_i'\rangle_B$, where $c_{ei}(3\tau+T_d) = \exp(i\delta_i\tau)c_{gi}(\tau+T_d)(-i\Omega_i \sin(\Omega_i'\tau)/\Omega_i')$ and $c_{gi}(3\tau+T_d) = \exp(i\delta_i\tau)c_{ei}(\tau+T_d)(-i\Omega_i \sin(\Omega_i'\tau)/\Omega_i')$. Following the π-pulse, the atoms are further set adrift in another dark zone of duration T_d, where the component of the atom following trajectory A picks up a phase due to detuning. The net effect of this is that

$$|\psi_i'(3\tau+2T_d)\rangle = c_{ei}(3\tau+2T_d)\,|e_i'\rangle_A + c_{gi}(3\tau+2T_d)\,|g_i'\rangle_B\,, \tag{4.11}$$

where $c_{ei}(3\tau+2T_d) = \exp(i\delta_i T_d)c_{ei}(3\tau+T_d)$ and $c_{gi}(3\tau+2T_d) = c_{ei}(3\tau+T_d)$. By the end of this dark zone, the two trajectories converge and a third pulse of duration τ is applied to the atoms. Therefore, the state of the atom at $t = 4\tau+2T_d$ is

$$\begin{aligned}|\psi_i'(4\tau+2T_d)\rangle = &(c_{gi}(4\tau+2T_d)_A\,|g_i'\rangle + c_{ei}(4\tau+2T_d)_A\,|e_i'\rangle)\\ &+ (c_{gi}(4\tau+2T_d)_B\,|g_i'\rangle + c_{ei}(4\tau+2T_d)_B\,|e_i'\rangle),\end{aligned} \tag{4.12}$$

where

$$
\begin{aligned}
c_{gi}(4\tau+2T_d)_A &= \exp(i\delta_i\tau/2)c_{ei}(3\tau+2T_d)(-i\Omega_i\sin(\Omega_i'\tau/2)/\Omega_i'),\\
c_{ei}(4\tau+2T_d)_A &= \exp(i\delta_i\tau/2)c_{ei}(3\tau+2T_d)(\cos(\Omega_i'\tau/2)+i\delta_i\sin(\Omega_i'\tau/2)/\Omega_i'),\\
c_{gi}(4\tau+2T_d)_B &= \exp(i\delta_i\tau/2)c_{gi}(3\tau+2T_d)(\cos(\Omega_i'\tau/2)-i\delta_i\sin(\Omega_i'\tau/2)/\Omega_i'),\\
c_{ei}(4\tau+2T_d)_B &= \exp(i\delta_i\tau/2)c_{gi}(3\tau+2T_d)(-i\Omega_i\sin(\Omega_i'\tau/2)/\Omega_i'). \qquad (4.13)
\end{aligned}
$$

The signal of the CRAIN formed by the i-th atom is the measurement of the amplitude of state $|g_i'\rangle$ at the end of the $\pi/2$-dark-π-dark-$\pi/2$ sequence due to the interference of the components from the two paths. Since the two arms yield identical proportions of both $|g_i'\rangle$ and $|e_i'\rangle$, i.e. $c_{gi}(4\tau+2T_d)_A = c_{gi}(4\tau+2T_d)_B$ and $c_{ei}(4\tau+2T_d)_A = -c_{ei}(4\tau+2T_d)_B$, the signal of the CRAIN formed is $S_{CRAIN,i} = \alpha_i$, where $\alpha_i = |2c_{gi}(4\tau+2T_d)_A|^2 \leq 1$. Since the signal of a COSAIN is the product of the signals of the individual CRAIN's formed by the constituent atoms in the ensemble [**39**], the signal of the resulting COSAIN is, consequently, $S_{COSAIN} = \prod_i^N S_{CRAIN,i} = \prod_i^N \alpha_i$. However, if a phase difference is introduced between the two paths, the signal of the CRAIN's and thus, the COSAIN will depend on it additionally. Assuming that an external phase, ϕ is introduced to the path A of the interferometer, the quantum state of the atom at $t = 4\tau + 2T_d$ is given by $|\psi_i'(4\tau+2T_d)\rangle = \exp(i\phi)(c_{gi}(4\tau+2T_d)_A|g_i'\rangle + c_{ei}(4\tau+2T_d)_A|e_i'\rangle) + (c_{gi}(4\tau+2T_d)_B|g_i'\rangle + c_{ei}(4\tau+2T_d)_B|e_i'\rangle)$. The amplitude of $|g_i'\rangle$ will, thus, be $S_{CRAIN,i} = |1+\exp(-i\phi)|^2\alpha_i = 4\alpha_i\cos^2(\phi/2)$. In the case where $\Omega_i \gg \delta_i$, $\alpha_i = 1/4$ and the signal shows the well known $\cos^2(\phi/2)$ dependence. The resulting COSAIN signal is, therefore, $S_{COSAIN} = \prod_i^N 4\alpha_i\cos^2(\phi/2)$. In the ideal situation where each atom sees the same Rabi

frequency due to a uniform beam profile and there is no effective detuning experienced by the atoms, $\alpha_i = 1/4$ and the signal at the end of the interferometer sequence is given by $S_{COSAIN} = \cos^{2N}(\phi/2)$. This corresponds to the narrowing of the signal fringe by a factor proportional to $\sqrt{N}$ as compared to the signal in a CRAIN.

In the more practical situation relevant for experimental conditions, Ω_i and δ_i for each atom are determined by the laser beam intensity profile, and atom trap size and temperature, as described above. To illustrate the effect of these parameters, we assume that the atoms are first cooled down using a magneto-optic trap arrangement. The trapped atoms are then held in a cigar-shaped dipole trap to further cool them down via evaporative cooling. The density of atoms in the trap is assumed to follow a Gaussian spatial distribution so that its length is in the longitudinal direction is ξ_L, and its width in the transverse direction is ξ_T.

4.3.1. Effect of Velocity Distribution

The Maxwell-Boltzmann velocity distribution of the ensemble is

$$f_{MB}(v, T_{MB}) = \sqrt{m/2\pi k_B T_{MB}} \times \exp\left(\frac{-mv^2}{2\pi k_B T_{MB}}\right), \tag{4.14}$$

where T_{MB} is the temperature of the trap and k_B is the Boltzmann constant. Since the ensemble undergoes interaction with a pair of counter-propagating laser beams, the Doppler shift observed by the i-th atom, $\delta_i = (k_1 + k_2)v_i$ cannot be neglected compared to the Raman-Rabi frequency experienced by it. Thus, at non-zero ensemble temperatures, the signal contribution from each atom is significantly lower than the maximum amplitude possible. The signal peak value falls sharply with increasing N as illustrated in Fig 4.8(a).

It is also evident from Fig. 4.8(b) that the signal of a COSAIN varies significantly as a function of the temperature.

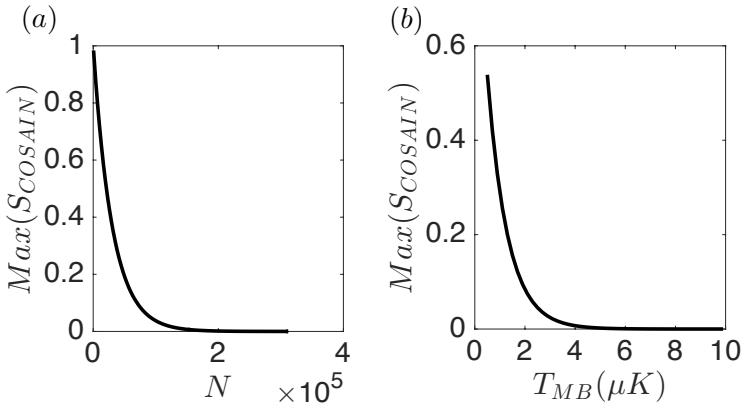

Figure 4.8. (a) Variation of signal peak value with N at 0.5μK average temperature and rectangular intensity profile beams at $\Omega = 1.9 \times 10^7 \mathrm{s}^{-1}$. (b) Variation of signal peak value with trap temperature for $N \simeq 1.9 \times 10^4$.

4.3.2. Effect of Intensity Profile of Laser Beams

Next, we consider the effect of the Gaussian spatial distribution of the Raman beams on the COSAIN. Assuming that the beam waist size is w, the Raman Rabi frequency experienced by the i-th atom of the ensemble is $\Omega_i = \Omega_0 \exp(-2r^2/w^2)$. Here Ω_0 is the peak value of the Raman Rabi frequency and r is the radial distance of the i-th atom from the center of the beam. We consider that the average temperature of the trapped atoms is $T_{MB} = 0.5\mu$K and the peak value of the beam intensity is 15 mW/mm^2 so that $\Omega_0 = 1.9 \times 10^7$ rad/s. Figure 4.9 shows the variation of the peak value of the S_{COSAIN} with increasing value of $\varsigma = w/\xi_T$.

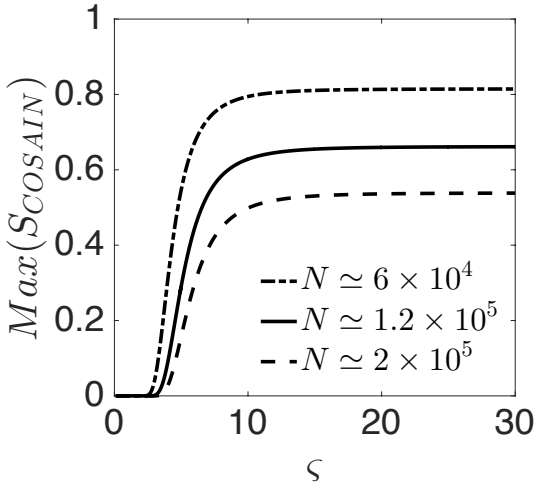

Figure 4.9. Variation of the peak value of the S_{COSAIN} with increasing MOT size to beam waist ratio at $T_{MB} = 0.5\mu$K for different values of N.

4.3.3. Effect of spontaneous emission

In our analysis of the COSAIN, we have employed a model of a three-level atom where the intermediate state ($|a, \hbar k_1\rangle$) is adiabtically eliminated to reduce the system to an equivalent two-level model. However, the actual population of this state is approximately Ω^2/δ^2, with $\Omega = \Omega_1 = \Omega_2$. In the time that it takes for a 2π pulse ($\pi/2 - \pi - \pi/2$ sequence sans the dark zones), we can estimate that the number of spontaneous emissions that occur per atom is $2(\Omega^2/\delta^2)\tau\Gamma \simeq 4\pi\Gamma/\delta$. For $\delta = 200\Gamma$, this number is about 6.3×10^{-2} and increases by a factor of N for an ensemble of N atoms. Note that there is no enhancement in the rate of spontaneous emission due to superradiant effects, since we are considering a dilute ensemble. Consequently, the signal for both the CRAIN and the COSAIN would deviate from the ideal one. The effect of spontaneous emission on the CRAIN can be taken into account by using the density matrix equation for a three level system. However, in this case, it is not possible to ascribe a well defined quantum state for each atom. This,

in turn, makes it difficult to figure out the response of the COSAIN, since our analysis for the COSAIN is based on using the direct product of the quantum state of each atom. For a large value of N, it is virtually impossible to develop a manageable density matrix description of the system directly in terms of the collective states. However, it should be possible to evaluate the results of such a density matrix based model for a small value of N (< 10, for example). This calculation is a subject of our future work.

For the general case of large N, one must rely on an experiment (which, in this context, can be viewed as an analog computer for simulating this problem) to determine the degree of degradation expected from residual spontaneous emission. It should be noted that the detrimental effect of spontaneous emission, for both the CRAIN and the COSAIN, can be suppressed to a large degree by simply increasing the optical detuning while also increasing the laser power. This is the approach used, for example, in reducing the effect of radiation loss of atoms in a far off resonant trap (FORT).

4.3.4. Effect of fluctuation in number of atoms

In both the CRAIN and the COSAIN, the signal is collected multiple times and averaged to increase the signal to noise ratio (SNR). The number of atoms in the ensemble can vary in each run. In the CRAIN, a fluctuation of ΔN in N is reflected in the signal amplitude by the same amount while the linewidth does not change. This can be easily deduced from the fact that $S_{CRAIN} = N\cos^2(\phi/2)$. Replacing N by ΔN will change the signal. However, the FWHM which occurs at $S_{CRAIN} = N/2$, will not change. More details on the classical and quantum noise in the CRAIN and the COSAIN are given in Sec.4.6.1.

In this section, we discuss how the fluctuation in the number of atoms in every run of the experiment affects the signal of the COSAIN.

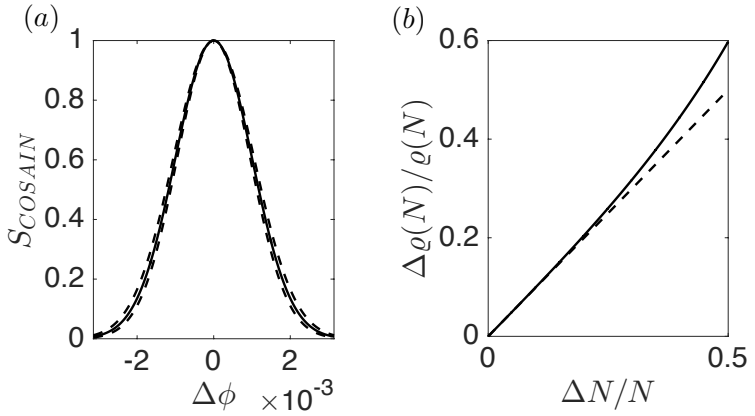

Figure 4.10. (a) S_{COSAIN} for $N = 2 \times 10^5$. (b) Plot of $\Delta\varrho/\varrho$ as a function of $\Delta N/N$.

The signal of the COSAIN due to a fluctuation of ΔN in N is given by $S_{COSAIN} = \cos(\phi/2)^{2(N\pm\Delta N)}$. Fig. 4.10(a) shows plot of a COSAIN signal with $N = 2 \times 10^5$. The broken lines represent the case where $\Delta N/N = 0.1$. As is evident from the above discussion, the linewidth increases (decreases) with decreasing (increasing) ΔN. However, the peak of the signal remains at unity, as opposed to the effect of inhomegneity of field and velocity distribution. The signal linewidth of the COSAIN is approximately $\varrho(N) = \varrho(1)/\sqrt{N}$. A fluctuation of ΔN in N is reflected in the linewidth uncertainty as $\Delta\varrho(N) = \varrho(1)((N - \Delta N)^{-1/2} - (N + \Delta N)^{-1/2})$. The fractional fluctuation is, therefore, $\Delta\varrho(N)/\varrho(N) \simeq (1 - \Delta N/N+)^{-1/2} - (1 + \Delta N/N+)^{-1/2} = \Delta N/N + 0.625(\Delta N/N)^3 + 0.492(\Delta N/N)^5 + O[(\Delta N/N)^6]$. This relation is depicted in Fig.9(b) by the broken line. For small $\Delta N/N$, the fractional change in FWHM is $\Delta\varrho(N)/\varrho(N) \simeq \Delta N/N$ to a good approximation, as shown by the solid line in Fig. 4.10(b).

4.4. Details of Proposed Experiment

In order to illustrate the complete picture of the proposed experiment, we consider ^{87}Rb as the atomic species as an example. We assume a scenario where the atoms will be evaporatively cooled to a temperature of about 2μK, in a dipole force trap [**46**] and then released. The Raman pulses will be applied while these atoms are falling under gravity. Each Raman pulse will consist of a pair of counterpropagating, right circularly polarized (σ_+) beams. One of these beams is red detuned from the $F = 1 \rightarrow F' = 1$ transition in the $D1$ manifold by $\sim$ 1.5GHz, and the other one is red detuned by the same amount from $F = 2 \rightarrow F' = 1$ transition, also in the $D1$ manifold. The second Raman beam is generated from the first one by a modulator which is driven by an ultrastable frequency synthesizer (FS) tuned to 6.8346826109 GHz. We assume that the atoms are initially in the $F=1$,$m_F=0$ state.

Thus, the states $|g\rangle$ and $|e\rangle$ in Fig. 4.1(a) would correspond to the hyperfine ground states $F = 1, m_F = 0$ and $F = 2, m_F = 0$, respectively. The Raman transitions occur via the excited states $F' = 1, m_{F'} = 1$ and $F' = 2, m_{F'} = 1$. The resulting four level system can be reduced to a two level system in the same way as that for the Λ system by adiabatically eliminating the excited states together. The resulting system has a coupling rate that is the sum of the two Raman Rabi frequencies. The laser intensities are adjusted to ensure that the light shifts of $|g\rangle$ and $|e\rangle$ are matched.

At the end of the $\pi/2 - \pi - \pi/2$ sequence, a probe beam is applied to measure the amplitude of one of the collective states, via the method of zero photon detection. To explain this, we revert to the three-level model of the atom, and first consider a situation where the atomic ensemble is contained in a single mode cavity with volume mode V,

cavity decay rate γ_c, resonant at ω_1. The cavity is coupled to the transition $|a\rangle \rightarrow |g\rangle$ with coupling rate $g_c = |e.\langle r\rangle|E/\hbar$, where $|e.\langle r\rangle|$ is the dipole moment of the atom and $E = \sqrt{2\hbar\omega_1/\epsilon_0 V}$. If an off-resonant classical laser pulse of frequency ω_2 is applied, the cavity causes Raman transitions to occur between the collective states $|E_n\rangle$ and $|E_{n-1}\rangle$ with the coupling rates $\Omega'_n = \sqrt{N-n+1}\sqrt{n}\Omega'$, where $\Omega' = \Omega_2 g_c/2\Delta$. This is illustrated in Fig. 4.11(a).

In the bad cavity limit ($\gamma_c \gg \sqrt{N}\Omega'$), the Raman transitions will still occur. However, the system will not reabsorb the emitted photon, i.e. the transition from $|E_n\rangle$ to $|E_{n-1}\rangle$ will occur, but not vice versa. The field of such a photon is $E = \sqrt{2\hbar\omega_1/\epsilon_0 \mathscr{A} cT}$, where $\mathscr{A}$ is the cross-sectional area of the ensemble and T the interaction time [**47**]. This limit applies here since there is no cavity, so that the stimulated Raman scattering is an irreversible process that can be modeled as a decay with an effective decay rate that is unique to each $|E_n\rangle$. The decay rate from $|E_N\rangle$ is $\gamma_N = 4NL|g_c\Omega_2|^2/\Delta^2 c = N\gamma_{sa}$, where $\gamma_{sa} = 16L\Omega'^2/c$ [**48**], and that for $|E_n\rangle$ is $\gamma_n = n(N+1-n)\gamma_{sa}$.

The read beam is extracted from the source and is passed through a $99:1$ (R/T: the ratio of the intensity reflectivity, R to the intensity transmittivity, T) non-polarizing beam splitter, $B1$ before hitting the ensemble. The probability of counter-propagating photons emitted from this interaction is determined by the resonant optical density of the ensemble. The direction of signal emission and the role of optical density are discussed further in Sec. 4.4.1. The emitted photons pass through $B1$ and, subsequently, through a half-wave plate. The emitted photons and the probe beam are recombined by another $99:1$ beam splitter, $B2$ and sent to a high speed detector, which generates a DC voltage along with a signal at the beat frequency ~ 6.834 GHz with an unknown phase. This signal

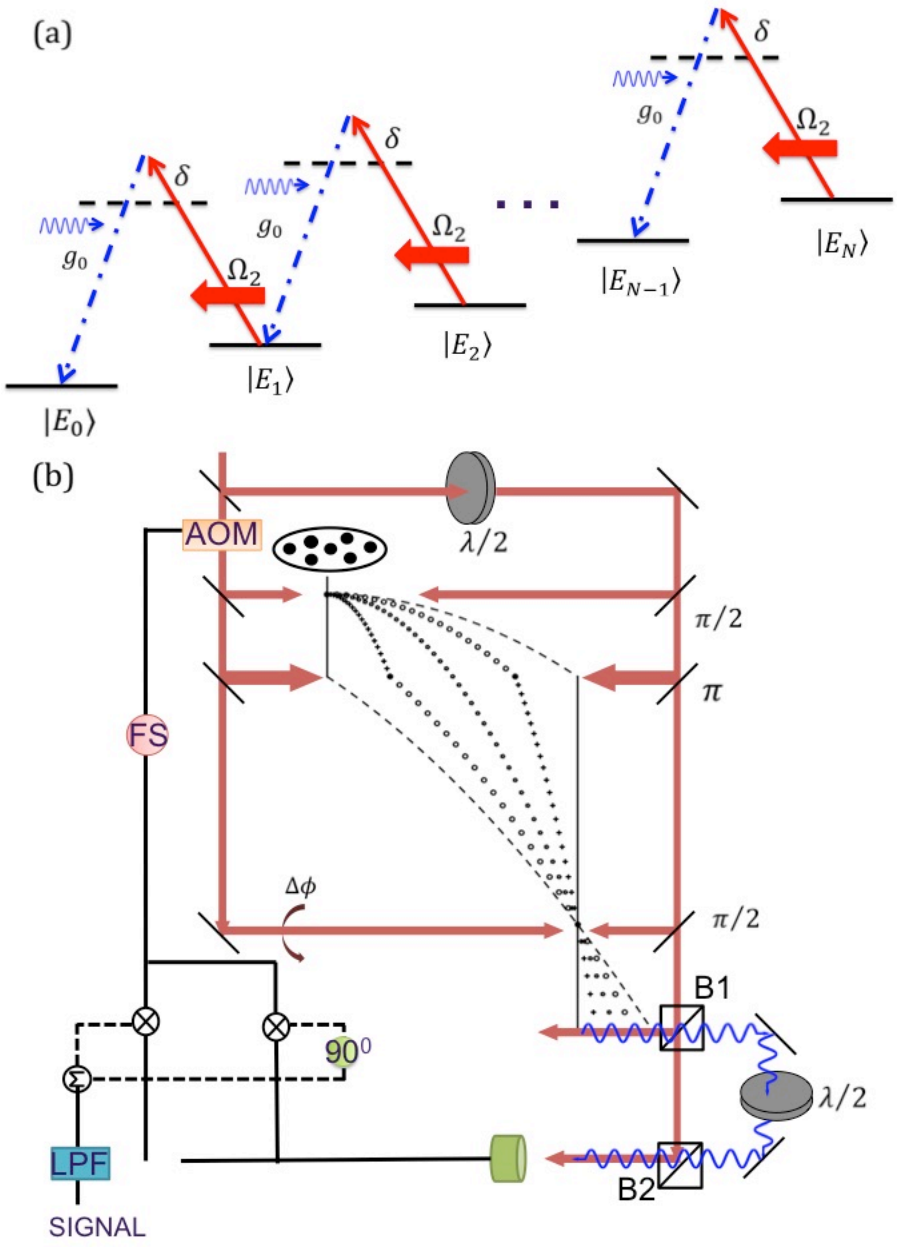

Figure 4.11. (Color online) (a) Interaction between the collective states in the bad cavity limit. (b) Atomic Interferometer experiment for an ensemble of Λ-type atoms for detecting state $|E_0\rangle$.

is bifurcated and one part is multiplied by the FS signal, while the other is multiplied by the FS signal phase shifted by 90°. The signals are then squared before being combined and sent through a low pass filter (LPF) to derive the DC voltage. This DC voltage is proportional to the number of scattered photons. A lower limit is set for the voltage reading and any values recorded above it will indicate the presence of emitted photons. The duration of the probe beam is set at $\gamma_N T = 10$, where $\gamma_N = N\gamma_{sa}$ is the slowest decay rate, to ensure that even the longest lived state is allowed to decay almost completely. If no photon is emitted, the voltage will read below the limit, indicating that the ensemble is in state $|E_0\rangle$. If the ensemble is in any other collective state, at least one photon will be emitted. This process is repeated $\mathscr{M}$ times for a given value of ϕ. The fraction of events where no photons are detected will correspond to the signal for this value of ϕ. This process is then repeated for several values of ϕ, producing the signal fringe for a COSAIN. The experimental scheme is illustrated in Fig. 4.11(b).

4.4.1. Role of Optical Density

In this paper, we have assumed that the ensemble is cigar shaped. This particular choice of configuration is made to achieve the optimum optical density required for realizing the detection scheme discussed above. Consider a four-wave mixing process where three laser beams with wavevectors $\vec{k_1}, \vec{k_2}$, and $\vec{k_3}$ interact with a non-linear medium. The process can be viewed as the scattering of the $\vec{k_3}$ beam, for example, off the grating formed by the interference between the $\vec{k_1}$ and $\vec{k_2}$ beams. Efficient phase matching (which is akin to Bragg matching) then requires that the generated beam with a wavevector $\vec{k_4}$ will satisfy the condition that $\vec{k_1} + \vec{k_2} = \vec{k_3} + \vec{k_4}$. The detection process for the COSAIN can be viewed

as a time-delayed four wave mixing process. The coherence induced in the ensemble has a spatial variation (i.e. a phase grating) proportional to $\exp(i(\vec{k_1} + \vec{k_2}))$. In the detection zone, we apply a readout field with a wavevector $\vec{k_3} = \vec{k_2}$. Thus, the scattering field will have a wavevector $\vec{k_4} = \vec{k_1}$. This implied that the photon would be scattered in the direction opposite to that of the probe.

In such a scattering process the fraction of photon that would be scattered in directions other than the direction dictated by exact phase matching is determined by the resonant optical density of the ensemble, which is given by $\rho = \sigma n \xi_L$ [**47**]. Here, $\sigma \simeq (\lambda/2)^2$ is the resonant scattering cross-section, n is the density, and ξ_L is the interaction length. The fraction of the signal captured by the detector would then be $(\rho - 1)/\rho$. This effect can be incorporated in the detector quantum efficiency by writing it as $\eta = \eta_0(\rho - 1)\rho$, where η_0 is the ideal quantum efficiency of the detector.

The proposed detection scheme demands that $\rho \geq 75$, so that at least 98% of the emitted photons are captured, assuming an ideal detector. As discussed in Sec. 4.3.1, the signal amplitude falls exponentially with increasing ensemble temperature, and N. However, the ensemble must not reach the vicinity of critical density at low temperatures. Considering these factors, we choose $N = 2.6 \times 10^4$, $\xi_L = 1\text{mm}$, and $\xi_T = 10\mu\text{m}$, deriving $\rho = 78.45$ for the $D1$ manifold of ^{87}Rb.

4.5. Alternate Experimental Scheme

The limitation on cooling the ensemble to reduce the effects of Doppler shift restricts the number of atoms. In turn, this restricts the optical density that can be achieved for an ensemble undergoing the COSAIN sequence. Here, we discuss an alternate experimental

scheme that raises the effective optical density of the ensemble. In this scheme, each atom is modeled as a four-level system, as shown in Fig 4.12(a). The metastable states, $|g\rangle$, and $|e\rangle$, are coupled via two intermediate states, $|a\rangle$, and $|b\rangle$. This four-level system can be reduced to an effective three-level system in the Λ-configuration. Each Raman pulse will consist of a pair of an s-polarized and a p-polarized beams, applied in counterpropagating directions. We assume that the s-polarized beam is moving in the $+\mathbf{z}$-direction, and thus, can be represented as $\mathbf{E}_s = (\hat{\sigma}^+\tilde{E_{s0}} + \hat{\sigma}^-\tilde{E_{s0}})\cos(\omega_s t - k_s z) = \hat{\mathbf{s}}E_{s0}\cos(\omega_s t - k_s z)$. Similarly, the p-polarized beam is moving in the $-\mathbf{z}$-direction, and thus, can be represented as $\mathbf{E}_p = (\hat{\sigma}^+\tilde{E_{p0}} - \hat{\sigma}^-\tilde{E_{p0}})\cos(\omega_p t + k_p z) = \hat{\mathbf{p}}E_{p0}\exp(i\pi/2)\cos(\omega_p t - k_p z)$. Here, ω_s and ω_p are the laser frequencies, and E_{s0} and E_{p0} are the amplitudes of the electric field of each laser beam. After making the rotating wave approximation and rotating wave transformation, the atom-laser interaction Hamiltonian elements are $\langle g|\,\vec{\rho}\cdot\hat{\sigma}^+\tilde{E_{s0}}\,|a\rangle$, $\langle g|\,\vec{\rho}\cdot\hat{\sigma}^-\tilde{E_{s0}}\,|b\rangle$, $\langle e|\,\vec{\rho}\cdot\hat{\sigma}^+\tilde{E_{p0}}\,|a\rangle$, $\langle e|\,-\vec{\rho}\cdot\hat{\sigma}^-\tilde{E_{p0}}\,|b\rangle$, and the corresponding complex conjugates. Here $\vec{\rho} = x\hat{\mathbf{x}} + y\hat{\mathbf{y}} + z\hat{\mathbf{z}} = \rho_{\sigma^+}\hat{\sigma^+} + \rho_{\sigma^-}\hat{\sigma^-} + z\hat{\mathbf{z}}$. The Hamiltonian can be further simplified to $H = \rho_{ga}\tilde{E}_{s0}\,|g\rangle\langle a| + \rho_{gb}\tilde{E}_{s0}\,|g\rangle\langle b| + \rho_{ea}\tilde{E}_{p0}\,|e\rangle\langle a| - \rho_{eb}\tilde{E}_{p0}\,|e\rangle\langle b| + c.c.$

For concreteness, we use the $D1$ line of ^{87}Rb to illustrate the mechanism behind this scheme. Thus, the states $|g\rangle$ and $|e\rangle$ in the left part of Fig. 4.12(a) would correspond to the hyperfine ground states $F = 1, m_F = 0$ and $F = 2, m_F = 0$, respectively. The Raman transitions occur via the excited states $|a \equiv F' = 1, m_{F'} = -1\rangle$ and $|b \equiv F' = 1, m_{F'} = 1\rangle$. For this particular choice of levels, $\rho_{ga} = -\rho_{gb} = \rho_{ea} = \rho_{eb} = |\rho_0|$, $|\rho_0\tilde{E_{s0}}| = \hbar\Omega_g/2$, and $|\rho_0\tilde{E_{p0}}| = \hbar\Omega_e/2$. The atom-laser interaction Hamiltonian in this case is, therefore, $H = \hbar(\Omega_g\,|g\rangle\langle a| - \Omega_g\,|g\rangle\langle b| + \Omega_e\,|e\rangle\langle a| - \Omega_e\,|e\rangle\langle b|)/2 + c.c.$ This four level system can be reduced to an equivalent three-level model by rotating the $\{|a\rangle, |b\rangle\}$ Hilbert sub-space by

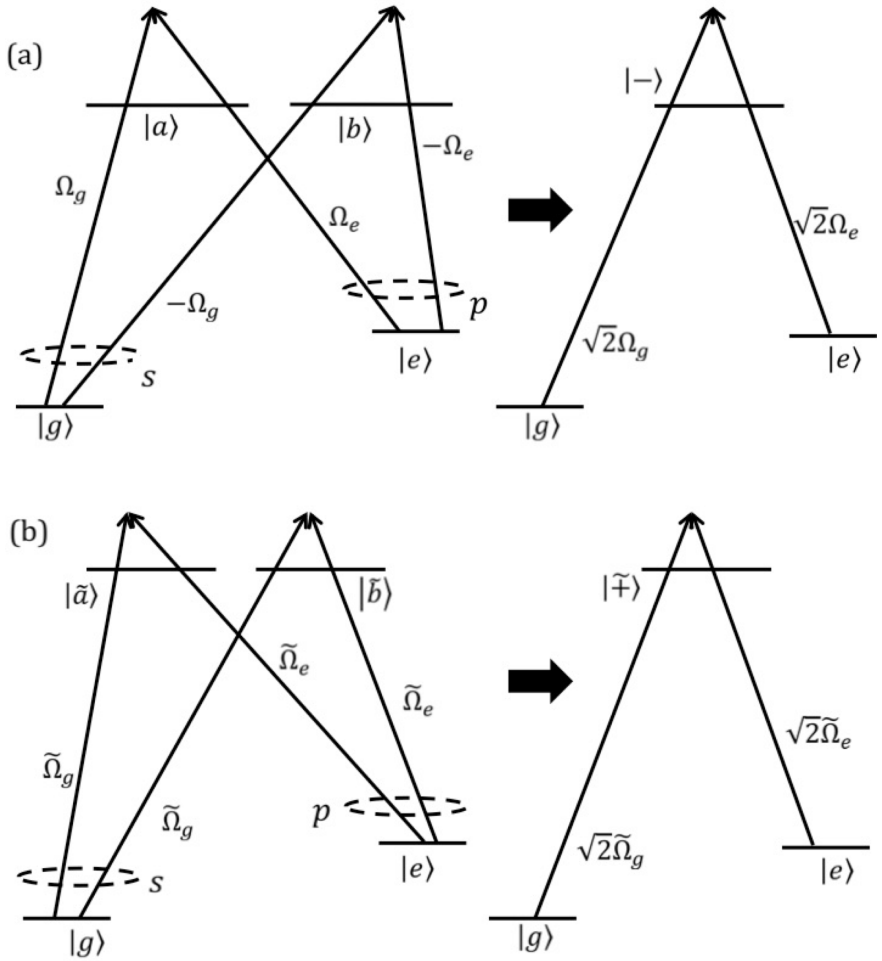

Figure 4.12. (a) Raman transitions between $|g \equiv F = 1, m_F = 0\rangle$ and $|e \equiv F = 2, m_F = 0\rangle$ via $|a \equiv F' = 1, m_{F'} = -1\rangle$ and $|b \equiv F' = 1, m_{F'} = 1\rangle$, (b) Raman transitions between $|g \equiv F = 1, m_F = 0\rangle$ and $|e \equiv F = 2, m_F = 0\rangle$ via $|\tilde{a} \equiv F' = 2, m_{F'} = -1\rangle$ and $|\tilde{b} \equiv F' = 2, m_{F'} = 1\rangle$.

$\pi/4$. The reduced Hamiltonian, H_{red} is given by $H_{red} = \hbar(\Omega_g |g\rangle \langle -| + \Omega_e |e\rangle \langle -|)/\sqrt{2} + c.c.$, where $|-\rangle = (|a\rangle - |b\rangle)/\sqrt{2}$, as illustrated in the right part of Fig. 4.12(a). The $D1$ line of ^{87}Rb are also coupled via $|\tilde{a} \equiv F' = 2, m_{F'} = -1\rangle$ and $|\tilde{b} \equiv F' = 2, m_{F'} = 1\rangle$. In this case, $-\rho_{g\tilde{a}} = -\rho_{g\tilde{b}} = -\rho_{e\tilde{a}} = \rho_{e\tilde{b}} = |\tilde{\rho}_0|$, $|\tilde{\rho}_0 \tilde{E}_{s0}| = \hbar\tilde{\Omega}_g/2$, and $|\tilde{\rho}_0 \tilde{E}_{p0}| = \hbar\tilde{\Omega}_e/2$. Thus, the Hamiltonian is $\tilde{H} = -\hbar(\tilde{\Omega}_g |g\rangle \langle \tilde{a}| + \tilde{\Omega}_g |g\rangle \langle \tilde{b}| + \tilde{\Omega}_e |e\rangle \langle \tilde{a}| + \tilde{\Omega}_e |e\rangle \langle \tilde{b}|)/2 + c.c.$ The

reduced equivalent three-level Hamiltonian is $\tilde{H}_{red} = \hbar(\tilde{\Omega}_g |g\rangle \langle\tilde{+}| + \tilde{\Omega}_e |e\rangle \langle\tilde{+}|)/\sqrt{2} + c.c.$, where $|\tilde{+}\rangle = (|\tilde{a}\rangle + |\tilde{b}\rangle)/\sqrt{2}$. These transitions are shown in the Fig. 4.12(b). Thus, the system is equivalent to two Λ-systems, each with a different common mode detuning. Adiabatic elimination of the $|-\rangle$ and the $|\tilde{+}\rangle$ states would produce the effective two level transition between $|g\rangle$ and $|e\rangle$, just as in the case of excitations with circularly polarized fields described earlier.

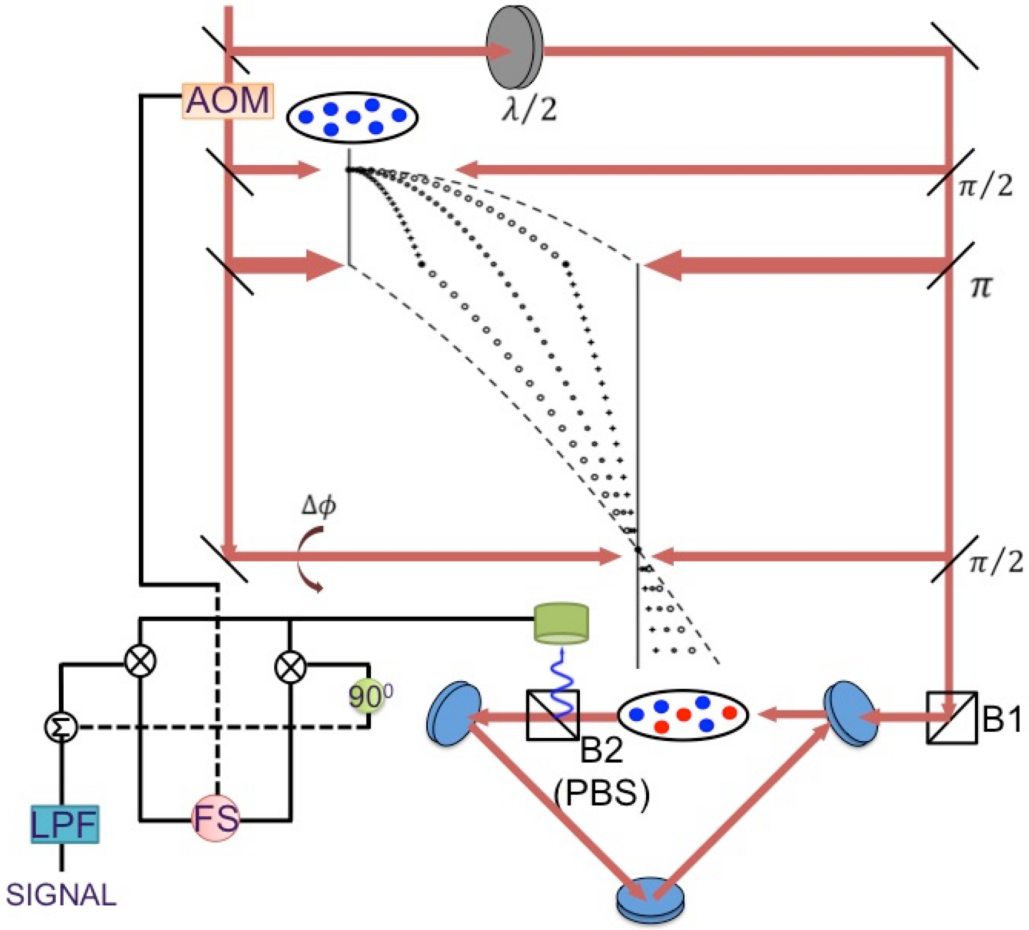

Figure 4.13. Alternate experimental scheme to increase the resonant optical density of the ensemble by introducing a ring cavity in the detection zone.

At the end of the $\pi/2$-dark-π-dark-$\pi/2$ sequence, the ensemble is introduced into a ring cavity of finesse $\mathscr{F}$. The read beam is extracted from the p-polarized beam and enters the cavity through port $P1$, as illustrated in Fig. 4.13. The scattered photons, which will be s-polarized, are extracted with a polarizing beam splitter, B2. Note that this type of extraction is not possible if the interferometer were to be realized with circularly polarized beams. The repeated interaction of the ensemble with the read beam increases the effective resonant optical density of the ensemble to $\mathscr{F}\rho/\pi$. Since the ensemble is falling under gravity through the course of the experiment, the cavity mode size must be reasonably large to accommodate this motion. We assume that the length of the first dark zone is 1cm, and that the distance between the last $\pi/2$ pulse and the read beam is also 1cm. The duration of the read beam, T is set at $\gamma_N T = 10$, where $\gamma_N = N\gamma_{sa}$ is the slowest decay rate, to ensure that even the longest lived state is allowed to decay completely. It can be shown that for $N = 2.6 \times 10^4$, $T \simeq 3.3$ms, so that the distance traveled by the ensemble during the interrogation period is $\simeq 3.3$mm. The cavity mode size must be at least twice as much as this distance.

4.6. Performance of the COSAIN Compared to that of the CRAIN

In order to compare the performance of the COSAIN to that of the CRAIN, we analyze the stability of the phase-difference measured by them by investigating the fluctuation that has both quantum mechanical and classical components, i.e. $\phi|_{total} = (\Delta S_{QM} + \Delta S_{classical})/|\partial S/\partial\phi|$, where $S(\phi)$ is the signal. Since the signal depends on the phase, the fluctuation is not necessarily constant. Therefore, there is no unique value of signal to noise ratio (SNR) to compare unless the COSAIN and the CRAIN are compared at a

particular value of the phase-difference. Thus, the fluctuations must be compared as a function of ϕ. In Sec. 4.6.1, we discuss in detail, the quantum fluctuation due to quantum projection noise, $\Delta P = \sqrt{P(1-P)}$ [**49**], where P is the population of the state being measured, and the classical noise in the long term regime. Since the measure of the signal depends on counting zero photon events, the efficiency of the high speed detector affects the signal amplitude and width. In Sec. 4.6.2, we discuss the effect of the detector efficiency on the COSAIN signal. In Sec. 4.6.3, we discuss the collection efficiency of the COSAIN as a measure of its performance as compared to the CRAIN. The CRAIN suffers from imperfect collection efficiency due to the latter's dependence on experimental geometry. On the other hand, the collection efficiency of the COSAIN is close to unity owing to the fact that the fluorescence of photons is collected through coherent Raman scattering. As a result, for the same number of atoms detected per unit time, the COSAIN is expected to outperform the CRAIN by as much as a factor of 10.

4.6.1. Effect of Quantum and Classical Noise

For the COSAIN to be a useful device for practical metrology, it must outperform the CRAIN. To explore this, we compare their stability in the short term and the long term regimes. The stability of an interferometer is determined by the fluctuations in ϕ that has both quantum mechanical and classical components. The phase difference, ϕ (expressed in radians) is proportional to the rate of rotation of the gyroscope, Ω_G (see Sec. 4.2.1). Thus, $\phi = \mu\Omega_G$, where μ depends on the area of the interferometer and mass of the single atom.

In the CRAIN described above, the signal is a measure of the probability of finding the atom in state $|g\rangle$, $P_g = \cos^2(\mu\Omega_G/2)$. The signal is detected by probing the desired state for a duration of time. If $\tilde{N}$ is the number of atoms per unit time and T is the interrogation period, then the net signal is $S_{CRAIN} = \tilde{N}TP_g$. For comparison, we set the number of atoms per trial in the COSAIN, N, multiplied by the number of trials, M, to equal $\tilde{N}T$. Therefore, $S_{CRAIN} = MN\cos^2(\mu\Omega_G/2)$. Since the fluctuation in MN is $\sqrt{MN}$, the quantum mechanical variance of the signal is $\Delta(S_{CRAIN,QM}) = \sqrt{MN}\sin(\mu\Omega_G)/2$, since the projection noise in a single two level atomic system is $\Delta S_{CRAIN} = \sqrt{P_g(1-P_g)}$ [**49**]. In the case where the probability of finding the atom in $|g\rangle$ is 0 or 1, the projection noise vanishes. On the other hand, the projection noise is at its peak value when $P_g = 1/2$. The slope of the signal is, therefore, $\partial S_{CRAIN}/\partial\Omega_G = -MN\sin(\mu\Omega_G)/(2\gamma_{sa})$, where $\gamma_{sa} = 1/2\mu$ is the linewidth. Assuming ideal quantum efficiency of the detection process, the fluctuation in the rate of rotation can be written as $\delta\Omega_G|_{total} = |(\Delta S_{QM} + \Delta S_{classical})/(\partial S_{CRAIN}/\partial\Omega_G)|$, which maybe be considered as noise (ΔS), over the Rotational Variation of Signal (RVS) which is $(\partial S_{CRAIN}/\partial\Omega_G)$. In the following text, we consider first the effect of quantum noise. The quantum rotation-rate fluctuation (QRF) for a CRAIN maybe written as

$$\delta\Omega_G|_{QM,CRAIN} = \left|\frac{\Delta S_{QM}}{(\partial S_{CRAIN}/\partial\Omega_G)}\right| = \frac{\gamma_{sa}}{\sqrt{MN}}. \tag{4.15}$$

It is, thus, merely a coincidence that the QRF turns out to be constant in a CRAIN. Contrary to popular perception, the QRF of an interferometer is, therefore, not fundamentally the linewidth divided by the SNR. It should be evident from the above discussion that

the signal is not given by MN, and the noise is not given by $\sqrt{MN}$. Instead, they both depend on Ω_G.

In devices where the QRF is not a constant, as we will show for a COSAIN, it is thus, imperative that we carry out an analysis of the QRF in a manner analogous to the analysis for the CRAIN shown above. Thus, we will adopt the approach that the net rotation-rate fluctuation, $\delta\Omega_G$ should be thought of as the ratio of the noise to the RVS. This approach should be adopted universally for all metrological devices. Of course, for devices where the relevant quantity is not the rotation rate, the definition should be adapted accordingly. For example, in a clock that measures frequency, the relevant quantity can be expressed as follows: net frequency fluctuation is the ratio of the noise to the Spectral Variation of Signal (SVS).

Following this approach, we calculate the net rotation-rate fluctuation of the COSAIN and compare it to that of the CRAIN. We will first calculate the quantum fluctuation which is relevant in the short term regime, and then the classical fluctuation, which dominates in the long term regime. The signal of a COSAIN for M trials is $S_{COSAIN} = MP_{E0} = M\cos^{2N}(\mu\Omega_G/2)$, and the projection noise is $\Delta P_{E0} = \sqrt{P_{E0}(1-P_{E0})}$ for a single trial, so that $\Delta P_{E0} = \sqrt{M}\sqrt{P_{E0}(1-P_{E0})}$ for M trials. Thus, the total quantum mechanical noise in the signal is

$$\Delta P_{E0} = \sqrt{M}\cos^{N}(\mu\Omega_G/2)\sqrt{1-\cos^{2N}(\mu\Omega_G/2)}, \tag{4.16}$$

and the RVS is

$$\partial S_{COSAIN}/\partial\Omega_G = -MN\cos^{2N-1}(\mu\Omega_G/2)$$

$$\times \sin(\mu\Omega_G/2)/\gamma_{sa}. \tag{4.17}$$

Therefore, the QRF in the COSAIN is given by

$$\delta\Omega_{G(QM,COSAIN)} = \frac{\gamma_{sa}}{N\sqrt{M}}\frac{\sqrt{\sec^{2N}(\mu\Omega_G/2)-1}}{\tan(\mu\Omega_G/2)}. \tag{4.18}$$

Thus, unlike the CRAIN, the phase fluctuation in a COSAIN is not constant and depends on Ω_G and thus, on ϕ. We consider first the limiting case of $\Omega_G \to 0$. Using Taylor expansion, it is evident that $\delta\Omega_{G(QM,COSAIN)} = \gamma_{sa}/\sqrt{MN}$, which is the same as that of a CRAIN. This can be understood physically by noting that while the fringe width becomes much narrower for the COSAIN, the SNR also decreases due to the fact that a single observation is made for all N atoms in a given trial. The QRF for the COSAIN, given in Eq. 4.18, is smallest as $\Omega_G \to 0$ and increases as Ω_G moves away from zero. The ratio of the QRF for the CRAIN to that of the COSAIN is plotted as a function of Ω_G in the left side of Fig. 4.14 for $M = 1000$ and $N = 10^4$. Here, the vertical bars indicate the FWHM of the COSAIN signal. It is clear from this plot that the QRF for the COSAIN increases significantly as we move away from resonance. However, since a servo will keep the value of Ω_G confined to be close to zero, the phase stability of the COSAIN, under quantum noise limited operation, should be very close to that of the CRAIN, assuming that all the other factors remain the same.

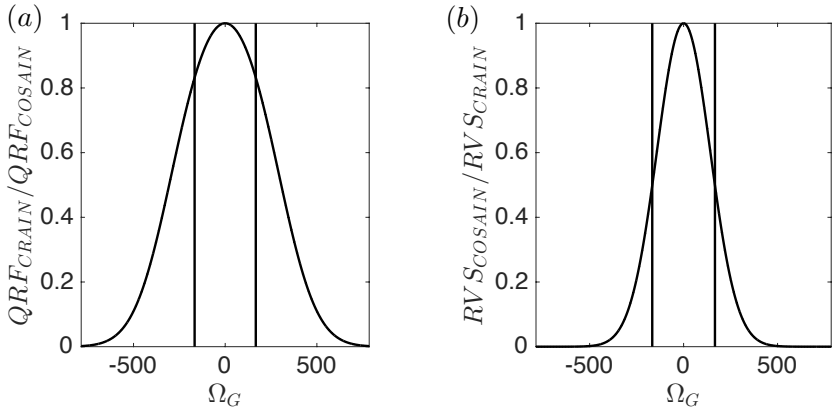

Figure 4.14. (left) Ratio of the QRF in the CRAIN to the QRF in the COSAIN, for $M = 1000$ and $N = 10^4$. It should be noted that the fluctuation in the CRAIN is independent of Ω_G while that of the COSAIN varies significantly with it. (right) Ratio of the RVS of the COSAIN to the RVS of the CRAIN for $M = 1000$ and $N = 10^4$. The vertical lines in the plots show where the FWHM of S_{CRAIN} are.

The classical rotation-rate fluctuation (CRF), $\delta\Omega_G|_{classical} = \Delta S_{classical}/(\partial S/\partial\Omega_G)$, is the limiting factor in the long term stability. While the quantum fluctuation is dominated by quantum projection noise, the classical noise is dominated by noise in the electronic and the mechanical components employed to generate the interferometer signal. Since the pieces of equipment used in the development of both the COSAIN and CRAIN suffer from similar noise issues, the variance ΔS is expected to be of the same order of magnitude for both interferometers. On the other hand, the RVS, $(\partial S/\partial\Omega_G)$, is not the same, as was shown previously. The ratio of the RVS of the COSAIN to the RVS of the CRAIN is

$$\frac{\partial S_{COSAIN}/\partial\Omega_G}{\partial S_{CRAIN}/\partial\Omega_G} = \frac{cos^{2N}(\mu\Omega_G/2)}{cos^2(\mu\Omega_G/2)} = \frac{P_{E0}}{P_g}, \tag{4.19}$$

and is plotted in Fig. 4.8(right). With $\Delta S_{classical,COSAIN} \sim \Delta S_{classical,CRAIN}$, the ratio of the CRF of the COSAIN to that of the CRAIN can be written as

$$\frac{\delta\Omega_{G(classical,COSAIN)}}{\delta\Omega_{G(classical,CRAIN)}} \simeq \frac{\cos^2(\mu\Omega_G/2)}{\cos^{2N}(\mu\Omega_G/2)}. \tag{4.20}$$

Similar to the ratio of the two interferometers in QRF, Eq. 4.20 is smallest as $\phi \to 0$ and increases as ϕ moves away from resonance. Thus, with respect to both quantum and classical sources of noise, the COSAIN must be operated near $\phi \simeq 0$ for optimal performance.

4.6.2. Effect of Detector Efficiency

The key aspect of the COSAIN is the measurement of the amplitude of $|E_0\rangle$, which indicates that each of the atoms in the ensemble is individually in $|g\rangle$. The probe beam is applied to the ensemble, which is in the quantum state $|\Psi\rangle = c_0 |E_0\rangle + \sum_{n=1}^{N} |E_n\rangle$. Interaction between the probe beam, the ensemble, and the free space vacuum modes on the other leg would lead to production of photons unless $c_0 = 1$, and $c_n = 0$ for all n. These photons are detected using a heterodyning technique, as described in Sec 4.2. The voltage output of the heterodyning system is proportional to the amplitude of the electric field corresponding to the photons.

In general, one or more photons are produced as $|E_n\rangle$ decays to $|E_{n-1}\rangle$ and subsequent states. The time needed for these photons to be produced depends in the vacuum and probe field induced Raman transition rates between $|E_n\rangle$ and $|E_{n-1}\rangle$. If we assume perfect efficiency for detecting each of these photons, and wait for a time long compared to the inverse of the weakest of these transition rates, then the detection of no photons implies

that the system is in state $|E_0\rangle$. In practical experimental conditions, we can choose a small threshold voltage at the output of the heterodyning system as an indicator of null detection. Thus, any signal below this threshold would be viewed as detection of the quantum system in the $|E_0\rangle$ state, and all signals above this threshold would be discarded. The number of events below this threshold for $\mathscr{M}$ trials carried out with all the parameters of the experiment unchanged, is the derived signal for the COSAIN. After collecting data for all the values of ϕ that is of interest, the result would ideally yield the plot of the COSAIN signal $S_{COSAIN} = |c_0|^2$, averaged over $\mathscr{M}$ trials. However, with a fractional detector efficiency and finite detection period, the signal would deviate from the ideal result.

Consider first the effect of the detection period. Given the decay rate of the off-resonant Raman process, $\gamma_n = n(N+1-n)\gamma_{sa}$, the probability that $|E_n\rangle$ will produce zero photons during the measurement period T is $P_{0,n} = e^{-\gamma_n T}$. Thus, the total probability of zero photon emission (which should vanish ideally for any $c_n \neq 0$) is given by $P_0 = \sum_{n=1}^{N} |c_n|^2 e^{-\gamma_n T}$. The COSAIN signal, S_{COSAIN}, is the total probability of finding zero photons during T, and can be expressed as $S_{COSAIN} = |c_0|^2 + \sum_{n=1}^{N} |c_n|^2 e^{-\gamma_n T}$. Noting that $\gamma_0 = 0$, we can rewrite this as $S_{COSAIN} = \sum_{n=0}^{N} |c_n|^2 e^{-\gamma_n T}$. The lower and upper bounds of S_{COSAIN} can be established by considering the strongest and the weakest effective decay rates. The strongest decay rate occurs for the middle state, $\gamma_{N/2} = (N/2)(N/2+1)\gamma_{sa} \approx (N^2/4)\gamma_{sa}$, where $N \gg 1$ approximation has been made. With the substitution of the largest decay rate for each $|E_n\rangle$ into the equation for S_{COSAIN}, the lower bound is set by

$$P_L = |c_0|^2 + (1 - |c_0|^2)\exp(-N^2\gamma_{sa}T/4). \tag{4.21}$$

On the other hand, the weakest decay rate is exhibited when $n = N$, making the upper bound on the signal,

$$P_U = |c_0|^2 + (1 - |c_0|^2) \exp(-N\gamma_{sa}T). \tag{4.22}$$

The signal of the COSAIN, S_{COSAIN} produced in time T will lie somewhere between P_L and P_U.

Consider next the effect of the non-ideal detection efficiency of the heterodyning scheme. For concreteness, we define η as the efficiency of detecting a single photon. In practice, this parameter will depend on a combination of factors, including the quantum efficiency of the high-speed photon detector and the overlap between the probe laser mode and the mode of the emitted photon. For the present experiment, we are only interested in knowing whether at least one photon is detected, and not in the actual number of photons. When more photons are emitted, the detector will have a better chance of observing a non-zero signal, and hence distinguish dark counts from the rest with more certainty. For example, if three photons are emitted in time T, then four different outcomes are possible:

- All three photons are detected, with probability η^3;
- Two of the photons are detected with probability $\eta^2(1 - \eta)$; this can occur for any two of the photons, so the multiplicity is 3;
- One photon is detected, with probability $\eta(1 - \eta)^2$ and multiplicity of 3;
- No photons are detected, with probability $\epsilon^3 \equiv (1 - \eta)^3$.

The sum of these probabilities is 1. The probability that at least 1 photon is detected is thus $(1-\epsilon^3)$. For any state $n \neq 0$, the probability of detecting at least 1 photon is, therefore, $(1-\epsilon^n)$.

Moreover, we must also consider how the effective detection efficiency is influenced by the fact that the collective states decay at different rates. Specifically, the n level for $n > 0$ might produce $N-n$ photons, $N-n-1$ photons, down to zero photons, depending on the length of the measurement time and the effective decay rate. If the system is in $|E_3\rangle$, for example, it can produce up to 3 photons but with probabilities that change over T. For a given time T, $|E_3\rangle$ evolves into a sum of the states $|E_3\rangle \rightarrow \sum_{k=0}^{3} a_{n,k}(T)\,|E_k\rangle$, where the coefficient $a_{n,k}(T)$ depends on the effective decay rate that is specific to each state, and changes as the states evolve in time. Thus the probability of detecting at least one photon is

$$P = \sum_{n=1}^{N-1} |c_n|^2 \sum_{k=n}^{N} (1-\epsilon^{k-n}) |a_{n,k}(T)|^2. \tag{4.23}$$

Therefore, the probability of detecting no photon is

$$\begin{aligned} S_{COSAIN} = 1 - P = 1 &- \sum_{n=1}^{N-1} |c_n|^2 \\ &\times \sum_{k=n}^{N} (1-\epsilon^{k-n}) |a_{n,k}(T)|^2. \end{aligned} \tag{4.24}$$

The numerical analysis for a large number of atoms is tedious and scales as at least $(N-1)!$ for the COSAIN. However, we can take the worst case scenario to serve as the upper bound for the signal. The worst case occurs when only a single photon is produced as a result of $|E_n\rangle$ decaying to only the $|E_{n-1}\rangle$ state, so that the index of the second

summation stops at $k = n - 1$. In this case, we can write $|a_{n,n-1}(T)| = (1 - e^{-\gamma_n T})$ and the signal becomes

$$S_{COSAIN} = |c_0|^2 + \epsilon(1 - |c_0|^2) + \eta \sum_{n=1}^{N} |c_n|^2 e^{-\gamma_n T}. \tag{4.25}$$

Using the approach we employed in arriving at Eq. 4.21 and Eq. 4.22, we now consider the strongest and the weakest decay rates for single photon production to arrive at the lower and upper bounds of the zero photon count signal:

$$P_L = 1 - \eta(1 - |c_0|^2)(1 - e^{-N^2 \gamma_{sa} T/4}), \tag{4.26}$$

$$P_U = 1 - \eta(1 - |c_0|^2)(1 - e^{-N \gamma_{sa} T}). \tag{4.27}$$

Figure 4.15 shows the plot of the ideal S_{COSAIN}, P_L and P_U over a variation in ϕ for different values of detector efficiencies and detection times for $N = 10,000$. It can be seen from the plots that the upper and lower bounds on the signal coincide with the ideal signal in the vicinity of $\phi \to 0$. For a larger size of the ensemble, a longer detection time ensures that the gap between the bounds decreases and that they are closer to the ideal signal.

If we set $\gamma_{sa} T = 1$, the signal depends on η as

$$S_{COSAIN} \simeq 1 - \eta(1 - \cos^{2N}(\phi/2)) \tag{4.28}$$

for large N and $\mathscr{M} = 1$. Hence, we can calculate the QRF for the COSAIN to see how it depends on the detector efficiency, and how it compares to the CRAIN. For

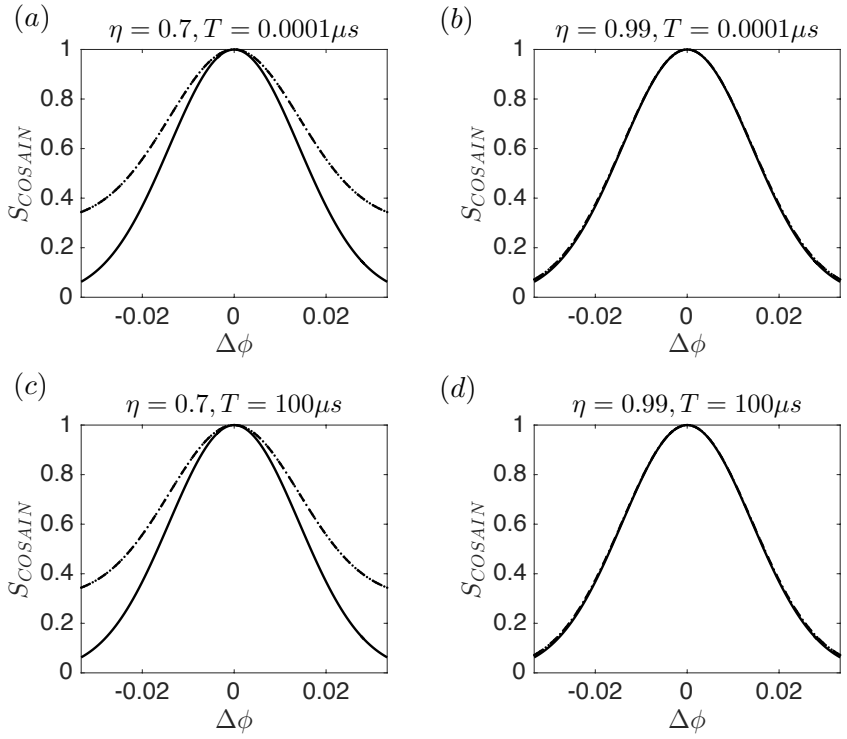

Figure 4.15. Plot of ideal signal (solid line), the upper bound (broken line), the lower bound (dotted line) for different detection times, T and detector efficiencies, η for $N = 10,000$.

the CRAIN, it is straightforward to show that with $S_{CRAIN} = \eta N \cos^2(\phi/2)$, the quantum mechanical noise in the signal is $\Delta S_{CRAIN} = \sqrt{\eta N}\cos(\phi/2)\sin(\phi/2)$ and the RVS is $|\partial S_{CRAIN}/\partial\Omega_G| = (\eta N/\gamma_{sa})\cos(\phi/2)\sin(\phi/2)$, so that the QRF is $\delta\Omega_{G(QM,CRAIN)} = \gamma_{sa}/\sqrt{\eta N}$. It is also straightforward to calculate the QRF of the COSAIN. the total quantum mechanical noise in the COSAIN signal in Eq. 4.28 is:

$$\Delta S_{QM,COSAIN} = \eta \cos^N(\phi/2)\sqrt{1 - \cos^{2N}(\phi/2)}, \tag{4.29}$$

and the RVS is

$$\partial S_{COSAIN}/\partial\Omega_G = -(\eta N/\gamma_{sa})\sin(\phi/2)\cos^{2N-1}(\phi/2). \tag{4.30}$$

Thus, the QRF of the COSAIN is

$$\delta\Omega_{G(QM,COSAIN)} = \left|\frac{\gamma_{sa}}{N\sqrt{\eta}}\frac{\sqrt{1-\cos^{2N}(\mu\Omega_G/2)}}{\cos^{N-1}(\mu\Omega_G/2)\sin(\mu\Omega_G/2)}\right| \tag{4.31}$$

which approaches $\gamma_{sa}/\sqrt{\eta N}$ as $\Omega_G \to 0$. Assuming that the detector efficiencies of the COSAIN and the CRAIN can be essentially the same, they do not affect the ratio of the two QRF's.

4.6.3. Effect of Collection Efficiency

We consider next the effect of collection efficiency, β on the COSAIN and compare it to that of the CRAIN. The signal for both the COSAIN and the CRAIN, is directly proportional to β. From Eq. 4.15 and Eq. 4.18, it is easy to show that

$$\begin{aligned}\zeta &\equiv \frac{\delta\Omega_{G(QM,COSAIN)}}{\delta\Omega_{G(QM,CRAIN)}} \\ &= \frac{\sqrt{\sec^{2N}(\frac{\mu\Omega_G}{2})-1}}{\sqrt{N}\tan(\frac{\mu\Omega_G}{2})}\sqrt{\frac{\beta_{CRAIN}}{\beta_{COSAIN}}},\end{aligned} \tag{4.32}$$

where $\beta_{CRAIN}(\beta_{COSAIN})$ is the collection efficiency of the CRAIN (COSAIN).

As $\Omega_G \to 0$, the quantity in the square bracket in Eq. (4.32) approaches unity. Therefore, in this limit, ζ, the ratio of the QRF of the COSAIN to that of the CRAIN, would depend on the ratio of of the collection efficiencies of the detection process. The coherent stimulated Raman scattering based detection method used for the COSAIN process has

a collection efficiency that is close to unity, i.e. $\beta_{COSAIN} \simeq 1$. In the case of the CRAIN, the fluorescence is collected from the spontaneous emission process, which emits photons in a dipolar radiation pattern. The β_{CRAIN} can be quantified by analyzing the detection method, for example, of a CRAIN that makes use of cold atoms released from a MOT. For a lens placed at a distance of $r = 5$ cm, with a diameter of $d = 2.5$ cm, ignoring the dipolar pattern of radiation for simplicity, and assuming it to be uniform in all directions, this system yields a value of $\beta_{CRAIN} \simeq d^2/4r^2 = 1/16$ corresponding to $\zeta \sim 0.25$. In a typical CRAIN, various geometric constraints make it difficult to achieve a value of β_{CRAIN} much larger than this. In practice, in cases where the total volume occupied by the CRAIN has to be constrained in order to meet the user requirements, the value of β_{CRAIN} is typically 1%, which would correspond to $\zeta \sim 0.1$. Thus, the near unity collection efficiency of the COSAIN can lead to an improvement of the interferometer stability by as much as a factor of 10.

Another method of detecting signal in a CRAIN is absorption. However, the use of absorption warrants the consideration of many practical issues. The fluctuation in ϕ is affected by additional noise contributed by the laser used in absorption. Let us assume that the observation time is T, and the number of photon in the probe beam before absorption is N_P, and that the probe is in a Coherent state. Furthermore, we assume that the number of atoms passing through the detection process within this time is N_A, and the linewidth of resonance is Γ. If the detection process produces an absorption by a fraction of κ (i.e. $\kappa = 1$ represents perfect absorption of the laser beam), and the detector

has a quantum efficiency of η, then the resulting fluctuation in ϕ can be expressed as

$$\delta\phi_{abs} = \Gamma\left(\frac{1}{\sqrt{\eta\kappa N_A}} + \frac{1}{\sqrt{\eta\kappa N_P}}\right), \tag{4.33}$$

where, the first term inside the parenthesis represents the quantum projection noise of the atoms, and the second term represents the shot noise of the photons (which can be regarded as the quantum projection noise of photons). The validity of this expression can be easily verified by considering various limits. Consider first the ideal case where $\varepsilon \equiv \eta\kappa = 1$. For $N_P \gg N_A$, the additional noise from the laser can be neglected, and we get the fundamental noise limit due to the quantum projection noise of the atoms. On the other hand, if $N_P \ll N_A$, the quantum projection noise from the atoms can be neglected, and the process is limited by the shot-noise of the laser. In general, the parameter ε represents the overall quantum efficiency of the detection process. The corresponding expression for detection via fluorescence is $\delta\phi_F = \gamma/\sqrt{\eta\rho N_A}$, where ρ is the fraction of fluorescence hitting the detector.

The contribution from the second term in Eq. (4.33) shows that the intensity of the laser beam used in absorption must be made strong enough in order to make the effect of this term negligible compared to the first term. However, since the absorption process is nonlinear and saturates for a strong laser beam, increasing the laser intensity often decreases the effective value of κ. For example, consider an ensemble of 2×10^6 atoms with a linear optical density of 300, which can be realized (as we have shown above) for an ensemble confined to a cigar shaped ensemble. For a weak probe, the value of κ is unity. However, as the probe power is increased, the value of κ decreases dramatically. This can be seen by considering a situation where the value of N_P is 10^9, for example. Since

the atomic transition used for absorption is not closed (i.e., not cyclic), the ensemble can only absorb a number of photons that is of the order of 2×10^6. Thus, the maximum value of κ would be only about 0.002. Furthermore, if the area of the laser beam (πw^2) is much larger than the area of the atomic ensemble ($\pi \xi_T^2$), then the value of κ can never exceed the value of ξ_T^2/w^2 . We are not aware of any publication reporting a cold atom interferometer that makes use of absorption for detecting the atoms, possibly because of these constraints and considerations. Nonetheless, as a matter of principle, an absorption process can certainly be used to reduce the quantum frequency fluctuation below what is observed in fluorescence detection systems, under proper choice of parameters.

4.7. Summary

In this paper, we have described a collective state atomic interferometer (COSAIN) with N non-interacting, independent atoms in an ensemble. We have shown that the signal fringes are narrowed by $\sqrt{N}$ compared to a conventional interferometer, without entanglement. This effect is a result of the interference among collective states, and is a manifestation of interference at a Compton frequency of ten nonillion Hz, or a de Broglie wavelength of 4.5 femtometer, for $N = 10^6$ and $v = 1m/s$. The essence of the COSAIN is the detection of a collective state, rather than individual atomic states. For a suitably chosen collective state, this is accomplished via a null detection scheme, wherein the detection of zero photons corresponds to the system being in this collective state. We have presented a heterodyne detection scheme for measuring this signal. In this scheme, the signal is detected by collecting fluorescence through stimulated Raman scattering of Stokes photons, which are emitted predominantly against the direction of the

probe beam, for a high enough resonant optical density. We have shown that the fringe width reduction occurs due to the interference of the multiple paths among the collective states, and does not violate the fundamental quantum limit. We have also proposed a new excitation scheme, applicable to both a conventional Raman atomic interferometer (CRAIN) as well to the COSAIN, wherein the counter-propagating beams are cross-linearly polarized. For the COSAIN, this scheme enables an enhancement of the effective resonant optical density by placing a cavity around the atoms in the detection zone. We have analyzed in detail the effect of various inhomegeneities, arising from the non-uniformity in experimental parameters, on the COSAIN signal, and used this analysis to identify a suitable choice of parameters for realizing a COSAIN. The performance of the COSAIN has been compared to that of the conventional Raman atomic interferometer (CRAIN) by analyzing quantum and classical fluctuations in frequency. When the effects of detector efficiency and collection efficiency are considered, it can be seen that the COSAIN may perform 10 times better than a CRAIN employing fluorescence detection.

CHAPTER 5

Spin Squeezing: Overview

This chapter presents a review of the concepts of spin squeezing. We lay down the mathematical framework of spin-1/2 systems necessary for understanding atom interferometry with spin ensembles. We establish the notation of the rotation operator, more details of which can be found in [**40**]. The conventional Raman atomic interferometer (CRAIN) is discussed in the light of the rotation operator. The concept of coherent spin states (CSS) is laid out in detail, and its correspondence in the angular momentum space in shown. The projection noise of unentangled atoms in a CSS is derived, yielding the standard quantum limit (SQL). A deliberation on exceeding the SQL with squeezed spin states (SSS) follows. A comprehensive review of the theoretical and experimental advancements in spin squeezing is given in [**50**].

5.1. Spin Representation of Atomic Ensembles

5.1.1. Spin-$\frac{1}{2}$ Systems

Any two-level quantum system, regardless of its physical manifestations, can be modeled as a collection of spin-1/2 particles, with states $\{|\downarrow\rangle, |\uparrow\rangle\}$. This allows for an elegant visualization of experiments that are based on Ramsey spectroscopy. Any operator acting on this system can be expanded in the set of angular momentum operators such that, $j_x = \hbar(|\downarrow\rangle\langle\uparrow| + |\uparrow\rangle\langle\downarrow|)/2$, $j_y = i\hbar(|\downarrow\rangle\langle\uparrow| - |\uparrow\rangle\langle\downarrow|)/2$, $j_z = \hbar(|\uparrow\rangle\langle\uparrow| - |\downarrow\rangle\langle\downarrow|)/2$, and the identity matrix I_2, associated with the atom, where $\hat{\mathbf{j}}_i = \frac{1}{2}(\hat{\sigma}_{xi}, \hat{\sigma}_{yi}, \hat{\sigma}_{zi})$, $\{\hat{\sigma_x}, \hat{\sigma_y}, \hat{\sigma_z}\}$

being Pauli matrices. The spin-up and spin-down operators of this spin-1/2 system are, therefore, given by $j_\pm = (j_x \pm i j_y)$. The states, $|\downarrow\rangle$ and $|\uparrow\rangle$ are eigenstates of the operator j_z. This choice of basis is driven purely by convenience, and is not unique.

In this picture, the Hamiltonian of the interaction of the atom with a semiclassical laser, ignoring the center of mass motion of the atom, is given by

$$H = \Omega j_x + \delta j_z. \tag{5.1}$$

Here, Ω is the Rabi frequency, and δ is the detuning of the atom-laser system. The state of the atom at time t, due to the interaction with the laser is $|\psi(t)\rangle = \exp(-iHt/\hbar)\,|\psi(0)\rangle$. It is assumed that at $t = 0$, the atom is in state $|\downarrow\rangle$. Consider first, the case where $\delta = 0$, so that the state of the atom after a pulse of duration t is

$$|\psi(t)\rangle = \exp(-i\Omega t j_x)\,|\downarrow\rangle\,. \tag{5.2}$$

From the Taylor series expansion of the exponential:

$$\begin{aligned}
|\psi(t)\rangle &= (\cos(\Omega t j_x) - i\sin(\Omega t j_x))\,|\downarrow\rangle \\
&= \left(\left(I_2 - \frac{(\Omega t j_x)^2}{2!} + \frac{(\Omega t j_x)^4}{4!} + \ldots\right) - i\left(j_x - \frac{(\Omega t j_x)^3}{3!} + \frac{(\Omega t j_x)^5}{5!} + \ldots\right)\right)|\downarrow\rangle \\
&= \Big(I_2\Big(1 - \frac{1}{2!}\Big(\frac{\Omega t}{2}\Big)^2 + \frac{1}{4!}\Big(\frac{\Omega t}{2}\Big)^4 + \ldots\Big) \\
&\quad - 2ij_x\Big(1 - \frac{1}{3!}\Big(\frac{\Omega t}{2}\Big)^3 + \frac{1}{5!}\Big(\frac{\Omega t}{2}\Big)^5 + \ldots\Big)\Big)\,|\downarrow\rangle \\
&= \Big(I_2\cos\Big(\frac{\Omega t}{2}\Big) - 2ij_x\sin\Big(\frac{\Omega t}{2}\Big)\Big)\,|\downarrow\rangle \\
&= \cos\left(\frac{\Omega t}{2}\right)|\downarrow\rangle - i\sin\left(\frac{\Omega t}{2}\right)|\uparrow\rangle\,. \qquad (5.3)
\end{aligned}$$

This expression is identical to that derived by substituting $c_g(0) = 1$ and $c_e(0) = 0$ in Eq. 2.20. Thus, the interaction of a spin-1/2 particle with any operator can be visualized as a rotation in the momentum space.

5.1.2. Collective Spins

The discussion in Sec. 5.1.1 can be generalized for an N-particle system where each particle has two states. The collective spin of the ensemble is the sum of the individual spins,

$$\hat{\mathbf{J}} = \sum_{i=1}^{N} \hat{\mathbf{j}}_i. \tag{5.4}$$

The collective atomic population operators for spin up and spin down are $\hat{N}_\downarrow = \sum_i |\downarrow_i\rangle \langle\downarrow_i|$, and $\hat{N}_\uparrow = \sum_i |\uparrow_i\rangle \langle\uparrow_i|$, respectively. Therefore, the population difference between the states can be expressed as

$$\hat{J}_z = \frac{\hat{N}_\uparrow - \hat{N}_\downarrow}{2}, \tag{5.5}$$

where $\hat{J}_z$ is the component of $\hat{\mathbf{J}}$ along the **z**-direction. Thus, unlike $\hat{J}_x$ and $\hat{J}_y$, $\hat{J}_z$ can be easily measured via conventional fluorescence detection techniques.

The collective spin operators are governed by the cyclic commutation relations,

$$[\hat{J}_i, \hat{J}_j] = i\epsilon_{ijk}\hat{J}_k, \tag{5.6}$$

where ϵ_{ijk} is the Levi-Civita symbol. These commutation relations give rise to the Heisenberg uncertainty relation

$$\langle \Delta J_i^2 \rangle \langle \Delta J_j^2 \rangle \geq \frac{1}{4} \left| \langle J_k \rangle \right|^2 , \tag{5.7}$$

where $\Delta J_i^2 = \langle \hat{J}_i^2 \rangle - \langle \hat{J}_i \rangle^2$ is the variance of the measurement of the spin projection J_i for numerous iterations of identical preparations and measurements.

5.1.3. Coherent Spin States

Coherent Spin States (CSS) are the quantum states of a symmetric ensemble of N spin-1/2 particles, with no entanglement or quantum correlation between them. They are formed by placing each particle of the N-particle system in the same quantum state

$$|\theta, \phi\rangle = \prod_{i=1}^{N} \left(\cos \frac{\theta}{2} |\downarrow_i\rangle + \mathrm{e}^{-i\phi} \sin \frac{\theta}{2} |\uparrow_i\rangle \right). \tag{5.8}$$

The angles θ and ϕ describe the direction (θ, ϕ) along which the mean spin vector $\mathbf{J} = \langle \hat{\mathbf{J}} \rangle = \langle \theta, \phi | \, \hat{\mathbf{J}} \, | \theta, \phi \rangle$ is pointed, as illustrated in Fig. 5.1. The tip of the Bloch vector is situated on the surface of the sphere of radius $J = N/2$. The Bloch vector behaves classically if fluctuations in the spin projections are not considered. In the spin representation, the Dicke collective states described in Sec. 3.1 are simply the usual angular momentum states, defined as the eigenstates of $\hat{J}_z = (\hat{J}_+ \hat{J}_- \hat{J}_- \hat{J}_+)/2$. These states are derived as a result of the rotation operator, $R_{\theta,\phi}$ acting on an eigenstate of $\hat{J}_z$. Using the generating functions given in [**40**], the expression for $R_{\theta,\phi}$ is

$$R_{\theta,\phi} = \exp\left(\tau \hat{\mathbf{J}}_+\right) \exp\left(ln(1 + |\tau|^2) \hat{\mathbf{J}}_z\right) \exp\left(-\tau^* \hat{\mathbf{J}}_-\right), \tag{5.9}$$

where $\tau = \exp(-i\phi)\tan(\theta/2)$.

For clarity, we consider an example of the CSS $|\frac{\pi}{2}, \frac{\pi}{2}\rangle = \prod_{i=1}^{N} \left(|\downarrow_i\rangle - i\,|\uparrow_i\rangle\right)/\sqrt{2}$, which corresponds to the state of the ensemble after the first $\pi/2-$pulse in Ramsey spectroscopy, discussed in its manifestation as a CRAIN in Sec. 2.3. Essentially, this state is a result of rotating $|-J\rangle = |0,0\rangle = \prod_{i=1}^{N} |\downarrow_i\rangle$ about the $\hat{\mathbf{x}}$-axis. Substituting $\theta = \pi/2, \phi = \pi/2$ in Eq. 5.9 we get:

$$\begin{aligned} |\frac{\pi}{2}, \frac{\pi}{2}\rangle &= \exp\left(-i\hat{\mathbf{J}}_+\right)\exp\left(ln(2)\hat{\mathbf{J}}_z\right)\exp\left(-i\hat{\mathbf{J}}_-\right)|-J\rangle \\ &= 2^{-J}\sum_{k=0}^{2J}(-i)^k\sqrt{\binom{2J}{k}}\,|-J+k\rangle\,. \end{aligned} \tag{5.10}$$

Each individual spin in the CSS is aligned along the $\hat{\mathbf{y}}$ axis. The mean collective spin that represents this CSS is, therefore, $\mathbf{J} = \frac{N}{2}\hat{\mathbf{y}}$. Due to quantum mechanics, an uncertainty is introduced in the spin projections, governed by the Heisenberg uncertainty relationships given in Eq. 5.7. Therefore, the quantum projection noise in $|\frac{\pi}{2}, \frac{\pi}{2}\rangle$ is $\Delta J_z = \Delta J_x = \sqrt{N}/2$. The quantum fluctuations in a CSS is, therefore, isotropic in the plane orthogonal to the direction of the mean spin.

5.2. Spin Squeezed States

Since the elementary spins of a CSS are uncorrelated, the variance of the components normal to the mean direction is the sum of the variance of the individual elementary spins which gives the SQL. One way to exceed the SQL of an uncorrelated atomic ensemble is to use quantum entanglement to either increase the slope $\partial J_z/\partial\delta$, lower the shot noise $\langle\Delta J_z\rangle$, or a combination of both. Spin squeezing utilizes the latter method to yield a decreased noise in J_z (quantity of interest) at the expense of increased noise in J_x (which

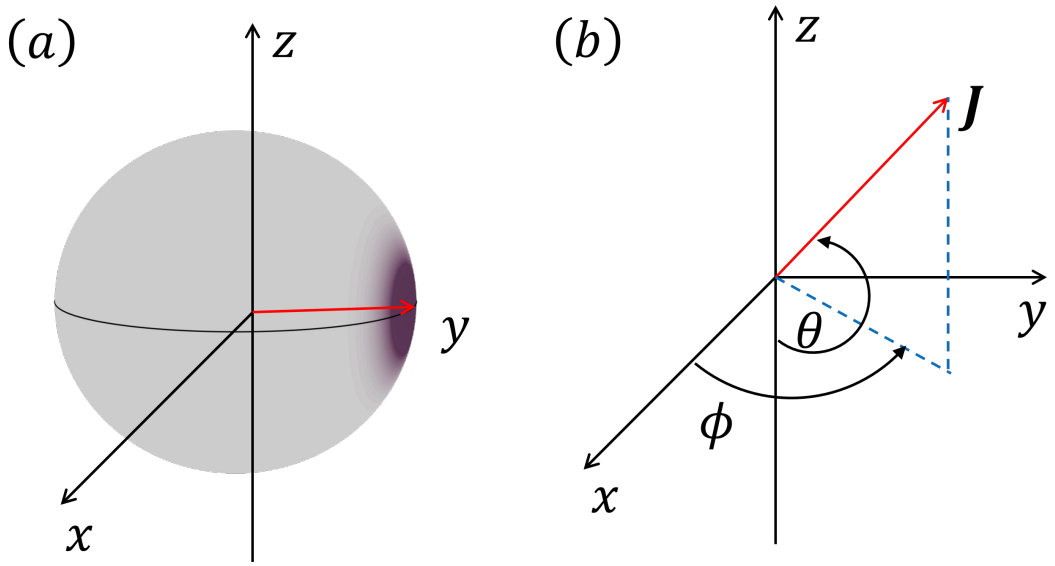

Figure 5.1. (a) Bloch sphere representation of a CSS. In this illustration the CSS is prepared along the $\hat{\mathbf{x}}$-axis. The quasiprobability distribution (QPD) for the CSS noise in J_x and J_z (coordinate system defined in (b)) is shown as a noise blob (purple disc) at the tip of the collective spin $\hat{\mathbf{J}}$ (red arrow). (b) Coordinate system defining the collective spin polar angle θ and azimuthal angle ϕ. The Cartesian components of the collective spin $\hat{\mathbf{J}}$ in the x, y and z directions are J_x, J_y and J_z.

is not measured). A linear Hamiltonian merely rotates the individual spins and does not establish quantum correlations among them. For this reason, a nonlinear interaction is the key to correlate the atoms. A single atom cannot be squeezed since it has no partner to be correlated with. In this segment, we will primarily focus on two methods of achieving spin squeezed states - One Axis Twist (OAT), and Two Axes Counter-Twist (TACT) Spin Squeezing.

5.2.1. One Axis Twist Spin Squeezing

In this section, we consider the CSS, $|\pi/2, \pi/2\rangle$ to demonstrate the process for generating an OAT spin squeezed state. The pertinent nonlinear Hamiltonian for achieving an OAT

state, H_{OAT}, is

$$H_{OAT} = \frac{\hbar\chi}{2} J_z^2. \tag{5.11}$$

This acts on a CSS to produce a squeezed spin state (SSS)

$$|SSS\rangle = \exp\left(-i\frac{\mu}{2}J_z^2\right)|CSS\rangle\,, \tag{5.12}$$

where $\mu = 2\chi\tau$ is the squeezing parameter, and τ is the duration of the squeezing interaction. The uncertainties in the CSS are distorted as μ increases. For example, the action of the OAT Hamiltonian on the CSS $|\pi/2, \pi/2\rangle$ is as follows

$$\begin{aligned} |\frac{\pi}{2}, \frac{\pi}{2}\rangle_{OAT} &= \exp\left(-i\frac{\mu}{2}J_z^2\right)|\frac{\pi}{2}, \frac{\pi}{2}\rangle \\ &= 2^{-J}\sum_{k=0}^{2J} i^k \binom{2J}{k} \exp(-i\frac{\mu}{2}(-J+k)^2)\,|-J+k\rangle \end{aligned} \tag{5.13}$$

As μ increases, the Husimi quasiprobability distribution (QPD) of $|\frac{\pi}{2}, \frac{\pi}{2}\rangle_{OAT}$ is deformed due to the rearrangement of the uncertainties in the $x - z$ plane, as shown in Fig.5.2a. The maximum value of the QPD decreases with an increase in μ. To access the decreased uncertainty along J_z, $|\pi/2, \pi/2\rangle_{OAT}$ is rotated by an angle ν about the **y**-axis so that the resulting $\langle \Delta J_z^2 \rangle$ is minimized (Fig.5.2b). For every J value, there is an optimal value of μ beyond which the QPD deviates from a geodesic, and exhibits *swirliness*. This optimal value of the coefficient of twist, μ_{OAT} is found from the minima of the Kitagawa-Ueda criterion, $\xi_{KU} = 2\langle \Delta J_z^2 \rangle / |\langle J_z \rangle| \leq 1$, and decreases with increasing J, as shown in Fig.5.3(a). The angle of corrective rotation, ν approaches zero as the spin number

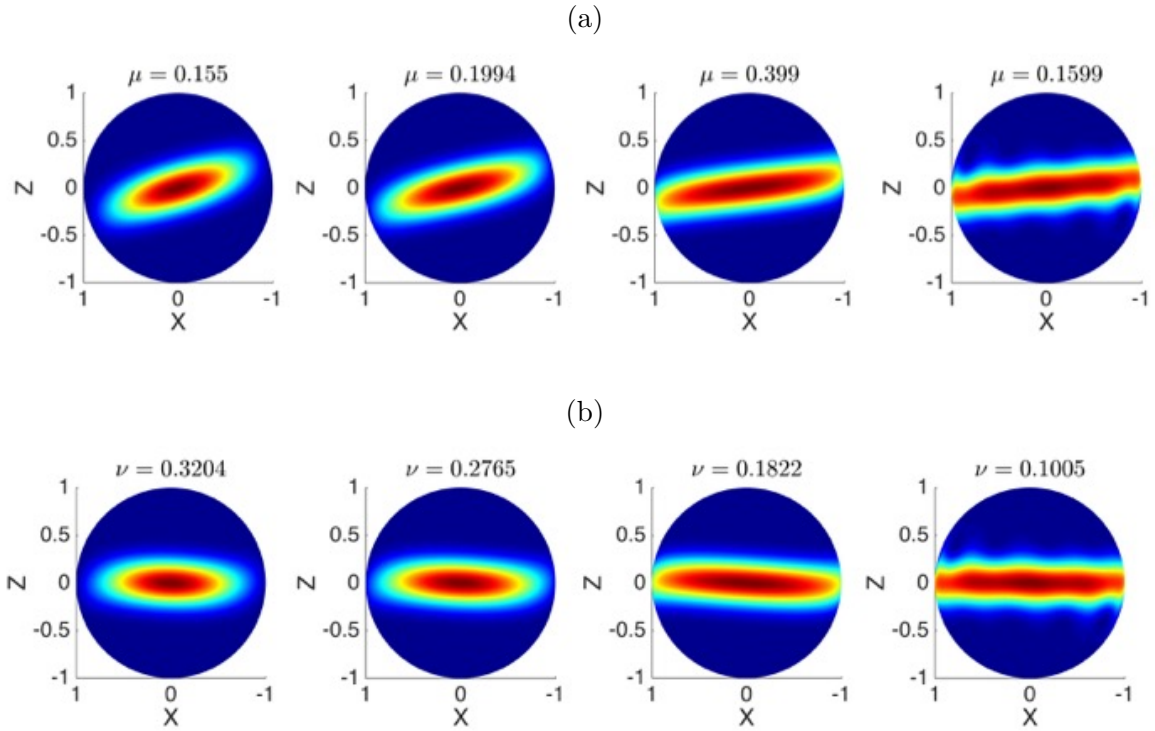

Figure 5.2. (a) QPD of the state evolution due to the action of H_{OAT} on $|\frac{1}{2}, \frac{1}{2}\rangle$, for $J = 20$. As the value of μ increases, the QPD continues to get distorted, and begins to exhibit *swirliness*. (b) For a given J, the angle of corrective rotation ν decreases with an increase in μ.

increases, as depicted in Fig.5.3(b). We note here that there exists another criterion for obtaining the limits on spin squeezing given by Wineland, et. al [**51**, **52**].

5.2.2. Two Axes Counter-Twist Spin Squeezing

Another method of surpassing the SQL is the TACT. If the QPD is simultaneously twisted clockwise and counterclockwise about two orthogonal axes, both normal to the mean spin vector of the CSS, the swirliness cancels out. In this section, we will consider the twisting of $|\pi/2, \pi/2\rangle$ along $J_x + iJ_z$ and $J_x - iJ_z$. The pertinent nonlinear Hamiltonian for achieving

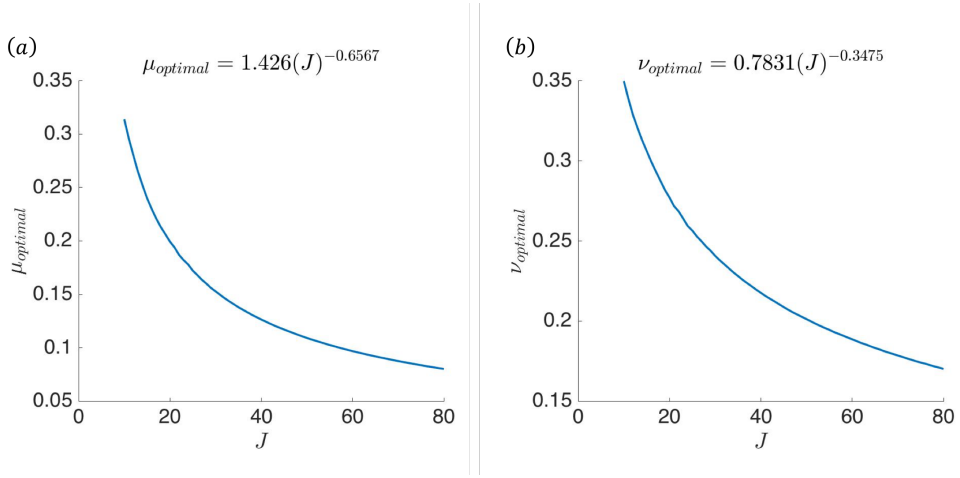

Figure 5.3. (a) Variation of the optimal value of the squeezing parameter with J. (b) Variation of the angle of corrective rotation with J.

a TACT state, H_{TACT} is given by the following expression

$$H_{TACT} = \frac{\hbar\mu}{4i}\left(\left(\frac{J_x - iJ_z}{\sqrt{2}}\right)^2 - \left(\frac{J_x + iJ_z}{\sqrt{2}}\right)^2\right). \tag{5.14}$$

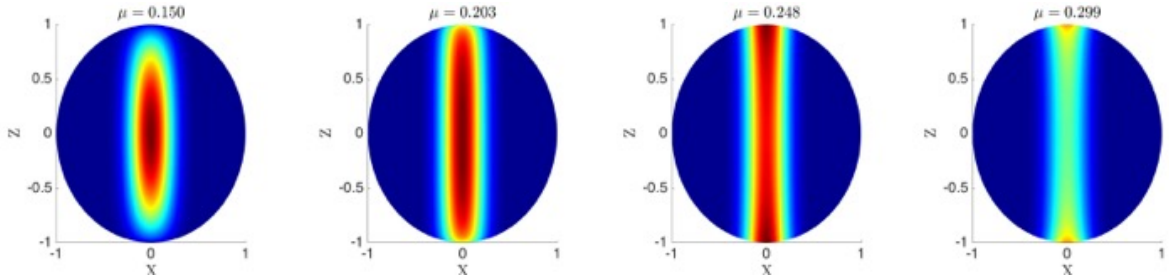

Figure 5.4. State evolutions by TACT spin squeezing represented in terms of the QPD for $J = 20$. The QPD begins to split into two parts as a result of oversqueezing.

Unlike the H_{OAT}, the action of H_{TACT} on $|\pi/2, \pi/2\rangle$ does not have an analytical solution. The MATLAB code for generating the QPD due to this given in Appendix. B. As is the case with the OAT spin squeezed states, there exists an optimal value of μ beyond which the QPD distorts and eventually splits into two. This optimal μ, denoted in

this thesis as μ_{TACT} is obtained in a similar way as μ_{OAT}, by applying the Kitagwa-Udea criterion. Figure5.4 shows the resulting QPD, for $J = 20$ due to various μ.

5.3. Spin Representation of Atom Interferometry

The discussion of the atom interferometric sequence in the spin representation is central to the analyses presented in Chapter 6. In this section, we will first review the CRAIN assuming an ensemble of N two-level atoms with a collective spin $\hat{\mathbf{J}}$ (Eq. 5.4). We will establish the standard quantum limit that restricts the phase sensitivity. We will then extend this knowledge to the COSAIN.

5.3.1. CRAIN in Spin Representation

The ensemble is initially prepared in a CSS, $|-\hat{\mathbf{z}}\rangle \equiv |E_0\rangle = \prod_{i=1}^{N} |\downarrow_i\rangle$. The first $\pi/2$-pulse rotates the CSS about the $\hat{\mathbf{x}}$ axis, producing the state

$$\begin{aligned} |\hat{\mathbf{y}}\rangle &= e^{-i(\pi/2)J_x} |-\hat{\mathbf{z}}\rangle \\ &= \prod_{i=1}^{N} \frac{(|\downarrow_i\rangle - i\,|\uparrow_i\rangle)}{\sqrt{2}}. \end{aligned} \tag{5.15}$$

Owing to the difference in linear momenta between $|\downarrow\rangle$ and $|\uparrow\rangle$, the trajectory of the atoms splits into two. The CSS is then left to evolve through a dark zone, during which it may pick up a phase due to metrological process of interest. As an example, we consider the case of rotation. Rigorously, the effect of the overall phase shiftϕ due to rotation is uniformly spread throughout the interferometric sequence. However, for theoretical convenience, we introduce it in two equal parts during each of the dark zones. Thus, at

the end of the first dark zone, the CSS picks up an additional phase $\phi/2$ yielding the state

$$e^{i\phi J_z/2}\left|\hat{\mathbf{y}}\right\rangle = \prod_{i=1}^{N}\frac{(\left|\downarrow_i\right\rangle - ie^{i\phi/2}\left|\uparrow_i\right\rangle)}{\sqrt{2}}. \tag{5.16}$$

At this point, a π-pulse is applied to the ensemble, causing the spins to flip, yielding

$$e^{-\pi J_z}e^{i\phi J_z/2}\left|\hat{\mathbf{y}}\right\rangle = \prod_{i=1}^{N}-\frac{(e^{i\phi/2}\left|\downarrow_i\right\rangle + i\left|\uparrow_i\right\rangle)}{\sqrt{2}}. \tag{5.17}$$

A second dark zone ensues, lending another phase factor to the ensemble, so that the CSS is now

$$e^{-i\phi J_z/2}e^{-i\pi J_x}e^{i\phi J_z/2}\left|\hat{\mathbf{y}}\right\rangle = \prod_{i=1}^{N}-\frac{e^{i\phi/2}(\left|\downarrow_i\right\rangle + ie^{-i\phi}\left|\uparrow_i\right\rangle)}{\sqrt{2}}. \tag{5.18}$$

The final $\pi/2$-pulse causes another rotation about the $\hat{\mathbf{x}}$ axis which establishes the final state,

$$\begin{aligned}\left|\psi\right\rangle &= e^{-i(\pi/2)J_x}e^{-i(\phi/2)J_z}e^{-i\pi J_x}e^{i(\phi/2)J_z}\left|\hat{\mathbf{y}}\right\rangle \\ &= \prod_{i=1}^{N}-\frac{1}{2}e^{-i\phi/2}((1+e^{i\phi})\left|\downarrow_i\right\rangle + i(1-e^{i\phi})\left|\uparrow_i\right\rangle).\end{aligned} \tag{5.19}$$

Essentially, this pulse catalyzes interference between the two trajectories of the interferometer. The goal of an AI is to measure ϕ and, therefore, Ω_G as accurately as possible. In a CRAIN, ϕ is measured by mapping it onto the collective spin projection $\hat{J}_z = (\hat{N}_\uparrow - \hat{N}_\downarrow)/2$. The signal, which is a measure of the population of $\left|\downarrow\right\rangle$ is, therefore,

$$S_{CRAIN} = J + \langle -\hat{J}_z\rangle = N\cos^2(\frac{\phi}{2}). \tag{5.20}$$

5.3.2. Standard Quantum Limit

The measurement process causes wavefunction collapse of the individual spins from the superposition state to $|\downarrow\rangle$, resulting in quantum projection noise in the measure of the signal,

$$\Delta S_{CRAIN} = \Delta(-\hat{J}_z) = \sqrt{N/4}\sin(\phi). \tag{5.21}$$

The pertinent gauge of the stability of measurement of rotation Ω_G is the quantum fluctuation in rotation (QFR), which is given by the ratio of the projection noise in measurement of Ω_G and the angular variation in signal (AVS). Assuming ideal quantum efficiency, the QFR is given by

$$\begin{aligned} \Delta\Omega_G\big|_{CRAIN} &= \frac{\Delta(-\hat{J}_z)}{\partial_{\Omega_G}\langle -\hat{J}_z\rangle} \\ &= \frac{c^2}{2\omega_C\Theta\sqrt{N}}, \end{aligned} \tag{5.22}$$

where $\partial_{\Omega_G} \equiv \partial/\partial\Omega_G$. This is the standard quantum limit. The SQL can be surpassed by introducing entanglement in the collective spin via spin squeezing.

5.3.3. COSAIN in Spin Representation

The COSAIN differs from a CRAIN in that the measurement of the signal is done on a Dicke collective state of the ensemble, instead of a single atomic state. The first $\pi/2$-pulse couples the initial state $|E_0, p_z = 0\rangle$ to $|E_1, p_z = \hbar k\rangle$, which in turn is coupled to $|E_2, p_z = 2\hbar k\rangle$, etc. This causes the ensemble to split into $N+1$ trajectories. The dark zone that immediately follows imparts a phase $e^{in\phi/2}$ to $|E_n\rangle$. At this point, the π-pulse

generates a spin flip in the individual spins in the CSS, causing $|E_n\rangle$ to become $|E_{N-n}\rangle$, and vice versa. The second dark-zone lends a phase $e^{i(0.5N-n)\phi}$ to $|E_n\rangle$. The mathematical derivation of this mechanism is discussed in detail in Chapter 4. The last $\pi/2$-pulse causes each of the collective states to interfere with the rest of the states. The COSAIN can, thus, be viewed as an aggregation of interference patterns due $\binom{N+1}{2}$ CRAIN's working simultaneously. The narrowest constituent signal fringes are derived from interferences between states with the largest difference in phase, i.e. $|E_0\rangle$ and $|E_N\rangle$. The full width at half maximum (FWHM) of this fringe is ϱ/N. The FWHM of the rest of the signal components lie between ϱ and $\varrho/(N-1)$. The signal, which is the measure of population of $|E_0\rangle$ is the result of the weighted sum of all the pairwise interferences. This is detected by projecting the final state of the ensemble, $|\psi\rangle$ on $|E_0\rangle$. Thus, $S_{COSAIN} = \langle\hat{G}\rangle = \cos^{2N}(\phi/2)$, where $\hat{G} \equiv |E_0\rangle\langle E_0|$. The quantum projection noise is the standard deviation of $\hat{G}$, given by $\Delta S_{COSAIN} = \cos^{N}(\phi/2)\sqrt{1-\cos^{2N}(\phi/2)}$. The rotation sensitivity, QFR of the COSAIN is thus,

$$\Delta\Omega_G\Big|_{COSAIN} = \left|\frac{\Delta\hat{G}}{\partial_{\Omega_G}\langle\hat{G}\rangle}\right| \tag{5.23a}$$

$$= \frac{\Delta\Omega_G\Big|_{CRAIN}}{\sqrt{N}}\left|\frac{\sqrt{\sec^{4J}(\phi/2)-1}}{\tan(\phi/2)}\right|. \tag{5.23b}$$

Therefore, for $\Omega_G \to 0$, the rotation sensitivity of the COSAIN, under quantum noise limited operation, is same as that of a CRAIN, assuming that all the other factors remain the same.

5.4. Spin Squeezed CRAIN and COSAIN

After the first $\pi/2$-pulse, the CSS in Eq. 5.15 is squeezed to produce an entangled state of the ensemble. The angle of corrective rotation is determined by ensuring that the fluctuations in $\hat{J}_z$ is minimum at $\phi = \pi/2$. This corresponds to aligning the direction of minimum fluctuations along the $\hat{\mathbf{x}}$ axis, so that the ν in Sec. 5.2.1 is shifted by $\pi/2$.

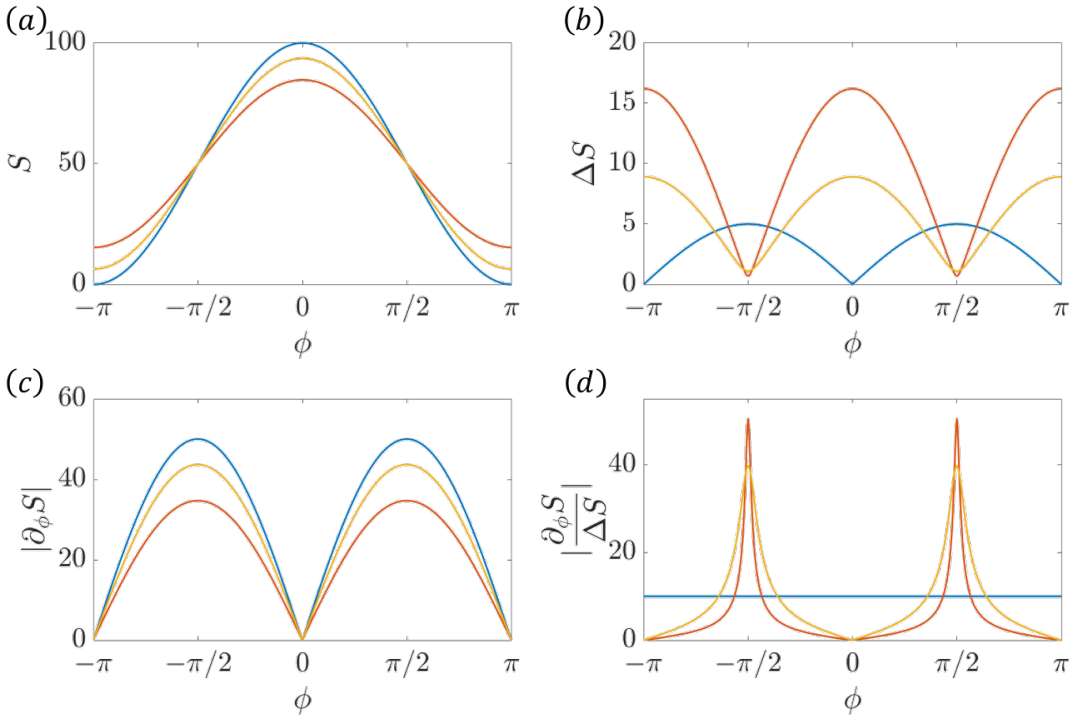

Figure 5.5. Variation of (a) Signal, (b) standard deviation, (c) angular variation of signal (AVS), (d) QRF^{-1} in a CRAIN with $N = 100$ due to spin squeezing. Blue lines indicate no squeezing, yellow lines indicate OAT, and Red lines indicate TACT.

The application of spin squeezing causes the signal amplitude to drop in a CRAIN, as shown in Fig. 5.7(a). However, at $\phi = \pi/2$, the signal amplitude remains unaltered, while the quantum projection noise dips to a minimum (Fig. 5.7(b)), leading to a net rise in phase sensitivity. The dependence of phase sensitivity on OAT and TACT squeezing

as a function of N is illustrated in Fig 5.6. Theoretically, the conventional application of two axis counter-twisting (TACT) spin squeezing to a CRAIN yields phase sensitivity approaching the Heisenberg limit [**31**]. However, despite several proposals, the TACT has not been experimentally realized so far [**53**–**56**]. In contrast, the conventional application of OAT in a CRAIN yields a phase sensitivity $\sim \pi/N^{5/6}$ but can be easily realized in a cavity [**57**–**60**].

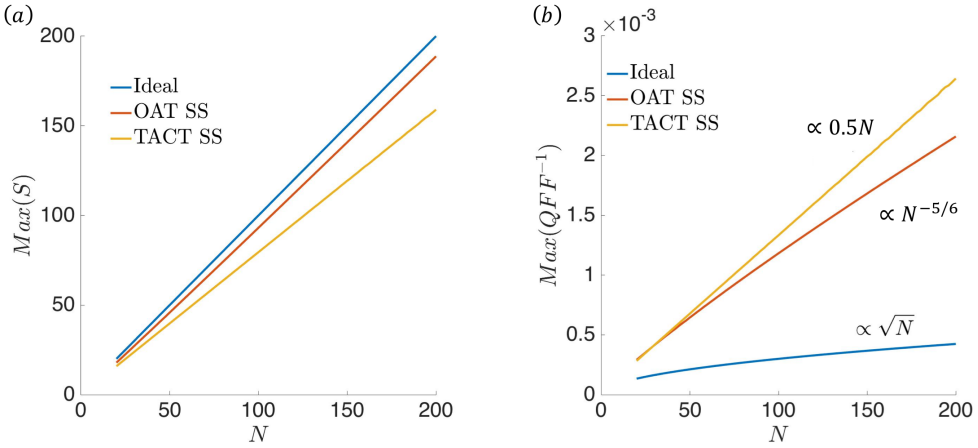

Figure 5.6. (a) As N increases, the peak value of CRAIN signal amplitude decreases due to squeezing. (b)

In a COSAIN, spin squeezing lowers the signal amplitude to an extent that the phase sensitivity worsens due it, as illustrated in Fig. 5.7.

In the next chapter, we describe the Schrödinger cat atomic interferometer (SCAIN), where we seek to undo the effect of squeezing in order to restore the maximum signal amplitude of a COSAIN to unity. We employ the experimentally achievable OAT spin squeezing in combination with unsqueezing which results in the generation of Schrödinger cat states corresponding to an equal superposition of the extremal Dicke collective states.

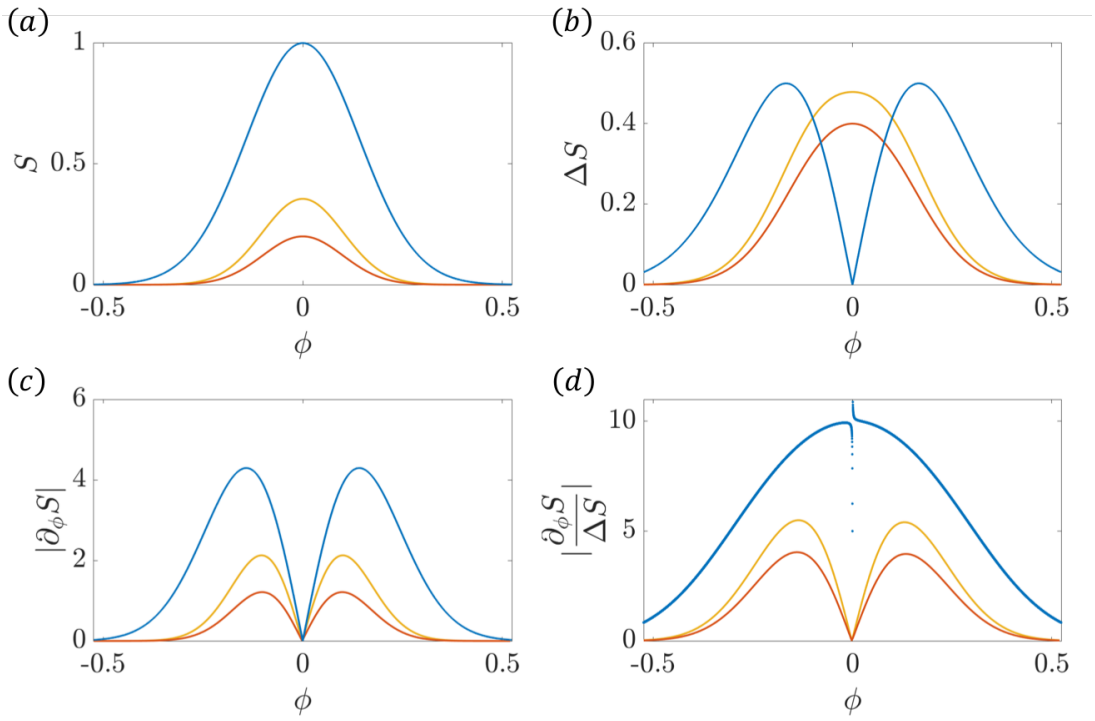

Figure 5.7. Variation of (a) Signal, (b) standard deviation, (c) angular variation of signal (AVS), (d) QRF^{-1} in a COSAIN with $N = 100$ due to spin squeezing. Blue lines indicate no squeezing, yellow lines indicate OAT, and Red lines indicate TACT.

This method exceed the phase sensitivity achieved by the conventional application of TACT spin squeezing discussed above.

CHAPTER 6

Schrödinger Cat Atomic Interferometer

6.1. Introduction

The phase sensitivity of an atomic interferometer (AI) depends on the Compton frequency, $\omega_C = mc^2/\hbar$ of the individual particles interfering at non-relativistic velocities, where m is the mass of the particle, and c is the velocity of light in vacuum [**2**, **4**, **23**, **61**]. Matter wave interferometry with large molecules have successfully demonstrated the superposition of quantum states with large mass [**37**]. However, these interferometers, based on the Talbot effect, are not suited for rotation sensing, owing to constraints in fabricating gratings of small enough spacing, and associated effects of van der Waals interaction. An alternative approach is to treat a large number of particles, each with a mass m, as a single object with a mass of $M \equiv Nm$, and thus a Compton frequency of $Mc^2/\hbar$. In this chapter, we describe a protocol that enables the realization of an atomic interferometer where two distinct quantum states of this mesoscopic single object, each with this Compton frequency, are spatially separated and then recombined, leading to fringes that are a factor of N narrower than what is achieved with a conventional atomic interferometer. We also show that the net metrological sensitivity of this interferometer is equivalent to the Heisenberg limited (HL) sensitivity of a conventional atomic interferometer. Aside from application to metrology, such a mesoscopic Schrödinger cat interferometer may

serve as a test-bed for various aspects of fundamental physics, such as the effect of gravitational red-shift on macroscopic decoherence [**38**] and the transition between quantum physics and classical realism [**62**]. It also opens up a new regime for atom-interferometric measurement of gravitational red-shift [**15**] and for exploring performance of matter-wave clocks [**11**] in a regime with a much higher Compton frequency. We also show how such a mesoscopic single object can be used to increase the effective base frequency of an atomic clock by a factor of N, with a metrological sensitivity that is equivalent to the HL sensitivity of a conventional atomic clock.

In Chapter 4, we showed that the effect of large Compton frequency can be observed indirectly by detecting one of the collective state. These states, $\{|E_0\rangle, |E_1\rangle, \ldots, |E_N\rangle\}$, arise as a result of interaction of an ensemble of identical independent atoms with a semiclassical field [**35**,**39**,**40**]. The interferences between each of the collective states lead to a reduction in signal linewidth by a factor of $\sqrt{N}$ as compared to a CRAIN. A direct transition $|E_0\rangle \leftrightarrow |E_N\rangle$, bypassing all the intermediate collective states, would result in a signal linewidth narrowed by a factor of N, thereby achieving HL phase sensitivity. However, since the electric dipole coupling rate between $|E_0\rangle$ and $|E_N\rangle$ is zero for non-interacting atoms, it is impossible to achieve this goal with conventional excitation.

In this chapter, we describe the application of squeezing and unsqueezing [**63**–**66**] in a COSAIN to attain HL of phase sensitivity. Explicitly, we employ what is known as the one axis twisting (OAT) spin squeezing [**31**] immediately following the first $\pi/2$-pulse. Prior to the application of the squeezing interaction, the population of the collective states follow a binomial distribution, corresponding to the Coherent Spin State (CSS) [**40**]. As the strength of squeezing is increased, the distribution begins to flatten out, eventually

generating Schrödinger cat states corresponding to an equal superposition of $|E_0\rangle$ and $|E_N\rangle$ [**67**]. The usual dark-π-dark sequence follows, at the end of which we undo the squeezing by applying a reverse OAT interaction. Finally, the last $\pi/2$ effectuates interference between the collective states that are detected by measuring the population of one of the collective states.

This technique critically depends on whether N is even or odd [**67**,**68**], a priori knowledge of which is virtually impossible for large ensembles. We circumvent this by detecting the state $|E_0\rangle$ using the null detection protocol described in Ref. [**30**]. When N is even, the interference between the two extremal states produce signal fringes narrowed by a factor of N. For odd N, the signal is zero, if the protocol is kept unchanged from the one used for even values of N. Thus, over repeated measurements (for example, using atoms released from a magneto-optic trap) under which the probability of N being even or odd is equal, this process produces a fringe amplitude that is reduced by a factor of 2. Thus, the sensitivity is $1/\sqrt{2}$ times the HL for N atoms. Alternatively, one can view the process as one that filters out the signal from the odd N cases, so that for $N/2$ atoms corresponding to even N cases, the sensitivity achieves the HL. We also show that a degree of sensitivity enhancement very close to this value can also be achieved for a much lower degree of squeezing than what is required for reaching the Schrödinger cat states. Since the system is highly entangled, and mesoscopic, we name this a Schrödinger Cat Atomic Interferometer (SCAIN). Finally, we also show how the proposed scheme can be used to realize a HL Schrödinger cat atomic clock, for which the base frequency is effectively enhanced by a factor of N.

6.2. Signal Fringewidth, SNR, Quantum Rotation Fluctuation

To appreciate the utility of a quantum metrological device, it is essential to consider the stability of its measurements. For example, an AI gyroscope rotating at a rate Ω_G about an axis normal to the area Θ accrues a phase difference $\phi = 2\omega_C\Theta\Omega_G/c^2$ between its trajectories [**24**]. One indicator of its performance is the quantum fluctuation in rotation (QFR), ascribed to the stability of the measurement of Ω_G. To recall, the fringe linewidth of a CRAIN is $\varrho = c^2/2\omega_C\Theta$, and the effective signal-to-noise ratio (SNR) is $\sqrt{N}$. Thus, the QFR, which is the ratio of noise to the angular variation in signal is $\varrho/\text{SNR}=c^2/2\sqrt{N}\omega_C\Theta$, as shown in Fig. 6.1. The precision of a CRAIN is thus constrained by standard quantum limit (SQL). On the other hand, the COSAIN treats the ensemble of independent atoms as a single particle so that the effective SNR is unity. Therefore, even though the signal linewidth is $\sim \varrho/\sqrt{N}$, the QFR turns out to be the same as that of a CRAIN. Similarly, the SCAIN essentially treats the ensemble as a single particle so that the effective SNR is unity. However, owing to the linewidth narrowing by a factor $\sim N$, the QFR attained approaches the HL, $c^2/2N\omega_C\Theta$. Theoretically, the conventional application of two axis counter-twisting (TACT) spin squeezing to a CRAIN yields phase sensitivity approaching the HL [**31**]. However, despite several proposals, the TACT has not been experimentally realized so far [**53**–**56**]. In contrast, the conventional application of OAT in a CRAIN yields a phase sensitivity $\sim \pi/N^{5/6}$ but can be easily realized in a cavity [**57**–**60**]. Thus, the SCAIN is in some ways equivalent to the TACT CRAIN, but realizable experimentally using OAT. Of course, as mentioned earlier, the SCAIN may have many applications in fundamental physics studies beyond conventional use in metrology.

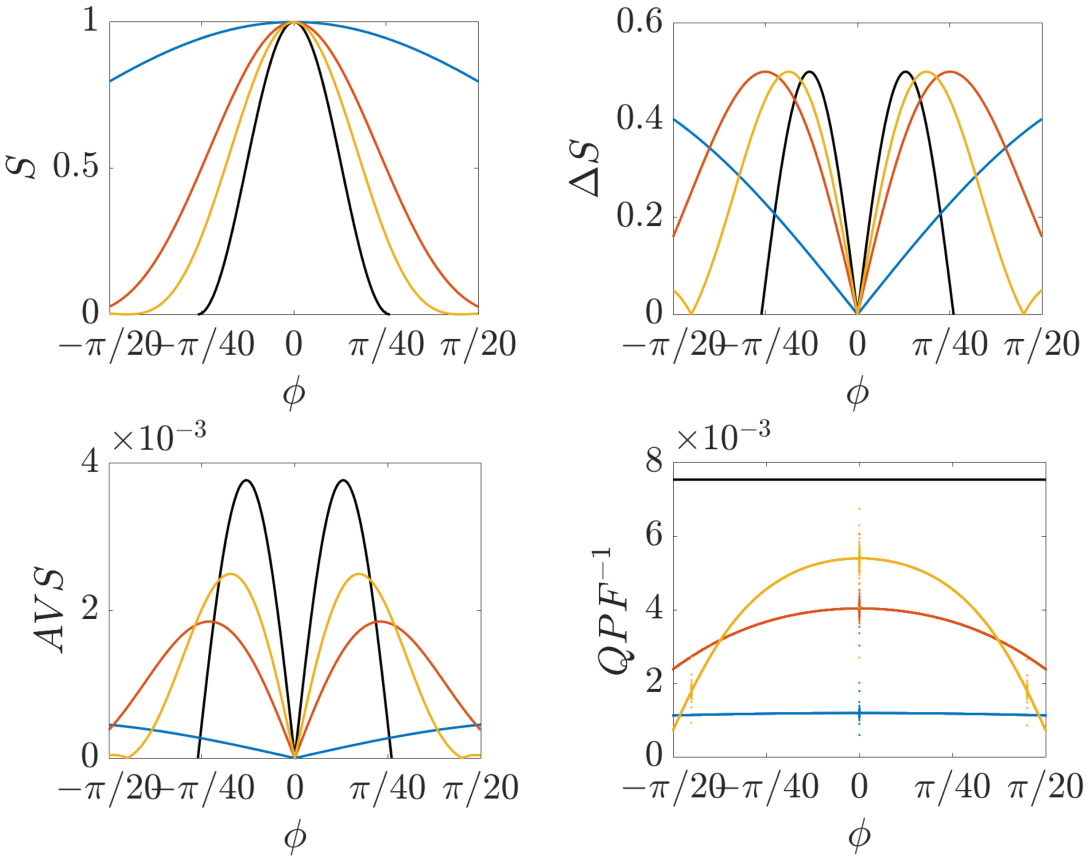

Figure 6.1. (a) Measurement of the interferometer signal (amplitude of $|E_0\rangle$) shows a narrowing of the fringe by a factor $0.35N$ in an excessively squeezed SCAIN (yellow line), as compared to an ideal COSAIN. (b) The rise in quantum projection noise in the vicinity of $\Omega_G = 0$ increases with squeezing. (c) Angular variation in signal as a measure of the slope of the signal. (d) The inverse of quantum phase fluctuation (QPF^{-1}) in a COSAIN. Black lines indicates the HL case of a GHZ state clock. Blue lines indicate the ideal COSAIN. For $\Omega_G \to 0$, the phase sensitivity of a COSAIN is very close to the SQL.

6.3. Squeezing and Unsqueezing Protocol

In order to illustrate clearly the mechanism for realizing the SCAIN, and the characteristics thereof, it is useful to recall briefly the operation of a CRAIN and a COSAIN, detailed discussions on which care given in Sec. 5.3.1 and Sec. 5.3.3, respectively. Briefly, these devices make use of N non-interacting identical three-level atoms with metastable hyperfine states $|\downarrow, p_z = 0\rangle$ and $|\uparrow, p_z = \hbar k\rangle$, and an excited state $|e\rangle$, in the Λ-configuration is reduced to an equivalent two-level model. The ensemble is initially prepared in a Coherent Spin State (CSS), $|-\hat{\mathbf{z}}\rangle \equiv |E_0\rangle = \prod_{i=1}^{N} |\downarrow_i\rangle$. The first $\pi/2$-pulse rotates the CSS about the $\hat{\mathbf{x}}$ axis, producing the state

$$\begin{aligned} |\hat{\mathbf{y}}\rangle &= e^{-i(\pi/2)J_x} |-\hat{\mathbf{z}}\rangle \\ &= \prod_{i=1}^{N} \frac{(|\downarrow_i\rangle - i\,|\uparrow_i\rangle)}{\sqrt{2}}. \end{aligned} \tag{6.1}$$

Following the dark-π-dark-$\pi/2$ sequence, the rotation sensitivity of both the CRAIN and the COSAIN is constrained by the SQL. One way of surpassing the SQL is to suppress the contribution of the constituent signal fringes broader than ϱ/N. This is accomplished by introducing entanglement in the CSS via the OAT spin squeezing Hamiltonian, $H_{OAT} = \chi J_z^2$. This produces a squeezed spin state (SSS) of the ensemble

$$|\psi_e\rangle = e^{-i\mu J_z^2/2} |\hat{\mathbf{y}}\rangle\,, \tag{6.2}$$

where $\mu = 2\chi\tau$ is the squeezing parameter, and τ is the duration of the squeezing interaction. The uncertainties in the CSS are distorted as μ increases. The direction along which the uncertainty in the collective spin dips below the classical limit is dictated by μ

and N, as shown by the quasiprobability distribution (QPD) in Fig. 6.4(b). To this end, the SSS must be rotated by an angle ν about an appropriate axis, the choices of which depend on the degree of squeezing.

6.3.1. $\mu \to \pi$

For even N, H_{OAT} transforms $|\hat{\mathbf{y}}\rangle$ to $|\psi_e\rangle = (|\hat{\mathbf{y}}\rangle + |-\hat{\mathbf{y}}\rangle)/\sqrt{2}$. Rotating $|\psi_e\rangle$ by $\nu = \pi/2$ about the $\hat{\mathbf{x}}$ axis yields the Schrödinger cat states $|\psi_{GHZ}\rangle = ((1+i)\,|E_0\rangle + (1-i)\,|E_N\rangle)/2$. At the end of the intermediate dark$-\pi-$dark sequence, the state of the ensemble is $e^{-i\phi J_z/2}e^{-i\pi J_x}e^{i\phi J_z/2}\,|\psi_{GHZ}\rangle = e^{iN\phi/2}((1-i)(-i)^N\,|E_0\rangle + (1+i)e^{-iN\phi}\,|E_N\rangle)/2$. As discussed above, the interference between states with a phase difference $N\phi$ produces signal fringes narrowed by a factor of N. To measure ϕ, we seek to undo the effect of squeezing on the system. This is accomplished in two steps − first, by undoing the effect of corrective rotation ν, followed by untwisting the action of H_{OAT}. Since the π-pulse induces a phase π in the spins, the effect of ν is undone by applying another rotation ν about the same axis as before. Thereafter, the untwisting Hamiltonian, $-H_{OAT}$ is applied to unfurl the hitherto entangled states. Finally, the last $\pi/2$ pulse is applied to catalyze interference between the resulting states. The signal arising from this interference depends on ϕ as $S_{GHZ} = \cos^2(N\phi/2)$.

When N is odd, initial squeezing produces $|\hat{\mathbf{x}}\rangle$ and $|-\hat{\mathbf{x}}\rangle$. Rotating these about the $\hat{\mathbf{x}}$ axis does not alter the states, and therefore, the sequence

$$e^{-i\nu' J_x}e^{-i\phi J_z/2}e^{-i\pi J_x/2}e^{i\phi J_z/2}e^{-i\nu' J_x} \tag{6.3}$$

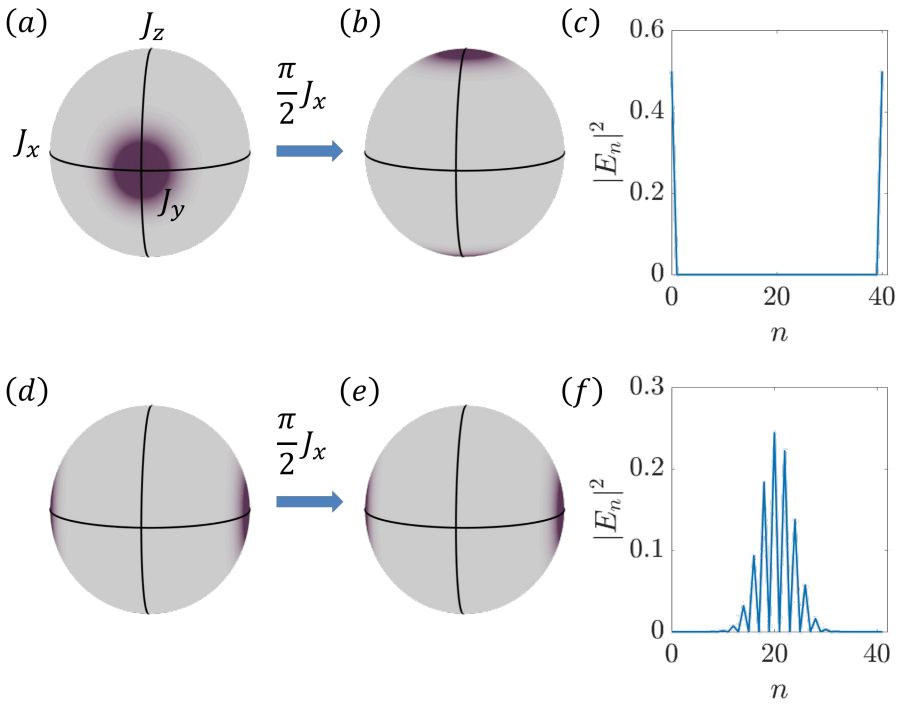

Figure 6.2. For even N (a→b) QPD of $|\psi_e\rangle$ rotated by $\pi/2$ about $\hat{\mathbf{x}}$ axis to yield Schrödinger cat states. (c) Distribution of states of the rotates SSS, showing an equal proportion of states $|E_0\rangle$ and $|E_N\rangle$. For odd N, (d→e) Rotation about $\hat{\mathbf{x}}$ axis does not transform the SSS. (f) Distribution of states of the rotates SSS.

only causes an identical phase change in each of these states. Finally, unsqueezing restores the original CSS, which is not altered by the final $\pi/2$ pulse. The whole sequence thus generates a null signal. Over repeated measurements, the probability of N being even or odd is equal. Thus, for M trials, the average signal of the SCAIN in this regime is $S_{GHZ} = M\cos^2(N\phi/2)/2$. The associated quantum projection noise is $\Delta S_{GHZ} = \sqrt{M/2}\sin(N\phi)$. The QFR is thus, $\Delta\Omega_G = c^2/\sqrt{2M}N\omega_C\Theta$.

6.3.2. $\mu < \pi$

The rotation axis and ν are chosen so as to minimize the fluctuations along $\hat{\mathbf{z}}$. This is achieved by rotating the SSS about the direction of the mean spin vector, $\hat{\mathbf{y}}$. Prior to rotation, the SSS has the same binomial distribution as the original CSS, as depicted in Fig 6.3(a). The rotation causes a reshuffle in the population of states, and the distribution begins to flatten out (Fig 6.3(b)). For a given value of N, ν increases with μ, reaching maximum value of $\pi/2$ at $\mu = \mu_0$. For a large ensemble, μ_0 can be achieved for a very short evolution time. When squeezed beyond μ_0, the distribution begins to invert, and the relative proportion of the extremal states increases. The exact state distribution is determined by whether N is even or odd (Fig 6.3(c)). At $\mu = \pi/2$, the QPD splits into four identical parts. For even N, the state of the ensemble is $|\psi_{rot}\rangle = e^{-i\nu\hat{J}_y}|\psi_e\rangle = (|-\hat{\mathbf{z}}\rangle + |\hat{\mathbf{y}}\rangle + |-\hat{\mathbf{y}}\rangle + |\hat{\mathbf{z}}\rangle)/2$, and the distribution becomes trimodal, as depicted by the blue line in Fig. 6.3(d). On the other hand, for odd N, $e^{-i\nu\hat{J}_y}|\psi_e\rangle = ((|\hat{\mathbf{y}}\rangle + |\hat{\mathbf{z}}\rangle)/\sqrt{2} + (|\hat{\mathbf{y}}\rangle + |-\hat{\mathbf{z}}\rangle)/\sqrt{2} + (-|\hat{\mathbf{y}}\rangle + |\hat{\mathbf{z}}\rangle)/\sqrt{2} + (|-\hat{\mathbf{y}}\rangle + |-\hat{\mathbf{z}}\rangle)/\sqrt{2})/2\sqrt{2}$. In this case, the distribution is bimodal, as shown in Fig. 6.3(d) (red line).

Once the SSS is optimally aligned, the usual dark$-\pi-$dark sequence follows. Similar to the case of $\mu = \pi$, the squeezing is undone by applying another rotation ν about $\hat{\mathbf{y}}$ axis, and untwisting the hitherto entangled states via $-H_{OAT}$. Finally, the last $\pi/2$ pulse is applied to catalyze interference between each of the resulting states. For $\phi = 0$, the original CSS is restored. However, for $\phi \neq 0$, the final state develops a bias along J_x proportional to ϕ, and entanglement remains in the system. The central fringe is identical for both N odd and even, so for M trials, the average signal is independent of the parity of N. Due to interferences at higher phase contrast, the resulting signal fringes are narrower

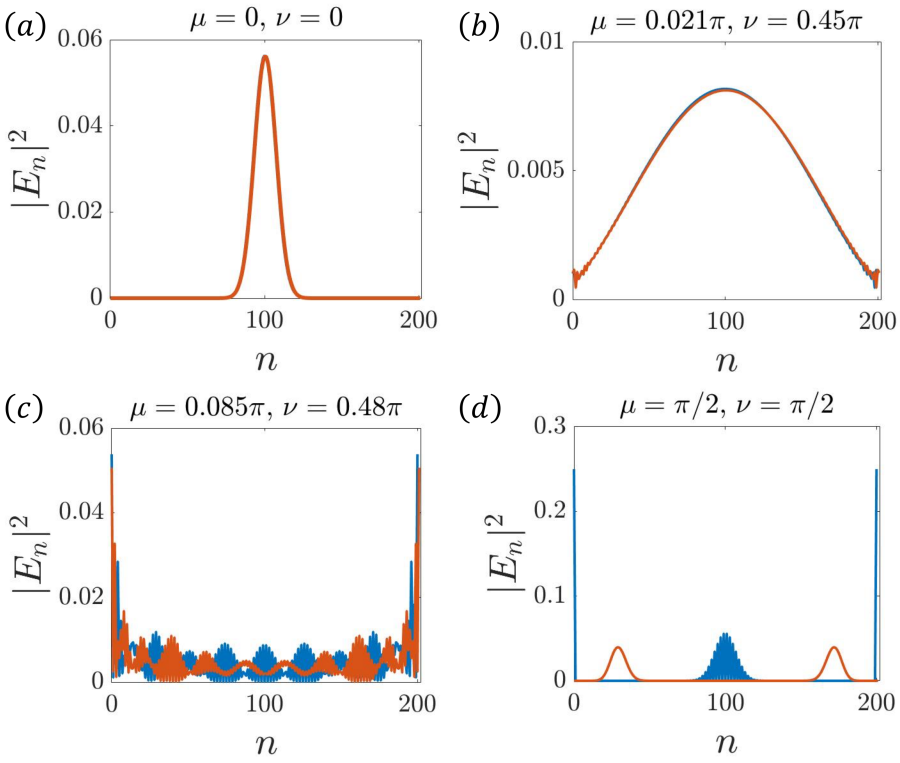

Figure 6.3. Variation of population of states distribution with μ. Both even (blue line) and odd (red line) values of N are considered.

than that in an identical COSAIN. The fringe width first decreases sharply with longer evolution times, and then saturates at $\mu = \mu_{opt}$. Consequently, the fluctuations in rotation sensitivity plummets, attaining the minimum value $\delta\Omega_G|_{SCAIN} = e^{1/3}c^2/2\sqrt{M}N\omega_C\Theta$, at $\mu = \mu_{opt}$.

Thus, the SCAIN can attain phase sensitivity that is very close to the HL, for an evolution time that is much shorter than that required to attain Schrödinger cat states. A similar treatment of the Collective State Atomic Clock [**42**] also produces similar results. Such a clock can be called a SCAC (Schrödinger Cat Atomic Clock). In this case, the Schrödinger Cat state for $\nu = \pi$ corresponds to a situation where the effective base

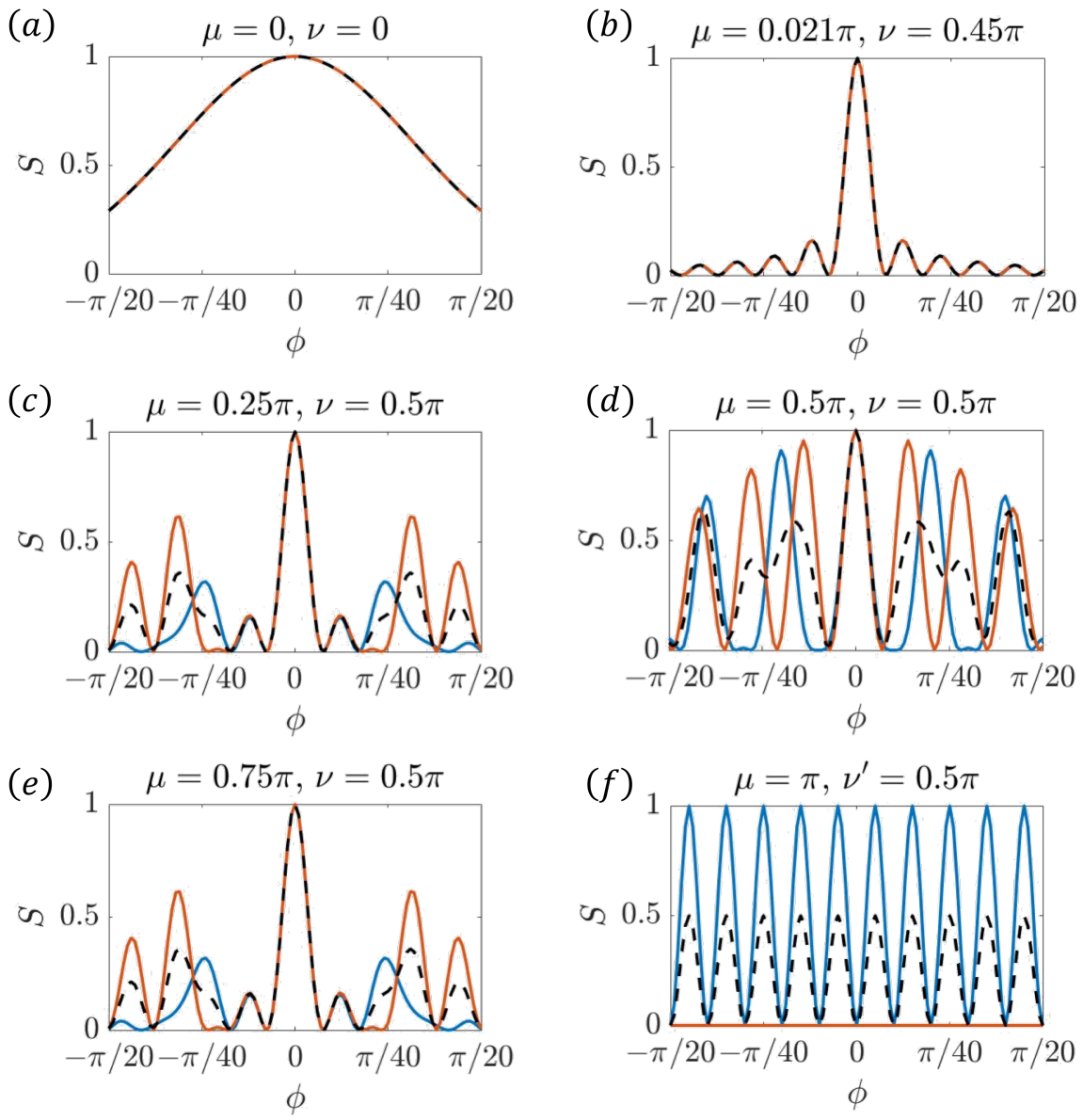

Figure 6.4. Signal fringes for various μ. $N = 200$ is indicated by blue lines, $N = 201$ by red lines. The broken black lines indicate the average signal.

frequency of the clock is increased by a factor of N. In the following section, we present a description of the SCAC, in the same vein as the SCAIN.

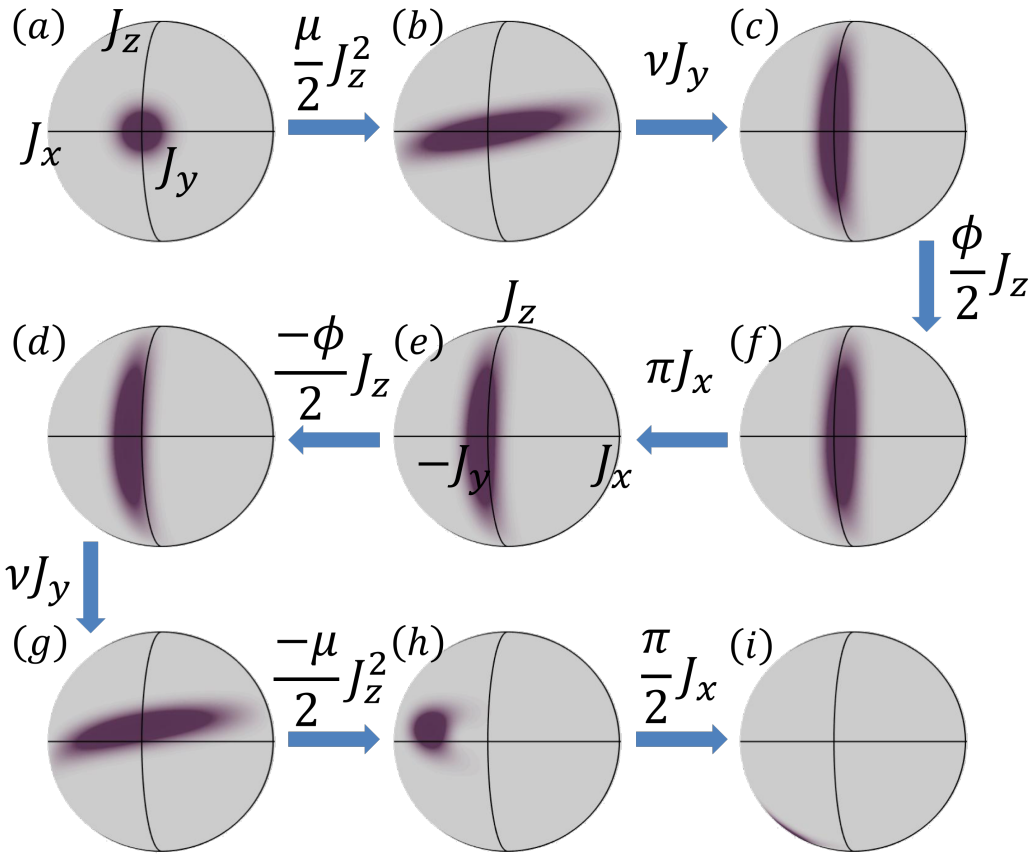

Figure 6.5. The Husimi quasiprobability distribution of state evolution through the SCAIN protocol. The initial CSS $|\hat{\mathbf{y}}\rangle$ (a) evolves under H_{OAT} to (b) which is then rotated (b→c)so as to maximize the fluctuations along $\hat{\mathbf{z}}$. (f) The first dark zone imparts a phase $\phi/2$. (e) The Bloch sphere is rotated to show the other face where the SSS is situated after the π pulse. (d) The second dark zone imparts the rest of the $\phi/2$ phase, and biases the spin precession. (d→g) The spins are effectively unrotated to restore the original orientation of the SSS, which are then unsqueezed to (h). (i) The final $\pi/2$ pulse that causes interference between the near-unsqueezed states.

6.4. Schrödinger Cat Atomic Clock

The ground states $|\downarrow\rangle$ and $|\uparrow\rangle$ of a three-level atom interact with an excited state $|e\rangle$ via two copropagating laser beams. One of the beams, detuned from resonance by δ_1 and with Rabi frequency Ω_1, couples $|\downarrow\rangle$ to $|e\rangle$. The other beam, with Rabi frequency Ω_2 and

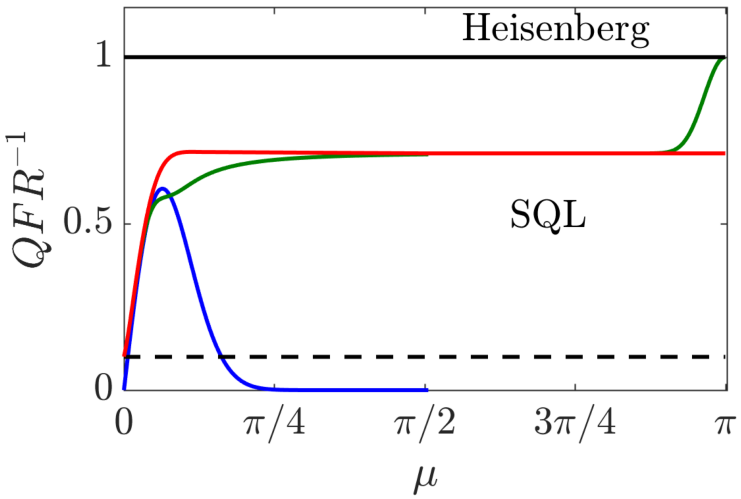

Figure 6.6. QFR^{-1} of SCAIN vs μ for $N = 100$, scaled with respect to the Heisenberg limit. Horizontal lines indicate the Heisenberg limit (black solid), and the SQL (black dashed). The red line indicates the rotation sensitivity achieved in a SCAIN considering the average of contributions form even and odd parity ensembles.

detuning δ_2, couples $|e\rangle$ to $|\uparrow\rangle$. For $\Delta \gg \Omega_1, \Omega_2$, where $\Delta = (\delta_1 + \delta_2)/2$, the interaction can be described as an effective two level system excited by an effective traveling wave with a Rabi frequency $\Omega = \Omega_1\Omega_2/2\Delta$, and detuning $\delta = \delta_1 - \delta_2$.

In a conventional Ramsey fringe atomic clock (RFAC), an ensemble of N effective two-level atoms is first prepared in the CSS, $|-\hat{\mathbf{z}}\rangle \equiv |E_0\rangle = \prod_{i=1}^{N} |\downarrow_i\rangle$. The initial $\pi/2$-pulse rotates the CSS about the $\hat{\mathbf{x}}$-axis and brings it to the $\hat{\mathbf{y}}$-axis, producing the state $e^{-i(\pi/2)J_x t_0} |-\hat{\mathbf{z}}\rangle = |\hat{\mathbf{y}}\rangle = \prod_{i=1}^{N}(|\downarrow_i\rangle - i\,|\uparrow_i\rangle)/\sqrt{2}$. The collective spin is then left to evolve without any interaction for time T_D, during which each constituent spin acquires a phase $\phi = 2\pi f T_D$, where $f = \delta/2\pi$ is the frequency of the clock in hertz. This is equivalent to a rotation by ϕ along the $\mathbf{z}$-axis. At this point, a second $\pi/2$-pulse is applied which establishes the final state, $|\psi\rangle = \prod_{i=1}^{N}((1 - e^{i\phi})\,|\downarrow\rangle - i(1 + e^{i\phi})\,|\uparrow\rangle)/2$. The aim of the RFAC is to measure ϕ, and therefore, f as precisely as possible.

In an ideal RFAC, ϕ is measured by mapping it onto the collective spin projection J_z. The signal, which a measure of the population of $|\uparrow\rangle$ is, therefore, $S_{RFAC} = J + \langle J_z \rangle = N\cos^2(\phi/2)$. The associated quantum projection noise is $\Delta S_{RFAC} = \Delta J_z = \sqrt{N/4}\sin(\phi)$. The stability of the measurement of f is an indicator of the performance of an atomic clock. The stability of the clock is attributed to the quantum fluctuation in frequency (QFF), analogous to the QRF described in the main body of this paper. The QFF can be written as

$$\begin{aligned} QFF = \Delta f &= \left| \frac{\Delta J_z}{\partial \langle J_z \rangle / \partial f} \right| \\ &= \left(2\pi T_D \sqrt{N} \right)^{-1}. \end{aligned} \tag{6.4}$$

which maybe be considered as quantum noise over the spectral variation of signal (SVS).

As is the case in a COSAIN, the COSAC differs from a conventional RFAC in that the measurement of the signal is done on a collective state of the ensemble, instead of single atom measurements [**42**]. The first $\pi/2$-pulse couples the initial state $|E_0\rangle$ to $|E_1\rangle$, which in turn is coupled to $|E_2\rangle$, etc., effectively causing the ensemble to split into $N+1$ states. During the dark zone, the n-th collective state $|E_n\rangle$ picks up a phase $e^{-in\phi}$. When the ensemble interacts with the last $\pi/2$-pulse, each of the collective states interfere with the rest of the states. The COSAC can, thus, be viewed as the aggregation of interference patterns due $\binom{N+1}{2}$ RFAC's working simultaneously. The mathematical derivation of this mechanism is discussed in detail in Ref [**42**]. The narrowest constituent signal fringes are derived from interferences between states with the largest difference in phase, i.e. $|E_0\rangle$ and $|E_N\rangle$, The full width at half maximum (FWHM) of this fringe is π/N. The FWHM

of the rest of the signal components lie between π and $\pi/(N-1)$. The signal, which is the measure of population of $|E_N\rangle$ is the result of the weighted sum of all the pairwise interferences. This is detected by projecting the final state of the ensemble, $|\psi\rangle$ on $|E_N\rangle$. Thus, $S_{COSAC} = \langle\hat{G}\rangle = \cos^{2N}(\phi/2)$, where $\hat{G} \equiv |E_N\rangle\langle E_N|$. The quantum projection noise is the standard deviation of $\hat{G}$, given by $\Delta S_{COSAC} = \cos^N(\phi/2)\sqrt{1-\cos^{2N}(\phi/2)}$. The QFF of the COSAC is thus,

$$\begin{aligned}\Delta f\Big|_{COSAC} &= \left|\Delta\hat{G}/\partial_f\langle\hat{G}\rangle\right| \\ &= (\Delta f\Big|_{CRAIN}/\sqrt{N})|\sqrt{\sec^{4J}(\phi/2)-1}/\tan(\phi/2)| \end{aligned} \tag{6.5}$$

Therefore, for $f \to 0$, the frequency sensitivity of the COSAC is same as that of an RFAC, assuming that all the other factors remain the same.

The Schrödinger cat atomic clock (SCAC) is based on the same principles of squeezing followed by perturbation and subsequent unsqueezing as the SCAIN. The CSS after the first $\pi/2$-pulse is squeezed via the OAT spin squeezing Hamiltonian, $H_{OAT} = \chi J_z^2$, yielding the squeezed spin state (SSS) of the ensemble $|\psi_e\rangle = e^{-i\mu J_z^2/2}|\hat{\mathbf{y}}\rangle$, where $\mu = 2\chi\tau$ is the squeezing parameter, and τ is the duration of the squeezing interaction. This SSS must be rotated by an angle ν about an appropriate axis, the choices of which depend on the degree of squeezing, and follows the same rules as described Sec 6.3.

6.4.1. $\mu \to \pi$

For even N, H_{OAT} transforms $|\hat{\mathbf{y}}\rangle$ to $|\psi_e\rangle = (|\hat{\mathbf{y}}\rangle + |-\hat{\mathbf{y}}\rangle)/\sqrt{2}$. Rotating $|\psi_e\rangle$ by $\nu = \pi/2$ about the $\hat{\mathbf{x}}$ axis yields the Schrödinger cat states $|\psi_{GHZ}\rangle = ((1+i)|E_0\rangle + (1-i)|E_N\rangle)/2$. At the end of the dark zone, the state of the ensemble is $e^{-i\phi J_z}|\psi_{GHZ}\rangle = ((1+i)|E_0\rangle +$

$(1-i)e^{-iN\phi}\,|E_N\rangle)/2$. To undo the effect of squeezing, we first undo the effect of corrective rotation ν by by applying another rotation ν about the $\hat{\mathbf{x}}$ axis. Thereafter, the untwisting Hamiltonian, $-H_{OAT}$ is applied to unfurl the hitherto entangled states. Finally, the last $\pi/2$ pulse is applied to catalyze interference between the resulting states. The signal arising from this interference depends on ϕ as $S_{GHZ} = \cos^2(N\phi/2)$.

When N is odd, initial squeezing produces $|\hat{\mathbf{x}}\rangle$ and $|-\hat{\mathbf{x}}\rangle$. Rotating these about the $\hat{\mathbf{x}}$ axis does not alter the states, and therefore, the sequence $e^{-i\nu' J_x}e^{-i\phi J_z}e^{-i\nu' J_x}$ only causes an identical phase change in each of these states. Finally, unsqueezing restores the original CSS, which is not altered by the final $\pi/2$ pulse. The whole sequence thus generates a null signal. Over repeated measurements, the probability of N being even or odd is equal. Thus, for M trials, the average signal of the SCAC in this regime is $S_{GHZ} = M\cos^2(N\phi/2)/2$. The associated quantum projection noise is $\Delta S_{GHZ} = \sqrt{M/2}\sin(N\phi)$. The QFF is thus, $\Delta f = 1/\sqrt{2M}\pi N T_D$.

6.4.2. $\mu < \pi$

The rotation axis and ν are chosen so as to maximize the fluctuations along $\hat{\mathbf{z}}$. This is achieved by rotating the SSS about the direction of the mean spin vector, $\hat{\mathbf{y}}$. Prior to rotation, the SSS has the same binomial distribution as the original CSS. The rotation causes a reshuffle in the population of states, and the distribution begins to flatten out. For a given value of N, ν increases with μ, reaching maximum value of $\pi/2$ at $\mu = \mu_0$. For a large ensemble, μ_0 can be achieved for a very short evolution time. When squeezed beyond μ_0, the distribution begins to invert, and the relative proportion of the extremal states increases. The exact state distribution is determined by whether N is even or

odd. At $\mu = \pi/2$, the QPD splits into four identical parts. For even N, the state of the ensemble is $|\psi_{rot}\rangle = e^{-i\nu\hat{J}_y}|\psi_e\rangle = (|-\hat{\mathbf{z}}\rangle + |\hat{\mathbf{y}}\rangle + |-\hat{\mathbf{y}}\rangle + |\hat{\mathbf{z}}\rangle)/2$, and the distribution becomes trimodal. On the other hand, for odd N, $e^{-i\nu\hat{J}_y}|\psi_e\rangle = ((|\hat{\mathbf{y}}\rangle + |\hat{\mathbf{z}}\rangle)/\sqrt{2} + (|\hat{\mathbf{y}}\rangle + |-\hat{\mathbf{z}}\rangle)/\sqrt{2} + (-|\hat{\mathbf{y}}\rangle + |\hat{\mathbf{z}}\rangle)/\sqrt{2} + (|-\hat{\mathbf{y}}\rangle + |-\hat{\mathbf{z}}\rangle)/\sqrt{2})/2\sqrt{2}$. In this case, the distribution is bimodal. The population of states at each stage follows the same distribution as in a corresponding SCAIN.

Once the SSS is optimally aligned, the usual dark zone follows. The squeezing is undone by applying another rotation $-\nu$ about $\hat{\mathbf{y}}$ axis, and untwisting the hitherto entangled states via $-H_{OAT}$. Finally, the last $\pi/2$ pulse is applied to catalyze interference between each of the resulting states. For $\phi = 0$, the original CSS is restored. However, for $\phi \neq 0$, the final state develops a bias along J_x proportional to ϕ, and entanglement remains in the system. The central fringe is identical for both N odd and even, so for M trials, the average signal is independent of the parity of N. Due to interferences at higher phase contrast, the resulting signal fringes are narrower than that in an identical COSAC. The fringe width first decreases sharply with longer evolution times, and then saturates at $\mu = \mu_{opt}$. Consequently, the fluctuations in rotation sensitivity plummets, attaining the minimum value $\Delta f|_{SCAIN} = e^{1/3}/\sqrt{M}2\pi NT_D$, at $\mu = \mu_{opt}$.

References

[1] Norman F. Ramsey. A molecular beam resonance method with separated oscillating fields. *Phys. Rev.*, 78:695–699, Jun 1950.

[2] Mark Kasevich and Steven Chu. Atomic interferometry using stimulated Raman transitions. *Physical Review Letters*, 67(2):181–184, 1991.

[3] M. Kasevich and S. Chu. Measurement of the gravitational acceleration of an atom with a light-pulse atom interferometer. *Applied Physics B Photophysics and Laser Chemistry*, 54(5):321–332, 1992.

[4] F. Riehle, Th Kisters, A. Witte, J. Helmcke, and Ch J. Bord?? Optical Ramsey spectroscopy in a rotating frame: Sagnac effect in a matter-wave interferometer. *Physical Review Letters*, 67(2):177–180, 1991.

[5] David W. Keith, Christopher R. Ekstrom, Quentin A. Turchette, and David E. Pritchard. An interferometer for atoms. *Physical Review Letters*, 66(21):2693–2696, 1991.

[6] O. Carnal and Jo Mlynek. Youngs double-slit experiment with atoms: A simple atom interferometer. *Physical Review Letters*, 66(21):2689–2692, 1991.

[7] T L Gustavson, A Landragin, and M a Kasevich. Rotation sensing with a dual atom-interferometer Sagnac gyroscope. *Classical Quant Grav*, 17(12):2385–2398, 2000.

[8] B. Canuel, F. Leduc, D. Holleville, A. Gauguet, J. Fils, A. Virdis, A. Clairon, N. Dimarcq, Ch J. Bordé, A. Landragin, and P. Bouyer. Six-axis inertial sensor using cold-atom interferometry. *Physical Review Letters*, 97(1), 2006.

[9] Achim Peters, Ky Chung, and Steven Chu. Measurement of gravitational acceleration by dropping atoms. *Nature*, 400:849–852, 1999.

[10] M. Snadden, J. McGuirk, P. Bouyer, K. Haritos, and M. Kasevich. Measurement of the Earth's Gravity Gradient with an Atom Interferometer-Based Gravity Gradiometer. *Physical Review Letters*, 81(5):971–974, 1998.

[11] Shau-Yu Lan, Pei-Chen Kuan, Brian Estey, Damon English, Justin M. Brown, Michael A. Hohensee, and Holger Müller. Supplementary Material for "A Clock Directly Linking Time to a Particle's Mass". *Science*, 339(6119):554–557, 2013.

[12] Rym Bouchendira, Pierre Cladé, Saïda Guellati-Khélifa, Francois Nez, and Francois Biraben. New determination of the fine structure constant and test of the quantum electrodynamics. *Phys. Rev. Lett.*, 106:080801, Feb 2011.

[13] Malo Cadoret, Estefania De Mirandes, Pierre Cladé, Sa??da Guellati-Khélifa, Catherine Schwob, Fran??ois Nez, Lucile Julien, and Fran??ois Biraben. Combination of bloch oscillations with a Ramsey-Bordé interferometer: New determination of the fine structure constant. *Physical Review Letters*, 101(23), 2008.

[14] J B Fixler, G T Foster, J M McGuirk, and M. A. Kasevich. Atom interferometer measurement of the newtonian constant of gravity. *Science*, 315(5808):74–77, 2007.

[15] Holger Müller, Achim Peters, and Steven Chu. A precision measurement of the gravitational redshift by the interference of matter waves. *Nature*, 463(February):926–929, 2010.

[16] R Geiger, V Ménoret, G Stern, N Zahzam, P Cheinet, B Battelier, a Villing, F Moron, M Lours, Y Bidel, a Bresson, a Landragin, and P Bouyer. Detecting inertial effects with airborne matter-wave interferometry. *Nature communications*, 2:474, 2011.

[17] M. S. Shahriar, M. Jheeta, Y. Tan, P. Pradhan, and A. Gangat. Continuously guided atomic interferometry using a single-zone optical excitation: Theoretical analysis. *Optics Communications*, 243(1-6):183–201, 2004.

[18] C.J. Foot. *Atomic physics*. Oxford master series in physics. Oxford University Press, 2005.

[19] M. Sargent, M.O. Scully, and W.E. Lamb. *Laser physics*. Number v. 201067196 in Advanced book program. Addison-Wesley Pub. Co., Advanced Book Program, 1976.

[20] D. Budker, D.F. Kimball, and D.P. DeMille. *Atomic Physics: An Exploration Through Problems and Solutions*. Oxford University Press, 2004.

[21] M. Born, E. Wolf, and A.B. Bhatia. *Principles of Optics: Electromagnetic Theory of Propagation, Interference and Diffraction of Light*. Cambridge University Press, 1999.

[22] Kurt Gibble and Steven Chu. Laser-cooled Cs frequency standard and a measurement of the frequency shift due to ultracold collisions. *Physical Review Letters*, 70(12):1771–1774, 1993.

[23] Ch J. Bordé. Atomic interferometry with internal state labelling. *Physics Letters A*, 140(1-2):10–12, 1989.

[24] E. J. Post. Sagnac effect. *Reviews of Modern Physics*, 39(2):475–493, 1967.

[25] Pippa Storey and Claude Cohen-Tannoudji. The Feynman path integral approach to atomic interferometry. A tutorial. *Journal de Physique II*, 4(11):1999–2027, 1994.

[26] Abhay Ashtekar and Anne Magnon. The sagnac effect in general relativity. *Journal of Mathematical Physics*, 16(2):341–344, 1975.

[27] Marlan O. Scully and Jonathan P. Dowling. Quantum-noise limits to matter-wave interferometry. *Physical Review A*, 48(4):3186–3190, 1993.

[28] Grigorii B. Malykin. The Sagnac effect: correct and incorrect explanations. *Uspekhi Fizicheskih Nauk*, 170(12):1325, 2000.

[29] Louis De Broglie. XXXV. A Tentative Theory of Light Quanta. *Philosophical Magazine Series 6*, 47(278):446–458, 1924.

[30] Resham Sarkar, May E. Kim, Renpeng Fang, and Selim M. Shahriar. N -atom collective-state atomic interferometer with ultrahigh Compton frequency and ultrashort de Broglie wavelength, with N reduction in fringe width. *Physical Review A - Atomic, Molecular, and Optical Physics*, 92(6), 2015.

[31] Masahiro Kitagawa and Masahito Ueda. Squeezed spin states. *Physical Review A*, 47(6):5138–5143, 1993.

[32] J Hald, J L Sørensen, C Schori, and E S Polzik. Spin Squeezed Atoms: A Macroscopic Entangled Ensemble Created by Light. *Physical Review Letters*, 83(7):1319–1322, 1999.

[33] A. Kuzmich, L. Mandel, and N. P. Bigelow. Generation of spin squeezing via continuous quantum nondemolition measurement. *Physical Review Letters*, 85(8):1594–1597, 2000.

[34] Klemens Hammerer, Anders S. Sørensen, and Eugene S. Polzik. Quantum interface between light and atomic ensembles. *Reviews of Modern Physics*, 82(2):1041–1093, 2010.

[35] R. H. Dicke. Coherence in spontaneous radiation processes. *Physical Review*, 93(1):99–110, 1954.

[36] D. B. Hume, C. W. Chou, T. Rosenband, and D. J. Wineland. Preparation of Dicke states in an ion chain. *Physical Review A - Atomic, Molecular, and Optical Physics*, 80(5), 2009.

[37] Sandra Eibenberger, Stefan Gerlich, Markus Arndt, Marcel Mayor, and Jens Tüxen. Matter-wave interference of particles selected from a molecular library with masses exceeding 10,000 amu. *Physical chemistry chemical physics : PCCP*, 15(35):14696–700, 2013.

[38] Igor Pikovski, Magdalena Zych, Fabio Costa, and Časlav Brukner. Universal decoherence due to gravitational time dilation. *Nature Physics*, 11(8):668–672, 2015.

[39] Resham Sarkar, May E. Kim, Renpeng Fang, Yanfei Tu, and Selim M. Shahriar. Effects of non-idealities and quantization of the center of mass motion on symmetric and asymmetric collective states in a collective state atomic interferometer. *Journal of Modern Optics*, 62(15):1253–1263, 2015.

[40] F. Arecchi, Eric Courtens, Robert Gilmore, and Harry Thomas. Atomic Coherent States in Quantum Optics. *Physical Review A*, 6(6):2211–2237, 1972.

[41] Marlan O. Scully, Edward S. Fry, C. H Raymond Ooi, and Krzysztof Wódkiewicz. Directed spontaneous emission from an extended ensemble of N atoms: Timing is everything. *Physical Review Letters*, 96(1), 2006.

[42] May E. Kim, Resham Sarkar, Renpeng Fang, and Selim M. Shahriar. N-atom collective-state atomic clock with $\sqrt{N}$-fold increase in effective frequency and $\sqrt{N}$-fold reduction in fringe width. *Physical Review A*, (6):063629.

[43] R. Bonifacio, L. De Salvo, L. M. Narducci, and E. J. D'Angelo. Exponential gain and self-bunching in a collective atomic recoil laser. *Physical Review A*, 50(2):1716–1724, 1994.

[44] P. R. Hemmer, N. P. Bigelow, D. P. Katz, M. S. Shahriar, L. DeSalvo, and R. Bonifacio. Self-organization, broken symmetry, and lasing in an atomic vapor: The interdependence of gratings and gain. *Phys. Rev. Lett.*, 77:1468–1471, Aug 1996.

[45] Kristian Baumann, Christine Guerlin, Ferdinand Brennecke, and Tilman Esslinger. Dicke quantum phase transition with a superfluid gas in an optical cavity. *Nature*, 464(7293):1301–1306, 2010.

[46] Abraham J. Olson, Robert J. Niffenegger, and Yong P. Chen. Optimizing the efficiency of evaporative cooling in optical dipole traps. *Physical Review A - Atomic, Molecular, and Optical Physics*, 87(5), 2013.

[47] L M Duan, M D Lukin, J I Cirac, and P Zoller. Long-distance quantum communication with atomic ensembles and linear optics. *Nature*, 414(6862):413–418, 2001.

[48] C W Gardiner and P Zoller. *Quantum noise : a handbook of Markovian and non-Markovian quantum stochastic methods with applications to quantum optics*. 2004.

[49] W. M. Itano, J. C. Bergquist, J. J. Bollinger, J. M. Gilligan, D. J. Heinzen, F. L. Moore, M. G. Raizen, and D. J. Wineland. Quantum projection noise: Population fluctuations in two-level systems. *Physical Review A*, 47(5):3554–3570, 1993.

[50] Jian Ma, Xiaoguang Wang, CP Sun, and Franco Nori. Quantum spin squeezing. *Physics Reports*, 509(2):89–165, 2011.

[51] D. J. Wineland, J. J. Bollinger, W. M. Itano, F. L. Moore, and D. J. Heinzen. Spin squeezing and reduced quantum noise in spectroscopy. *Phys. Rev. A*, 46:R6797–R6800, Dec 1992.

[52] D. J. Wineland, J. J. Bollinger, W. M. Itano, and D. J. Heinzen. Squeezed atomic states and projection noise in spectroscopy. *Phys. Rev. A*, 50:67–88, Jul 1994.

[53] A. André and M. D. Lukin. Atom correlations and spin squeezing near the heisenberg limit: Finite-size effect and decoherence. *Phys. Rev. A*, 65:053819, May 2002.

[54] Kristian Helmerson and Li You. Creating massive entanglement of bose-einstein condensed atoms. *Phys. Rev. Lett.*, 87:170402, Oct 2001.

[55] Isabelle Bouchoule and Klaus Mølmer. Spin squeezing of atoms by the dipole interaction in virtually excited rydberg states. *Phys. Rev. A*, 65:041803, Apr 2002.

[56] M. Zhang, Kristian Helmerson, and L. You. Entanglement and spin squeezing of bose-einstein-condensed atoms. *Phys. Rev. A*, 68:043622, Oct 2003.

[57] Monika H. Schleier-Smith, Ian D. Leroux, and Vladan Vuletić. Squeezing the collective spin of a dilute atomic ensemble by cavity feedback. *Phys. Rev. A*, 81:021804, Feb 2010.

[58] Ian D. Leroux, Monika H. Schleier-Smith, and Vladan Vuletić. Implementation of cavity squeezing of a collective atomic spin. *Phys. Rev. Lett.*, 104:073602, Feb 2010.

[59] Yan-Lei Zhang, Chang-Ling Zou, Xu-Bo Zou, Liang Jiang, and Guang-Can Guo. Detuning-enhanced cavity spin squeezing. *Phys. Rev. A*, 91:033625, Mar 2015.

[60] Anders Søndberg Sørensen and Klaus Mølmer. Entangling atoms in bad cavities. *Phys. Rev. A*, 66:022314, Aug 2002.

[61] The signal corresponding to an atomic interferometer can also be derived using de broglie wavelength. however, it can be shown that this approach simply corresponds to interference at the compton frequency in a moving frame, as shown in ref. [**11**,**30**].

[62] A J Leggett. Realism and the physical world. *Reports on Progress in Physics*, 71(2):022001, 2008.

[63] Bernard Yurke, Samuel L. McCall, and John R. Klauder. Su(2) and su(1,1) interferometers. *Phys. Rev. A*, 33:4033–4054, Jun 1986.

[64] F. Toscano, D. A. R. Dalvit, L. Davidovich, and W. H. Zurek. Sub-planck phase-space structures and heisenberg-limited measurements. *Phys. Rev. A*, 73:023803, Feb 2006.

[65] G. Goldstein, P. Cappellaro, J. R. Maze, J. S. Hodges, L. Jiang, A. S. Sørensen, and M. D. Lukin. Environment-assisted precision measurement. *Phys. Rev. Lett.*, 106:140502, Apr 2011.

[66] Emily Davis, Gregory Bentsen, and Monika Schleier-Smith. Approaching the Heisenberg Limit without Single-Particle Detection. *Physical Review Letters*, 116(5):1–5, 2016.

[67] Klaus Mølmer and Anders Sørensen. Multiparticle entanglement of hot trapped ions. *Phys. Rev. Lett.*, 82:1835–1838, Mar 1999.

[68] Dietrich Leibfried, Emanuel Knill, Signe Seidelin, Joe Britton, R Brad Blakestad, John Chiaverini, David B Hume, Wayne M Itano, John D Jost, Christopher Langer, et al. Creation of a six-atom 'schrödinger cat'state. *Nature*, 438(7068):639–642, 2005.

APPENDIX A

Matlab codes for COSAIN Analyses

A.1. Effect of Gaussian Beam Profile and Doppler Effect Induced Detuning

```
clc

close all;

clear all;

format long;


hbar = 1.054571726e-34;

c = 299792458;

lambda = 780.241368e-09;

k_l = 2*pi/lambda;

m = 85*1.66e-27; %%Rb-85

k_B = 1.3806488e-23;


delta = 2*pi*1.5179e9/3;


Gamma = 38.117e6; %%in rad/s
```

```
I_sat = 2*hbar*(pi^2)*c*Gamma/3/lambda^3;

g_0_sat = Gamma/sqrt(2);

I_max = 5e3; %%variable parameter in W/m^2

g_0_max = (sqrt(I_max/I_sat))*g_0_sat;

g_0_adiabatic = 0.1*(2*delta);

om_0 = g_0_max^2/2/delta;


T = pi/2/om_0;



MOT_radius = 0.1e-3;


dr = 1e-6; %%shell width

j = 0;

density_0 = 2.5e3/(4*pi*dr^3/3);


j = j+1;

r = 0:dr:MOT_radius;

density_dist = density_0*exp(-r.^2/2/(MOT_radius/3)^2);


Vol_n = (4*pi/3)*((r+dr).^3-r.^3);


x = dr/2:dr:MOT_radius;
```

```
rho_n = density_0*exp(-x.^2/2/(MOT_radius/3)^2);

XYZ = Vol_n(1:size(x));

atom_shell_n = round(rho_n.*XYZ);

% subplot(2,1,1)
% plot(x,atom_shell_n)
% hold on;
Temp_ar = [];
Signal_Final_ar = [];
waist_size = 500*MOT_radius

Temp = 1e-6;
sigma_v = sqrt(k_B*Temp/m);

% subplot(2,1,2)

%for waist_size = 100*MOT_radius:5*MOT_radius:1000*MOT_radius;



phi_ar = [];
```

```
Signal_Final_ar = [];
for phi = (-1e-2:1e-5:1e-2)*pi
    atom_ar = [];
    Signal_ar = [];
    for i = 1:1:100

        val = 11;
        div = 2*3*sigma_v/val;
        vel_i = -3*sigma_v:div:3*sigma_v;
        f = atom_shell_n(i)*sqrt(m/(2*pi*k_B*Temp))
        *exp(-m*vel_i.^2/(2*k_B*Temp));

        del_i = 2*k_l*vel_i;
        atoms_shell_div = round(div.*f);

        % subplot(2,1,2)
        % plot(del_i,round(div.*f))
        % hold on;

        om_i = om_0*exp(-2*(x(i)-dr/2).^2/waist_size^2);

        OM = sqrt(om_i^2+del_i.^2);
```

```
    A_1 = cos(OM*T/2)-1i*(del_i./OM).*sin(OM*T/2);
    A_2 = -1i*(om_i./OM).*sin(OM*T);
    A_3 = -1i*(om_i./OM).*sin(OM*T/2);
    c_g = ((abs(A_1.*A_2.*A_3)).^2).*4.*(cos(phi/2)).^2;

    dummy = c_g.^atoms_shell_div;
    Signal_shell = prod(dummy);
    Signal_ar = [Signal_ar Signal_shell];
    atom_ar = [atom_ar round(div.*f)];
end


Signal_Final = prod(Signal_ar);
% plot(waist_size/(2*MOT_radius),Signal_Final)
% hold on
%end

% Temp_ar = [Temp_ar Temp];
% Signal_Final_ar = [Signal_Final_ar Signal_Final];
% end
Total_atoms = sum(atom_ar);
%subplot(2,2,j)
% plot(Temp_ar, Signal_Final_ar)
```

```
    % hold all
    Signal_Final_ar = [Signal_Final_ar Signal_Final];
    phi_ar = [phi_ar phi];
end

plot(phi_ar,(cos(phi_ar/2)).^(2*Total_atoms))
hold on

plot(phi_ar,Signal_Final_ar,'r')
hold all
```

APPENDIX B

Matlab Codes for Spin Squeezing Analyses

B.1. SCAIN Signal

This is a sample code for generating signal, variance, and QRF of an SCAIN with $N = 100$ atoms. The squeezing function can be modified to accommodate a TACT squeezing scheme. The values of mu and ν for a given J are derived in a separate program, and so are the spin matrices.

```
J = 50;   % (N atoms)/2

%Spin-J particle matrices functions
J_z = Spin_Sz(J);
J_x = Spin_Sx(J);
J_y = Spin_Sy(J);

%OAT Spin squeezing function
func = 1i*(J_z)^2/2;

%squeezing parameter and corrective rotation angle
mu = [0, pi/2];
nu = [0, pi/2];
```

```
CSS_ini_vec = zeros(2*J+1,1); %define initial CSS vector

CSS_ini_vec(2*J + 1) = 1;

%first pi/2 pulse

CSS_first_pulse_vec = expm(-1i*(pi/2)*J_x)*CSS_ini_vec;


%phase imparted in one dark zone

delta_T = 0:pi/1000:pi/2;


omega = 30e-6;

freq = delta_T/omega/(2*pi);


for q = 1:1:length(mu)


    %Squeezing

    SSS_OAT_pulse_vec = expm(-mu(q)*func)*CSS_first_pulse_vec;


    %Corrective rotation

    rotated_vec = expm(-1i*(nu(q))*J_y)*SSS_OAT_pulse_vec;


    Sig = zeros(length(delta_T),1);

    for k = 1:1:length(delta_T)
```

```
    %first dark zone
    detuning1_vec = expm(-1i*(delta_T(k)/2)*J_z)*rotated_vec;

    %pi pulse
    pi_pulse_vec = expm(-1i*(pi)*J_x)*detuning1_vec;

    %second dark zone
    detuning2_vec = expm(1i*(delta_T(k)/2)*J_z)*pi_pulse_vec;

    %un-rotate
    unrotated_vec = expm(-1i*(nu(q))*J_y)*detuning2_vec;

    %unsqueeze
    unsqueeze_pulse_vec = expm(mu(q)*func)*unrotated_vec;

    %last pi/2 pulse
    last_pulse_vec = expm(-1i*(pi/2)*J_x)*unsqueeze_pulse_vec;

    Sig(k) = (abs(last_pulse_vec(2*J+1))).^2;
end

subplot(2,2,1)
plot(freq, Sig,'linewidth', 2)
```

```
    hold on
    max(Sig)

    Var = Sig.*(1-Sig);
    Var_sqrt = abs(sqrt(Var));
    subplot(2,2,2)
    plot(freq, Var_sqrt,'linewidth', 2)
    hold on;

    partial_Sig = diff(Sig)/(freq(2)-freq(1));
    subplot(2,2,3)
    plot(freq(:,1:length(partial_Sig)),abs(partial_Sig),'linewidth', 2)
    hold on;


    QFF_Inverse = abs(partial_Sig./Var_sqrt(1:length(partial_Sig)));
    subplot(2,2,4)
    plot(freq(:,1:length(partial_Sig)), QFF_Inverse,'linewidth', 2)
    hold on;

end
```

B.2. Pauli matrix definitions

$\mathbf{J_x}$

```
function f = Spin_Sx(J)
Sx_ini = zeros(2*J+1,2*J+1);

for a = 1:1:2*J+1
        for b = 1:1:2*J+1
        if(a==b+1 || a+1==b)
            Sx_ini(a,b) = sqrt((J+1).*(a+b-1)-a*b)/2;
        end
    end
end
f = Sx_ini;
```

$\mathbf{J_y}$

```
function f = Spin_Sy(J)
Sy_ini = zeros(2*J+1,2*J+1);
for a = 1:1:2*J+1
    for b = 1:1:2*J+1
        if(a==b+1 || a+1==b && b>a)
            Sy_ini(a,b) = sqrt((J+1).*(a+b-1)-a*b)/(2*i);
        end
```

```
        if(a==b+1 || a+1==b && b<a)
            Sy_ini(a,b) = -sqrt((J+1).*(a+b-1)-a*b)/(2*i);
        end
    end
end
f = Sy_ini;
```

J_z

```
function f = Spin_Sz(J)
Sz_ini = zeros(2*J+1,2*J+1);
for a = 1:1:2*J+1
    for b = 1:1:2*J+1
        if(a==b)
            Sz_ini(a,b) = (J+1-a);
        end
    end
end
f = Sz_ini;
```

B.3. Husimi Quasiprobability Distribution

```
data_matrix = csvread('J50_Squeezing parameters3.csv', 1, 0);
```

```
mu_derived = data_matrix(:,1);
alpha_derived = pi*data_matrix(:,2);

J = 50;

delta_T = pi/20;  %value of phase
omega = 30e-6;
freq = delta_T/omega/(2*pi);

J_z = Spin_Sz(J);
J_x = Spin_Sx(J);
J_y = Spin_Sy(J);
func = 1i*(J_z)^2/2;

CSS_ini_vec = zeros(2*J+1,1); %define initial CSS vector
CSS_ini_vec(2*J + 1) = 1;
CSS_first_pulse_vec = expm(-1i*(pi/2)*J_x)*CSS_ini_vec;


mu_opt = mu_derived(198);
alpha_opt = alpha_derived(198);

Squeezing_pulse_vec = expm(-mu_opt*func)*CSS_first_pulse_vec;
```

```
rotation_pulse_vec = expm(-1i*(alpha_opt)*J_y)*Squeezing_pulse_vec;
darkzone1_vec = expm(-1i*(delta_T/2)*J_z)*rotation_pulse_vec;
pi_pulse_vec = expm(-1i*(pi)*J_x)*darkzone1_vec;
darkzone2_vec = expm(-1i*(-delta_T/2)*J_z)*pi_pulse_vec;
unrotation_pulse_vec = expm(-1i*(alpha_opt)*J_y)*darkzone2_vec;
Unsqueezing_pulse_vec = expm(mu_opt*func)*unrotation_pulse_vec;
last_pulse_vec = expm(-1i*(pi/2)*J_x)*Unsqueezing_pulse_vec;



[theta_prime,phi_prime] = meshgrid(0:pi/300:pi, 0:2*pi/300:2*pi);
x = sin(theta_prime).*cos(phi_prime);
y = sin(theta_prime).*sin(phi_prime);
z = cos(theta_prime);
tau_prime = tan(theta_prime/2).*exp(-1i*phi_prime);

dummy = 0;
test_vec = last_pulse_vec;  % Vector whose QPD we want to plot
State_ar = zeros(2*J+1,1);
for ctr_ini = -J:1:J

    var_prime = sqrt(nchoosek(2*J,ctr_ini+J))
    .*(tau_prime).^(ctr_ini+J)./(1+(abs(tau_prime)).^2).^J;
    dummy = dummy+(test_vec(ctr_ini+J+1).*var_prime);
```

```
    State_ar(ctr_ini+J+1) = ctr_ini;
end
% figure(2)

s = surf(x,y,z,(abs(dummy)).^2);

shading interp; axis off;
hold on
ax = gca;
colormap(jet)
view(180, 0)
xlabel('X')
ylabel('Y')
zlabel('Z')
```